



HAL
open science

Walking gait features extraction and characterization using wearable devices

Mahdi Abib

► **To cite this version:**

Mahdi Abib. Walking gait features extraction and characterization using wearable devices. Engineering Sciences [physics]. L'ÉCOLE CENTRALE DE NANTES, 2018. English. NNT: . tel-01969674

HAL Id: tel-01969674

<https://hal.science/tel-01969674>

Submitted on 4 Jan 2019

HAL is a multi-disciplinary open access archive for the deposit and dissemination of scientific research documents, whether they are published or not. The documents may come from teaching and research institutions in France or abroad, or from public or private research centers.

L'archive ouverte pluridisciplinaire **HAL**, est destinée au dépôt et à la diffusion de documents scientifiques de niveau recherche, publiés ou non, émanant des établissements d'enseignement et de recherche français ou étrangers, des laboratoires publics ou privés.

THESE DE DOCTORAT DE

L'ÉCOLE CENTRALE DE NANTES
COMUE UNIVERSITE BRETAGNE LOIRE

ECOLE DOCTORALE N° 602
*Mathématiques et Sciences et Technologies
de l'Information et de la Communication*
Spécialité : Automatique, Productique, Robotique
Par

« **Mahdi ABID** »

« **Walking gait features extraction and characterization
using wearable devices** »

Thèse présentée et soutenue à Nantes, le 26 octobre 2018
Unité de recherche : GEOLOC- IFSTTAR

Rapporteurs avant soutenance :

Federica Pascucci, Professeur assistant, Università degli
Studi Roma Tre
Alexandre Janot, Ingénieur de Recherche, ONERA

Composition du Jury :

Olivier Bruneau, Professeur des Universités, Université Paris-
Saclay IUT Cachan
Yannick Aoustin, Professeur des universités, Université
de Nantes, LS2N, UMR CNRS 6004
Éric Le Carpentier, Maître de conférences, Ecole Centrale de
Nantes
Vincent Bonnet, Maître de conférences, Université de Paris-
Est Créteil (UPEC)
Federica Pascucci, Professeur assistant, Università degli
Studi Roma Tre
Alexandre Janot, Ingénieur de Recherche, ONERA
Directeur de thèse
Valérie Renaudin, Professeur des universités, HDR,
GEOLOC/IFSTTAR
Co-directeur ou co-encadrant(s) de thèse
Thomas Robert, Chargé de recherche, LBMC UMR_T9406
(IFSTTAR-UCBL)

I would like to dedicate this thesis to my loving parents ...

Declaration

I hereby declare that except where specific reference is made to the work of others, the contents of this dissertation are original and have not been submitted in whole or in part for consideration for any other degree or qualification in this, or any other university. This dissertation is my own work and contains nothing which is the outcome of work done in collaboration with others, except as specified in the text and Acknowledgements. This dissertation contains fewer than 65,000 words including appendices, bibliography, footnotes, tables and equations and has fewer than 150 figures.

Mahdi Abid
September 2018

Abstract

New wearables devices are introduced with novel options for observing personal transport and mobility in indoor and outdoor spaces. This hardware includes low cost MEMS sensors: accelerometer, gyroscope, magnetometer, which provide continuously available data contrary to existing solutions that are based on radio signals. In order to mitigate the propagation of sensor errors in the position estimate, a pedestrian dead reckoning strategy is commonly adopted. The processing requires parametric step length models relying on some physiological parameters, displacement features and acceleration statistical properties. The coefficients of these models need frequent adjustment to limit cumulative errors induced by alteration of gait pattern. A large experimental database providing information about human locomotion variability is required for this calibration. However, the development of such database is costly in terms of time and effort, and several gait-affecting factors should be considered, which highly increases the number of measurement trials. In this thesis, we propose an alternative way of generating locomotion data that consists in simulating human gait motion under different conditions. In this scope, a 3D multibody system simulator based on parametric optimization technique was developed, and improvements were made throughout this work to get a more realistic walking motion prediction. Joint trajectories during one step were optimized by minimizing an energy criterion based on actuated torques. Validation with inertial data from overground walking experiments on one healthy subject showed an asymmetry in experimental acceleration signals from one step to the next. This suggests that asymmetric movement are likely to result in a step-level asymmetry of displacement features. This defeats the general assumption in PDR strategy: the presence of a device in hand does not impact the gait symmetry and all steps are identical for a fixed walking speed. This hypothesis is investigated with motion capture experiments with several subjects, designed to study the influence of a mass carried in hand on the walking gait cycles. Analysis of variance tests have shown that the presence of a mass in hand changes the gait symmetry at the step level, and then the proposed optimization process is extended to the stride level in order to allow observing asymmetric acceleration patterns. Overall, our simulator reproduces similar fundamental patterns of walking, and the same variation trend of acceleration related items found in experiments. However, it shows limitations when predicting acceleration data

related to the hand, due to some modeling assumptions and numerical issues. Therefore, our simulation approach partially solves for the direct modeling problem in pedestrian navigation, and improvements on model assumptions are foreseen to predict acceleration signals over a complete gait cycle more reliably.

Keywords: Handheld devices, MEMS sensors, Multibody system, Parametric optimization, Step-level symmetry, Walking gait patterns, Human motion analysis, Analysis of variance.

Table of contents

List of figures	xiii
List of tables	xix
1 Introduction	1
1.1 General context: Pedestrian navigation technology	1
1.2 Pedestrian Dead Reckoning	3
1.2.1 Presentation of the PDR strategy	3
1.2.2 Step length estimation	4
1.3 Limitations of current step length models	5
1.4 Thesis contributions	6
1.5 Organization of the thesis	8
2 State of the art	11
2.1 State of the art on human walking gait modeling	11
2.1.1 Simplified gait modeling	11
2.1.1.1 Inverted pendulum model	11
2.1.1.2 Compass gait model	13
2.1.1.3 Ballistic and dynamic walking models	14
2.1.1.4 Limitations of simplified gait models	17
2.1.2 Complex gait modeling	19
2.1.2.1 Robotic versus human motion	20
2.1.2.2 Forward and inverse dynamics	21
2.1.2.3 Skeletal and musculoskeletal models	22
2.1.2.4 Limitations of complex gait models	22
2.2 State of the art on arm swinging during walking and its mathematical modeling	25
3 Experimental extraction of human gait features	31
3.1 Introduction	31

3.2	Estimation of body segment inertial parameters	31
3.3	Overground walking experiments	32
3.3.1	Experimental walking gait features estimation	32
3.3.1.1	State of the art on gait features extraction using inertial sensors	32
3.3.1.2	Selected walking gait features	33
3.3.2	Experimental setup	34
3.3.2.1	Equipment	34
3.3.2.2	Environment	35
3.3.3	Subjects and scenarios	35
3.4	Feature validation process	36
3.4.1	Step characteristics extraction	36
3.4.1.1	Step detection	36
3.4.1.2	Extraction of displacement features	38
3.4.2	Inertial data processing	39
3.4.2.1	Synchronization with simulation data	39
3.4.2.2	Averaged profiles over a stride	39
3.5	Experimental results	40
4	3D modeling of human gait	43
4.1	Introduction	43
4.2	Conception of the 3D biped model equipped with handheld device	43
4.2.1	Biomechanical observations on normal human walking	44
4.2.1.1	Locomotor part	44
4.2.1.2	Head-Trunk-Pelvis	48
4.2.1.3	Arms	50
4.2.2	Presentation of the 3D bipedal model	52
4.2.2.1	Geometric description of the 3D biped	54
4.2.2.2	System parametrization	55
4.3	Gait cycle definition	59
4.3.1	Gait cycle composed of a single support phase and instantaneous impact	59
4.3.2	Switching matrix	61
4.4	Dynamic and impact models	63
4.4.1	Dynamic modeling using Newton-Euler formalism	63
4.4.1.1	Dynamic model in single support	63
4.4.1.2	Zero Moment Point position	64

4.4.2	Impact modeling	66
4.4.2.1	Dynamic model in double support	67
4.4.2.2	Impulsive impact model	68
4.4.2.3	Calculation of the matrices \mathbf{D} and \mathbf{D}_J	69
4.4.2.4	Determination of final velocity parameters	70
4.5	Description of joint motion	71
4.6	Choice of optimization variables	74
4.6.1	Optimization variables for step-level optimization	74
4.6.2	Determination of limit configuration parameters	75
4.7	Definition of constraints and cost functions	78
4.7.1	Constraints	78
4.7.2	Cost function	80
4.8	Validation with experimental data	81
4.8.1	Numerical examples of simulation outputs	81
4.8.2	Estimation of selected gait parameters	84
4.8.2.1	Assessment of natural aspects of walking	84
4.8.2.2	Step characteristics	85
4.8.2.3	Acceleration features estimation	85
4.9	Conclusions and contributions to autonomous geolocation	88
5	Study of walking gait asymmetry induced by a handheld device	91
5.1	Introduction	91
5.2	Human motion capture experiments	92
5.2.1	Experimental setup	92
5.2.2	Subjects and scenarios	93
5.2.3	Parameters used to assess the gait symmetry	94
5.3	Evaluation of walking gait step-level symmetry	94
5.3.1	Experimental results	94
5.3.2	Simulation results from a human gait model in the sagittal plane	98
5.3.3	Impact on the estimation of traveled distance for pedestrian navigation applications	99
5.3.3.1	Position estimation error	99
5.3.3.2	Predicted errors based on empirical data	100
5.3.3.3	Comparison with predicted errors from simulation	101
5.4	Conclusions and contributions to autonomous geolocation	101

6	3D human gait simulator extended to stride level	103
6.1	Introduction	103
6.2	Gait cycle composed of two consecutive steps with instantaneous impacts .	103
6.3	Optimization variables for stride-level optimization	105
6.4	Specific constraints and cost functions	107
6.5	Validation results	108
6.5.1	3D acceleration of the feet	108
6.5.2	COM's vertical acceleration	108
6.5.3	Hand's 3D acceleration	110
6.6	Conclusions and contributions to autonomous geolocation	111
7	General conclusion and perspectives	115
	References	119
	Appendix A	135
	Appendix B Inversion matrix	137
	Appendix C Arm motion	139
	Appendix D COM displacement	141
	Appendix E 2D biped model	143
	Appendix F Acceleration of handheld device	145
	Appendix G Sthenic criterion	147

List of figures

1.1	PDR process using IMU in hand [1].	3
1.2	Different carrying modes of the handheld device [2].	5
1.3	Overview of the proposed approach for a better pedestrian navigation solution.	7
2.1	(a) Inverted pendulum model of the leg movement, where l is the leg length, h is the vertical displacement of the waist, and h is calculated by double integration of vertical acceleration. (b) Modified inverted pendulum to model walking, where S represents the foot length [3].	12
2.2	Compass gait model (Inman et al. [4]).	14
2.3	Schematic representation of a ballistic walking model (Mochon and McMahon [5]).	15
2.4	Passive dynamic walking model including legs with arbitrary mass and inertia, semicircular feet, and a point mass at the hip (McGeer [6]).	16
2.5	Active dynamic walking model (Kuo [7]).	16
2.6	Peak values of (a) vertical ground reaction moment and (b) vertical angular momentum for normal (Light grey), bound (mid grey), Held (dark grey), and anti-normal (black) modes (Collins et al. [8]).	27
2.7	Net metabolic rate for different arm swinging modes (Collins et al. [8]).	28
2.8	Sthenic criteria versus walking speed for different arm configurations: passive, bound, active, and active with springs (Kaddar et al. [9]).	29
3.1	Placement of different devices during walking trials: (a) PERSYs; (b) ULISS 1; (c) ULISS 2.	34
3.2	Tested device carrying modes: (a) Swinging; (b) Texting.	35
3.3	The additional mass taped to ULISS device.	36
3.4	The pedestrian and the associated frames: the navigation frame and the body frame.	37

3.5	Step detection using the acceleration-moving variance detector. Red and purple curves are respectively 3D acceleration norm and 3D acceleration variance signals, the red line indicates the variance threshold level, and blue dots refer to detected step events.	38
3.6	The subdivisions of GC [10].	39
3.7	3D acceleration norm profile of the right (blue) and left (red) foot during a GC for the walking condition $V_2/(S1)$. The dashed lines indicate SS phases.	41
3.8	Vertical acceleration profile of the COM during a GC for the walking condition $V_2/(S1)$. The black dashed lines indicate DS phases.	41
3.9	3D acceleration norm profile of the hand during a GC for the walking condition $V_2/(S1)$. The black dashed lines indicate DS phases.	41
3.10	(a) The peak-trough differences of COM's vertical acceleration and (b) RMS values of hand's 3D acceleration for different walking conditions.	42
4.1	3D knee joint rotations and arcs of motion used in normal walking: sagittal plane flexion (60°); transverse plane rotation (varying from 4° to 8° depending on subject); and coronal plane motion (4° abduction and 2° adduction) [10].	45
4.2	Normal range sagittal plane motion of the knee during a GC. Black line designates the mean values, dotted lines denotes one standard deviation. Gait phase divisions are designated by vertical bars (LR: Loading Response, MSt: Mid Stance, TSt: Terminal Stance, PSw: Pre-Swing, ISw: Initial swing, MSw: Mid Swing, TSw: Terminal Swing) [10].	46
4.3	Vertical displacement of the trunk indicated by head height. It is highest in mid single limb stance (SLS) and mid swing and lowest in DS configurations (loading response and pre-swing) [10].	49
4.4	Lateral displacement of the trunk during walking indicated by head location. It is midline during DS phases (1, 3 and 5), displacement to left during left SS (4), and displacement to right during right SS (2) [10].	49
4.5	Arcs of motion of the pelvis during a stride: 4° for Anterior tilt, 4° for contralateral pelvic drop, and 10° for the transverse rotation [10].	50
4.6	Natural arm swing during free walking. Maximum backward swing (24°) corresponds to IC while peak forward swing (8°) corresponds to terminal stance [10].	51
4.7	Patterns of shoulder and elbow motion during arm swing for a GC. Horizontal scale indicates % GC beginning with IC [10].	52

4.8	The three reference planes in zoological anatomy in the standard human anatomical position: frontal, sagittal and transverse planes [10].	53
4.9	The 3D biped as a tree structure, consisting in $N=26$ bodies and 25 joints. $N_j=19$ joints are variable and the other five joints are fixed. The fixed joints correspond to the virtual bodies added to represent end bodies dimensions as well as the segments relating the trunk to shoulders. The fat bodies represent the main bodies, whereas the thin bodies are fictional bodies (mass, inertias and dimensions are null), they are required to describe the biped through series of one DOF joints.	55
4.10	The Denavit-Hartenberg notation modified by Khalil and Kleinfinger [11]. .	56
4.11	Local frames related to the main bodies of the 3D biped, according to Khalil-Kleinfinger convention [12].	58
4.12	The 19 DOF human linkage model with joint rotations (denoted by cylinders) and dimensions ($l_p, L_p, L_i, i = 1, \dots, 11$).	60
4.13	GC composed of a SS phase and an instantaneous impact.	61
4.14	Forces and moments acting on the support foot of a humanoid robot [13]. .	64
4.15	Forces exerted on the biped during walking: ground reaction forces \mathbf{R}_0 , inertial force ($-m\ddot{\mathbf{x}}_{\text{COM}}$), inertial moment ($-\dot{\mathbf{H}}_{\text{COM}}$) and gravity force mg [14].	65
4.16	The seven variables determining the locomotor system configuration at initial DS: five variables for pelvis situation with respect to the stance foot, and two parameters for step length and width.	75
4.17	Example of interpolation of joint positions for $N = 2$ intermediate time knots. The red/blue dots represent the values from which trajectories are interpolated. The green dots represent the instants where the constraints are evaluated.	82
4.18	Right and shoulder pitch angle histories during three consecutive steps following the sequence right-left-right. The dots correspond to the values at impacts instants.	83
4.19	Right and shoulder pitch joint velocities histories during three consecutive steps following the sequence right-left-right. The dots correspond to the values at impacts instants.	83
4.20	3D acceleration profile of the right (blue) and left (red) foot during a GC: (a) experimental data for the walking condition $V_2/(S1)$, (b) simulation data ($V_2/\text{unloaded swinging}$). The dashed lines indicate SS phases for (a) and impact instants for (b).	86

4.21	Vertical acceleration profile of the COM during a GC: (a) experimental data for the walking condition $V_2/(S1)$, (b) simulation data (V_2 /unloaded swinging). The black dashed lines indicate DS phases, and red dashed lines indicate impact instants.	87
4.22	3D acceleration profile of the hand during a GC: (a) experimental data for the walking condition $V_2/(S1)$, (b) simulation data (V_2 /unloaded swinging). The black dashed lines indicate DS phases, and red dashed lines indicate impact instants.	87
4.23	(a) The peak-trough differences of COM's vertical acceleration and (b) RMS values of hand's 3D acceleration according to different gait velocities. . . .	88
5.1	Experimental setup of motion capture experiments	92
5.2	Handheld device equipped with an optical markers' assembly	93
5.3	Probability density function of the TSI_{step} for the unloaded swinging mode at 5 km/h for one typical test participant	95
5.4	Probability density function of the TSI_{step} for the loaded swinging mode at 5 km/h for one test participant	95
5.5	Probability density function of the TSI_{step} for the texting mode at 5 km/h for one test participant	95
5.6	Averaged TSI_{step} of each participant in the three device carrying modes (considering all the walking velocities). TSI_{step} mostly decreases for the loaded swinging and texting cases with respect to unloaded swinging mode.	97
5.7	Tuckey's HSD test for the three device carrying modes (considering all the walking velocities). Each group mean is represented by a small circle, and each comparison interval is represented by a bar extending out from the mean value. Two group means are significantly different if their intervals are disjoint. They are not significantly different if their intervals overlap.	98
6.1	GC composed of two SS phase and two instantaneous impacts (the red dot stands for the carried mass).	105
6.2	3D acceleration profile of the right (blue) and left (red) foot during a GC for the walking condition $V_2/(S1)$: (a) experimental data, (b) simulation data (continuous/dashed curves correspond to optimization over stride/step). The dashed lines indicate SS phases for (a), and impact instants for (b).	109
6.3	Vertical acceleration profile of the COM during a GC for the walking condition $V_2/(S1)$: (a) experimental data, (b) simulation data. The black dashed lines indicate DS phases, and red dashed lines indicate impact instants.	110

6.4	The peak-trough differences of COM vertical acceleration for different walking conditions: (a) experimental data, (b) simulation data.	110
6.5	3D acceleration profile of the hand during a GC for the walking condition $V_2/(S1)$: (a) experimental data, (b) simulation data. The black dashed lines indicate DS phases, and red dashed lines indicate impact instants.	111
6.6	RMS values of hand's 3D acceleration for different walking conditions: (a) experimental data, (b) simulation data.	112
6.7	Sthenic criterion versus walking velocity for different simulation scenarios.	113

List of tables

2.1	Different formulations for digital human motion prediction [15].	24
3.1	The values of variance threshold and sliding window width for the different gait speeds	38
4.1	Modified Denavit-Hartenberg parameters of the 3D biped.	57
4.2	Step characteristics across three gait velocities for experimental and simulation data. (E): experimental data, (S): simulation data.	85
5.1	Results of the repeated measures analysis (RM ANOVA) applied to TSI_{step}	96
5.2	Effect of carrying mode factor on TSI_{step} for the different gait speeds . . .	96
5.3	Error ratio $\epsilon_{\%}$ in % over the traveled distance for each participant and for the different trials	100
5.4	Error ratio $\epsilon_{\%}$ in % based on simulation results for all testing speeds and for different carrying modes	101
6.1	Optimization variables corresponding to the step labelled j , $j=1,2$ and to N intermediate time knots. (S): Swinging mode, (T): Texting mode.	106

Chapter 1

Introduction

1.1 General context: Pedestrian navigation technology

Nowadays, the location information is considered to be a crucial requirement for pervasive computing where the indoor pedestrian localization is becoming a relevant research field of an enormous potential for many applications with context aware services. In this context, the market for pedestrian positioning applications has recently grown. Thus far, the majority of positioning applications are based on global navigation satellite systems (GNSS). Despite the usage of reliable GNSS-based techniques in outdoor localization, these solutions are primarily limited to open areas where radio signals transmitted by satellites are steadily available [16]. In urban canyons, the continuity and accuracy of GNSS services are not guaranteed since satellite signals are heavily weakened by multipath or even blocked by artificial infrastructures and dynamic obstacles [16], thus leading to loss of information on human movement. Therefore, these services are unreliable inside buildings and indoor spaces, where most location-based services (LBS) users spend 70 - 90% of their time [17, 18]. Hence, a trustworthy indoor navigation solution is strongly demanding [19].

Overcoming this limitation is far more challenging for the use of pedestrian navigation for commercial purposes, as well as for the ability to continuously track people wherever they are to solve safety and public healthcare issues such as risks of falls among older people and monitoring vulnerable patients. Helping subjects affected by a cognitive function deficit or elderly people suffering from dementia or Alzheimer's is a good illustration [20]. Certainly, the main consequences of these diseases are memory loss and lack of attention causing difficult orientation and wandering [20]. Then, permanent tracking and monitoring are required in order to provide efficient assistance in case of necessity or to alert third

parties when pedestrians wander beyond a determined radius considered as a secure area [20].

The integration of GNSS with other technologies is needed to develop an indoor or mixed indoor/outdoor alternative with reference to ubiquity, reliability and, of course, costs. Ultra Wide Band (UWB), Radio-Frequency Identification (RFID), or Radio based positioning systems using Wireless Fidelity (Wi-Fi), are possible solutions for tracking users indoors. However, these systems are usually limited to specific environments because they depend on dedicated infrastructures, which are expensive [21].

An increasing attention to the pedestrian localization issue can also be assigned to the recent development in affordable wearable computing platforms [22]. Smartphones are the example of such systems, since they are efficient enough to perform signal acquisition, preprocessing and run reasonably sensor fusion and real time sophisticated estimation algorithms thanks to Inertial Measurement Units (IMUs) embedded into it [22]. To overcome GNSS limitation, a hybridization technique consisting in fusing natural signals such as accelerations, angular rates, or magnetic sensed by an IMU with GNSS data is a possible approach. One advantage of this solution is that these signals rely on external forces that are always available in all environments (indoors, outdoors). GNSS receivers and IMUs are often embedded in unobtrusive portable devices, which are usually carried in hands or kept in bags.

To estimate body's position and orientation, a strap down method [23] can be applied to inertial data. This method can seldom be employed for long period due to prompt accumulating integration errors ingrained in the low-cost nature of inertial modules, especially drift and biases affecting their signals [16]. Although additional sensors including magnetic compasses are often integrated into the inertial systems to mitigate the heading error, an external reference or source of information is needed. Note that every additional sensor comes at its own costs such as heightened power consumption, system's size and weight, and associated maintenance costs [16]. In order to mitigate the propagation of sensor errors, a better solution would be the usage of pedestrian dead reckoning (PDR) strategy which integrates information from biomechanics of walking movement to estimate the linear pedestrian trajectory [20]. Both methods provide good results when the sensors are attached to some relatively stable parts of human body (e.g. belt or foot). With foot mounted sensors, zero velocity phases of the walking gait can be sensed and used to calibrate the sensor errors [24]. With wrist mounted or handheld sensors, these phases do not exist and the PDR strategy must be adopted.

1.2 Pedestrian Dead Reckoning

1.2.1 Presentation of the PDR strategy

PDR approach consists in estimating the current pedestrian's position denoted \mathbf{p}_k from the position at the previous instant \mathbf{p}_{k-1} and from the estimate of a displacement vector \mathbf{d}_k between those two instants. When the IMU is attached to the foot, the displacement vector is directly estimated by an integration process of inertial measurements [25]. When using the IMU of a smartphone or a connected object, another process is adopted. The displacement vector \mathbf{d}_k is estimated from two parameters which are: walking direction set by an angle, denoted θ_k , and step length, denoted l_k . This process is illustrated in figure 1.1. The recursive equation defining the horizontal position is then:

$$\mathbf{p}_k = \mathbf{p}_{k-1} + l_k \begin{pmatrix} \cos(\theta_k) \\ \sin(\theta_k) \end{pmatrix} \quad (1.1)$$

The instants t_k and t_{k-1} are called step instants. The vertical position, such as a floor change inside a building, is achieved by using a barometer coupled to accelerometers.

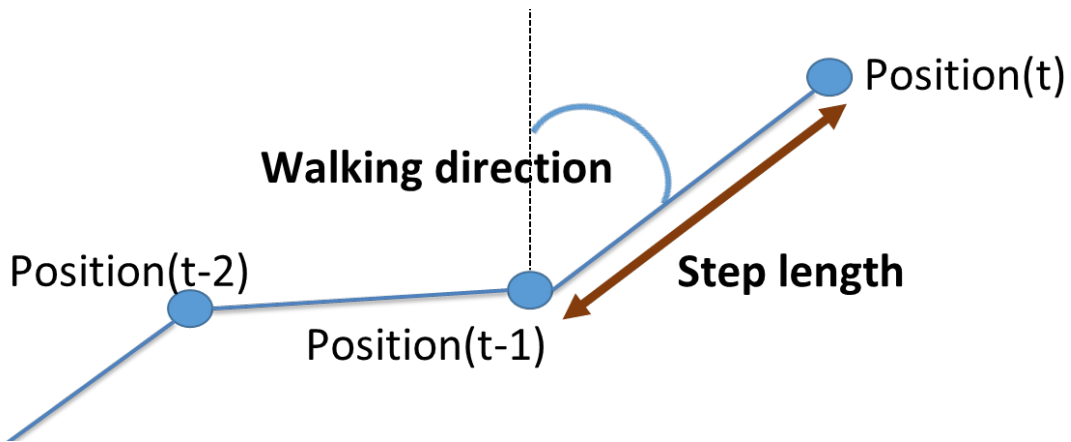


Fig. 1.1 PDR process using IMU in hand [1].

The accuracy of location in pedestrian navigation relies on both step length and walking heading. Thus, promoting the precision of step length estimation is crucial for improving pedestrian navigation service since it has a significant impact on the final position estimate. In other fields of application, such as rehabilitation, gait analysis and sports medicine, step length and the changing rate of step length are essential features for evaluating motion intensity and health condition [3].

1.2.2 Step length estimation

The estimation of step length has been widely addressed in literature [20, 26]. It is performed using several approaches depending on the sensor's location. Most of these approaches focus on inertial data acquired by a sensing device attached to the user's body i.e. close to the center of mass (COM), or linked to the leg [22, 27, 28]. Inertial forces experienced by sensors in these locations directly reflect the gait cycle (GC). Using body fixed sensors, two popular categories of models are used for step length estimation: biomechanical and parametric models. On one hand, biomechanical models consider the user's leg as an inverted pendulum with the sensor located at its COM [22, 28]. A geometric relationship between the vertical displacement of the COM and step length is then used. Other models based on geometric considerations are also proposed in [29, 30]. On the other hand, parametric models use the accelerometer variance and the step frequency to estimate the step length [26, 31]. When studying non body fixed sensors, their emplacement is often constrained to locations where the device is relatively stable during walking. For instance, the device is close to the ear while phoning [24], or is carried in the user's pocket [32]. In these scenarios, inertial signal patterns are similar to those produced by body fixed sensors and analogous approaches can then be applied.

The arm movements have a high degree of freedom that induces a relative independence between the motion of the hand, and the characteristics of pedestrian displacement. The upper limbs constitute important lever arms where movements are amplified in amplitude, speed and variety. Under these conditions, when the device is carried by hand without any constraints, estimating the travel distance is much more complex and specific processing is required. For instance, parasitic motions of the hand that do not reflect the user's displacement have to be identified and classified to avoid wrong propagation of user's position estimate. Very few studies target the case of handheld sensor and phoning or texting scenarios are mostly considered [33]. In these specific scenarios, the sensor mainly experiences inertial forces due to the global motion of the user, similarly to body fixed case.

Overall, when sensors are handheld or wrist mounted, IMU data is first filtered to recognize the activity completed by the different device carrying modes: static, swinging, texting, phoning, handbag/trouser and irregular motion modes [34] (cf. figure 1.2). Step frequencies are then extracted using a Short Time Fourier Transform (STFT) [35] analysis on the accelerations that are filtered in different frequency sub-bands. A binary classifier differentiates between step and stride frequencies since the coupling of the arm oscillations and the steps varies with the walking speed [8, 36]. Finally, parametric models that use physiological pa-



Fig. 1.2 Different carrying modes of the handheld device [2].

rameters (height [20]), step characteristics (frequency [37]) and acceleration signal statistical characteristics [38], either combined or independently, are adopted for step length estimation.

1.3 Limitations of current step length models

Most of parametric step length models assume that common gait has been performed by individuals, who are more likely to exhibit highly irregular gait motions when walking at extreme conditions: under fatigue, when handling an additional mass in hand [2], or due to the specificity of indoor environments e.g. stepping aside to avoid obstacles, walking speed decreased with increasing crowd density, etc. These unpredictable irregular motions can lead into major alteration of gait pattern, which significantly affects the performance of displacement features estimation, since positioning errors at different steps are induced and accumulated over the duration of displacement. Thus, the step length models coefficients should be adjusted frequently. A large experimental database that characterizes the variability related to human locomotion parameters is needed for this calibration. In the ideal case, the collected data should provide information about the substantial variation of walking parameters across different subjects due to intrinsic body morphology and motion pattern, i.e. inter-subject variation, and about their variation induced by a single user under different walking conditions, i.e. intra-subject variation. Hence, a challenging task is to validate the models accuracy on new subjects rather than the ones these models have been adjusted on.

The development of such a database is costly in terms of time, effort and material. In effect, many available volunteers must be found in order to collect enough experimental data, and they have to provide their written consent to perform the trials. The main problems are the number of subjects that is determinant in evaluating the reliability of the empirical method,

as well as subjects' distribution in terms of age, gender, and physiological characteristics (e.g. height, weight) that have to be sufficiently addressed in order to make the collected data as broadened as possible. In addition, experimental protocols should include as many gait-impacting factors as possible (e.g. physiological or sensor-induced), and these factors have to be well measured and labelled in such datasets [39]. Yet, it is hard to analyze the coexisting effects of these factors on gait patterns simultaneously. Besides, several settings of each factor should be considered in order to conduct the evaluation in a generalized and efficient way [39], which highly increases the number of measurement trials included in the dataset, and then more effort and longer acquisition time are needed. To overcome these issues, extended data collected with wide population in the wild [40, 41], i.e. in realistic and uncontrolled circumstances where several environmental and physiological factors affect gait patterns, are used to examine the robustness of gait recognition models. However, the major drawback is that the influence of all particular factors cannot systematically be investigated since its contributions are unlabelled and are somehow merged within such datasets.

1.4 Thesis contributions

The previously proposed step length models have been only partially successful since they are linear, simple and mostly based on empirical observations from biomechanics. Although the biomechanics of normal human walking is well understood [42], little is known about the involved control strategies. Better understanding human locomotion suggests a profound need of exploiting transdisciplinary knowhow derived from human motion analysis and humanoid robotics for better pedestrian linear displacement interpretation. Predictive human gait simulation is a potential approach in this context. The development of mathematical models for full-body kinematics and dynamics for digital human walking modeling taking into account different device carrying modes can help in studying arm swing behavior induced in different walking conditions.

This thesis intends to provide an alternative way to generate the database that could be used for calibration of pedestrian navigation models, by substituting costly experimental protocols for simulated human locomotion. Proposing a human gait simulator, taking into account the correlation between upper limbs and legs movements [8], enables to predict human gait motion under different walking conditions, i.e. walking velocity and device carrying mode, and for given anthropometric properties of the user. This approach allows to generate walking gait acceleration data especially for the hand, while keeping the gait-affecting factors (i.e. sensor-induced, physiological, environmental) well determined and labelled in the generated

datasets since they are treated as input parameters in the simulation process.

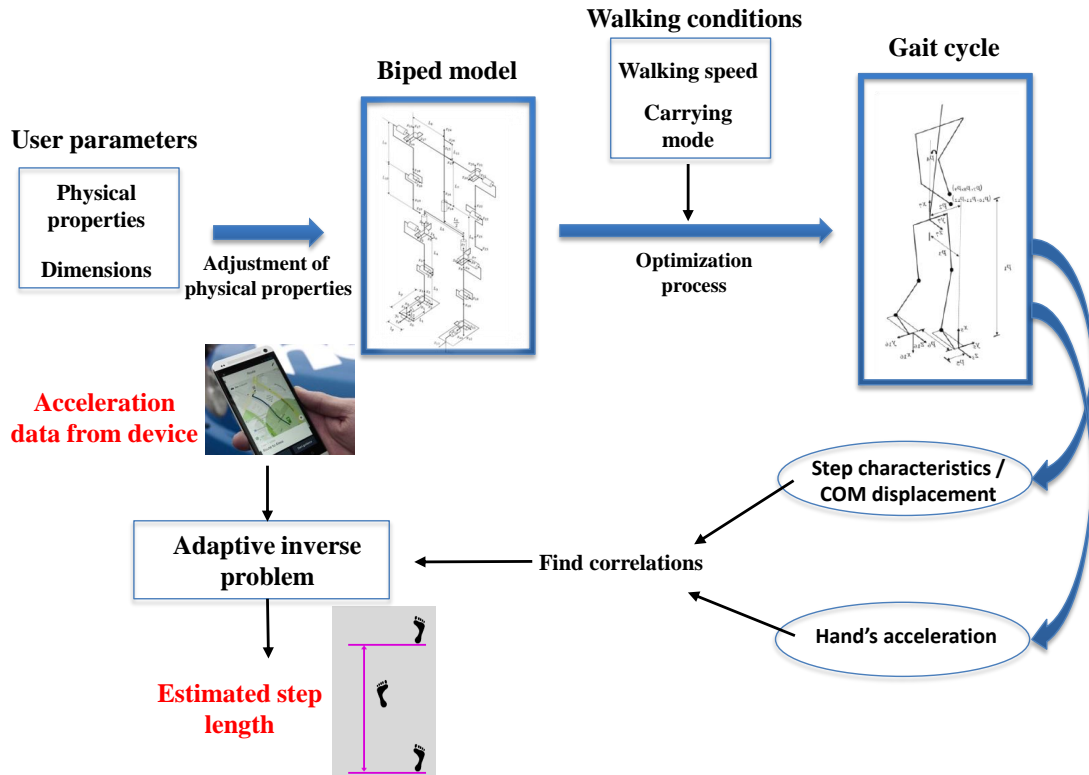


Fig. 1.3 Overview of the proposed approach for a better pedestrian navigation solution.

The proposed approach is illustrated in figure 1.3, and the overall objective of this thesis is to contribute to solving the direct modeling problem, which consists in predicting the linear accelerations of the handheld device for a given carrying mode and given displacement characteristics (i.e. step length, step cadence, etc.). The development of a realistic walking gait simulator for human motion prediction can be employed to build large scale database useful to find fine correlations between accelerometry data sensed at the hand, and the features of the user's displacement. These fine correlations can solve for the inverse problem of pedestrian navigation in an adaptive manner, by building universal step length models dedicated to the hand case.

The overall contribution of this work can be divided into separate identifiable contributions as follows:

- Introducing a 3D rigid skeletal system, whose choices and assumptions are justified by biomechanical observations on normal human gait.

- Combining inverse dynamics and optimization method to predict normal human walking motion over a step, including a single support phase and an instantaneous double support phase, in swinging mode. The walking gait is assumed to be step symmetric, and the walking motion over a stride is deduced from the optimized motion over a step, considering the symmetric property of human body structure.
- Conducting motion capture experiments, with 10 healthy volunteers, to study the step level symmetry of human walking gait under the presence of a handheld device. It is shown that the presence of a smartphone mass (190 g) in hand alters the temporal symmetry over steps, which has a significant impact on position estimation for pedestrian navigation applications.
- Extending the optimization process to the stride level, while considering the possible temporal and spatial asymmetry of walking gait. Swinging and texting modes are tested in the extended model.
- Performing overground walking experiments with a test subject to evaluate the simulation outputs of both step and stride level human walking simulators.
- Discussing the results found with humanoid robotics tools in a context of autonomous geolocation.
- Identifying the limitations of the developed simulation tools, and making recommendations for possible improvements to make the model more realistic for human gait prediction.

1.5 Organization of the thesis

The thesis consists of five main chapters:

- **Chapter 2** is devoted to the introduction of the state of the art in modeling human walking gait. Existing models are divided into simplified and complex gait models, and the limitations of each type of modeling are detailed. Additionally, the state of the art on arm swinging during gait and its mathematical modeling is presented.
- **Chapter 3** is dedicated to the overground walking experiments conducted to evaluate the simulation approach. It first presents the estimation of physical properties of a human test subject using regressions reported in the literature. Then, we present the aim, the experimental setup and the walking gait features that are extracted for

validation. Finally, we present the signal processing of the inertial data and the methods used for step characteristics extraction.

- **Chapter 4** broadly presents the modeling approach. First, a 3D anthropometric model with 19 DOFs is introduced based on biomechanical observations on normal human walking reported from the literature. Then, human walking motion generation using differential inclusion formulation, based on inverse dynamics and parametric optimization, is presented. This method is applied to a walking gait cycle involving a single step, and simulation outcomes are presented and discussed in comparison with experimental data.
- **Chapter 5** is dedicated to the study of the influence of a mass carried in hand on the temporal symmetry of the walking gait cycle. First, we present the motion capture experiments that have been designed for this purpose, as well as the parameters used to assess the symmetry of the walking gait. Then, experimental data are analyzed following biomechanical approaches. The analysis results are then presented and supported by simulation results from a human gait model in the sagittal plane. Finally, the impact of the induced temporal asymmetry on the estimation of traveled distance for pedestrian navigation applications is discussed.
- **Chapter 6** is dedicated to the extension of the 3D human gait simulator to the stride level, motivated by the results of the previous chapter. First, modifications on gait cycle definition, optimization variables, constraint and cost functions are detailed. Then, we present and discuss the validation results of the stride-level simulator based on acceleration data related to different body parts.

Chapter 2

State of the art

2.1 State of the art on human walking gait modeling

2.1.1 Simplified gait modeling

A first approach to understanding the behaviour of the entire musculoskeletal system during normal human walking is to highlight the basic mechanisms involved in this system, using simple biomechanical models. The advantage of such models is that they only have a small number of mechanical parameters to be examined. This would then facilitate the understanding of the relationships between causes and effects. To do this, simple gait models first reduce the musculoskeletal model to its COM, then the modeling of effects produced by the musculoskeletal system with simple mechanical elements is used to simulate the movements of the system during walking. Alexander et al. [43] states that these models can provide an indication on potential strategies that the neuromusculoskeletal system could use to perform walking.

2.1.1.1 Inverted pendulum model

The simplest biomechanical model for studying normal walking is the inverted pendulum. This model consists of a rigid rod representing the subject's leg and a point mass equal to the total body mass of the subject [44]. In this model, the mass describes an arc of a circle above the rigid support leg during the simple support phase, the COM then reaches its highest point at the middle of stance phase. Cavagna et al. [44] then states that the potential energy variations are exactly in phase opposite to external kinetic energy variations calculated at COM. Therefore, at midstance, the potential energy reaches its maximum value and the kinetic energy reaches its minimum value. It is also highlighted that the pattern of mechanical

energy variations at the COM is qualitatively similar to the pattern observed during normal human walking.

The inverted pendulum model is able to predict with reasonable accuracy a large number of experimental observations on normal walking. More particularly, it has been used to (1) simulate the duration of oscillation during normal speed walking [5], (2) explain observed variations in ground reaction force patterns as a function of walking speed [43, 45, 46], (3) study the dependence of COM vertical movements on leg rigidity during walking [47], and (4) study the mechanisms of gait stability control in the absence of active muscle control [48].

Researches in pedestrian navigation estimated step length based on one or two inverted pendulums to model the leg movement [28, 49]. The stride length can be estimated with a gyroscope on the thigh, since the forward displacement of the COM can be calculated (cf. Renaudin [50]). Indeed, in the middle and end of the support phase, the leg is stretched and its movement during this period can therefore be compared to a simple inverse pendulum [51]. The calculation of the covered distance is carried out by integrating the measurement of the angular velocity of the thigh during the mid-stance phase. This integral calculates the rotation angle of the leg, considered as one segment, around the pelvis during a stride. Then, a simple trigonometric relationship is used to estimate the traveled distance.

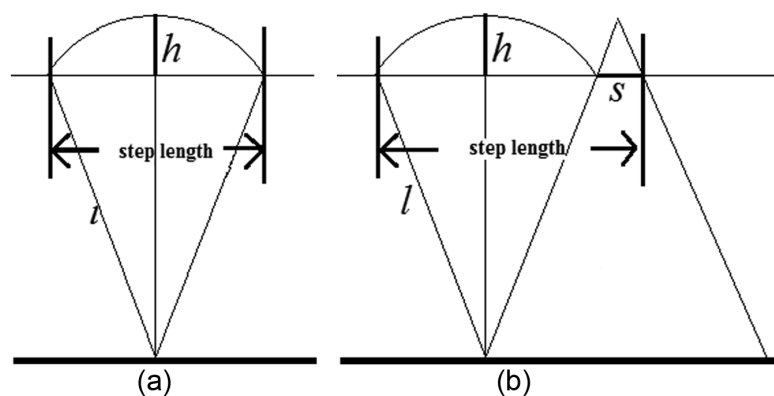


Fig. 2.1 (a) Inverted pendulum model of the leg movement, where l is the leg length, h is the vertical displacement of the waist, and h is calculated by double integration of vertical acceleration. (b) Modified inverted pendulum to model walking, where S represents the foot length [3].

In the case where the acceleration is measured at subject's waist which is close to the body's COM. The problem of step length (SL) estimation is transformed to the problem of how

to calculate the vertical displacement (h) of each step, and the typical solution is to double integrate the vertical acceleration a (cf. figure 2.1(a)):

$$SL = K \times 2\sqrt{2lh - h^2}, \quad h = \iint a(t) dt \quad (2.1)$$

where l is the leg length and K is a constant determined by calibration.

Zhao et al. [3] aimed at estimating step length using sensors based on an improved inverted pendulum algorithm to model the anterior-posterior displacement (L_{ds}) during the double support (DS) phase (cf. figure 2.1(b)):

$$SL = L_{ss} + L_{ds} = 2 \times \sqrt{2lh - h^2} + K \cdot S \quad (2.2)$$

where L_{ss} is the leg displacement during single support (SS), S is the foot length and K is the proportional constant.

In contrast with previous studies, vertical acceleration was integrated as a whole without piecewise integrations. The advantage is to avoid finding the start and the end points of the integrals for each step, which easily results in drift errors.

Among the limitations of using inverted pendulum model for step length estimation is inefficiency when using sensors that are not attached to the body, as it would be difficult to deduce the acceleration of the pedestrian's COM. Another limitation is that vertical acceleration must be integrated to estimate the vertical displacement of the COM, resulting in a double integration of the accelerometer measurement errors. And finally the need for large amounts of training data for calibration of the constant K used in step length calculation formula.

2.1.1.2 Compass gait model

The compass gait model simulates the COM trajectory of a bipedal system in which the lower limbs are represented by rigid links without joints at the feet, ankles and knees. The locomotor system is operated in flexion and extension by joints similar to those of a hip. Each leg has a point mass, and a third point mass is located in the middle of the segment connecting the hip joints. The model assumes oscillation of the lower contralateral limb propelling the body forward, and the COM describes a circular arc around the supporting ipsilateral limb [52] (figure 2.2). Like the inverted pendulum model, the body's COM reaches its peak position at midstance. The COM then describes a vertical downward trajectory under the action of gravity. At the instant of transition between two successive arcs, characterizing the

phase of double support, the oscillating contralateral member slows down the fall and starts a support. Simultaneously, at the end of support, the ipsilateral limb begins its oscillation phase. This results in a second circular arc described by the COM with roles exchanged between the ipsilateral and contralateral members. In the end, the inverted double pendulum model allows to generate a series of complete walking cycles [53].

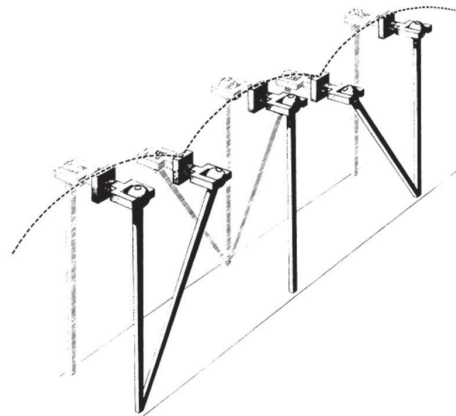


Fig. 2.2 Compass gait model (Inman et al. [4]).

2.1.1.3 Ballistic and dynamic walking models

The ballistic models and the dynamic walking models represent extensions of the inverted pendulum and compass gait models. They differ from these models by the possibility of performing, through simple mathematical models, dynamic walking simulations that can be tested experimentally on machines. Indeed, these models were initially developed to simulate normal human walking by bipedal robots [6, 54], with no interest in muscle and joint control, nor consideration for empirical human behaviour. These models are distinguished by their ability to generate complete periodic gaits either by taking advantage of the action of gravity, through actuating forces on knees and/or hips, or through propulsive forces on support foot.

2.1.1.3.1 Ballistic models Based on a compass gait mechanical model, ballistic models refer to the analysis of the swing phase of gait cycle. Mochon and McMahon [5] showed that the body's forward movement during the swing phase can be accomplished in the absence of any generation of muscle force and only from a set of kinematic conditions i.e. setting the swinging leg velocity at the instant of toe lift. At that moment, their mathematical model establishes this set of initial conditions to both generate ground support and the swing of the contralateral leg (figure 2.3).

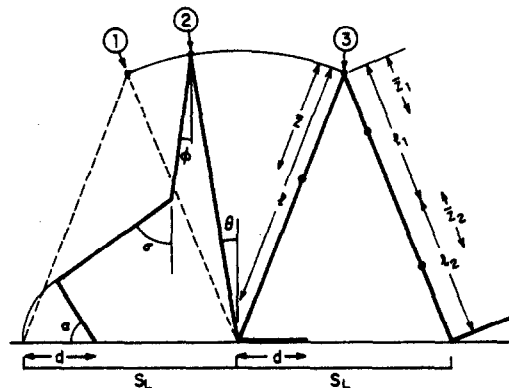


Fig. 2.3 Schematic representation of a ballistic walking model (Mochon and McMahon [5]).

During the swing phase, the system moves only under the influence of gravity and the constraint of a zero mechanical energy variation of the system. The swing phase ends, at initial contact (IC), in kinematic conditions that allow a new step to begin immediately. The explicit hypothesis of such a model is that the swing of the leg can be performed in a similar way to that of a simple pendulum [55], assuming that no muscular torque acts during this phase. Several studies support this hypothesis and point out that the joint moments of the swing limb are small compared to the joint moments of the stance limb [56–58]. Other studies show that electromyographic recordings of the swing limb are also relatively small [59, 60]. The study of normal walking using ballistic models has also made it possible to predict a number of walking parameters such as the duration of the swing phase [61], the kinematics of the swing limb [62] and the constraints required to take off the foot as a function of walking velocity and step length [5].

2.1.1.3.2 Passive dynamic walking models In the case of passive dynamic models, the dynamic parameters of the model give the system the ability to generate a stable and periodic gait on an inclined slope without external energy supply (i.e. actuators) other than the potential gravitational energy (figure 2.4).

In this type of modeling, gait characteristics (walking speed, step duration and length) depend on the geometrical and inertial properties of the system and the slope inclination. This passive system then behaves in a similar way to a simple pendulum since the energy lost due to contact with the leg extremity with the ground is compensated by an energy gain at regular intervals. In fact, for this type of mechanical system, the gain in kinetic energy due to conversion of potential energy during the swing phase is absorbed by the instantaneous impact at IC. From passive dynamic systems, Mc Geer [6] suggests that the geometric and

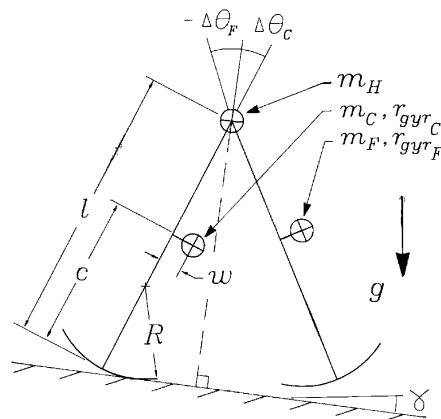


Fig. 2.4 Passive dynamic walking model including legs with arbitrary mass and inertia, semicircular feet, and a point mass at the hip (McGeer [6]).

inertial parameters of the human body (segment lengths, mass distribution) have an effect on walking motion that is equally as important as walking control strategies.

2.1.1.3.3 Active dynamic walking models Active dynamic walking models include rigid support and oscillating legs driven by active torques to allow walking on a flat ground. The first studies based on this type of modeling were limited to planar displacements [7, 63]. Actuation is performed as a pulse directed along the support leg just before toe lift to simulate the muscular activity of the plantar flexors at this instant. The aim is to minimize the energy lost by the system at the impact with the ground of the lower extremity of the leg. The mechanical energy lost would be reduced by 75% by applying this pulse immediately before IC [64]. Another type of actuation can be performed as an actuator torque at the hip in the form of a spring of known stiffness connected to the legs, or by instantaneous joint torques occurring at the beginning and end of the swing phase (figure 2.5).

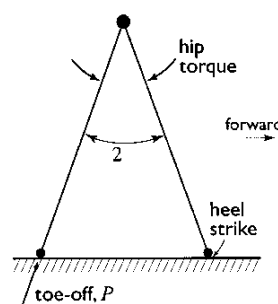


Fig. 2.5 Active dynamic walking model (Kuo [7]).

The advantage of this type of actuation is that the swing frequency of the leg can be adjusted. Other authors [65] have shown that a stable cyclic gait on flat ground can be achieved with simple phasic muscle contractions controlling the hip joint torque. Kuo [7] points out that the metabolic cost associated with the foot pulse and hip joint torque can perfectly predict the relationship between walking speed and step length observed experimentally. By extending these models into three dimensions, Kuo [63, 66] acknowledges that while active dynamic walking models maintain their stability in the sagittal plane, this is not the case in the frontal plane. He nevertheless believes that this instability can be controlled in feedback by the lateral placement of the foot. He infers that humans should exploit more passive leg dynamics in the sagittal plane and probably provide more muscle control to stabilize the lateral movement of the body during walking.

2.1.1.4 Limitations of simplified gait models

2.1.1.4.1 Kinematic approximations In the different simplified gait models, the lower limbs of the human subject are represented by rigid links of zero mass and constant length connecting the COM to the center of pressure (COP) of the support foot. The COP is then considered fixed in the reference frame, and the trajectory of the COM during the support phase is characterized by a circular arc with a constant radius equal to the length of the support leg. The consequence of such modeling is that the vertical trajectory of the COM is overestimated (by 7 to 10%). As Saunders [53] points out, the energy cost generated by a walking modeled by this type of mechanical representation would be overly high.

2.1.1.4.2 Dynamic approximations Several studies [67, 68] reveal that simplified mechanical models of walking cannot accurately predict the vertical reaction force pattern on the ground. They would produce a force pattern that is not correlated with experiments performed on subjects. While experimental data from force platforms for comfortable speed walking show two vertical force peaks and a minimum reached between the peaks, simplified mechanical models predict only one force peak at midstance, when the support leg is perpendicular to the ground. To improve the simulation of vertical force pattern from these models, some authors [46, 67–69] represent the supporting leg more realistically by introducing knee and ankle rotations [67, 69]. Furthermore, Pandy [70] points out that when an individual bends the knee excessively, the peak of vertical ground reaction force would decrease. On the contrary, more rigid lower limbs would increase the vertical force peak [71].

2.1.1.4.3 Musculoskeletal simplification Simplified mechanical models make it possible to analyze global relations between body height and mass, leg stiffness and length,

walking speed, and the global energetic mechanisms of normal walking [42], but they remain unsuitable for understanding the different muscle synergies involved during walking. Although ballistic and dynamic models produce complete stable steps, they do not allow many important details of walking to be studied. For example, active dynamic walking models emphasize the importance of the propulsion phase of the gait cycle, yet the way muscle synergies contribute to propulsion can only be studied using very detailed muscle models [72]. Another important limitation is the inability of these models to represent muscle coordination during double support due to the large number of muscle co-contractions during this phase [73]. Studies introducing muscles into this type of models [65, 74] have predicted step length and walk/run transition speed, and reproduced ground reaction forces over the entire gait cycle. Nevertheless, these studies are subject to important constraints and adjustments e.g. ground reaction pattern, single support duration. A better understanding of the different muscle synergies requires an enhanced model with enough actuators to represent all the muscle groups of lower limbs [42].

2.1.1.4.4 Conservation of mechanical energy The term energy conservation refers to the exchange of mechanical energy between the kinetic energy and the potential energy generated by the pendular movements of the system. Energy conservation would be a phenomenon frequently observed during segmental movements of the human body. This phenomenon would often appear during cyclical movements such as walking. When the COM moves downward, a part of its potential energy is used to accelerate the COM along the vertical axis and is transformed into kinetic energy. When the COM accelerates forward, the kinetic energy of the COM can be used to raise it and provide work against gravity action. However, in reality the theoretical effectiveness of this energy exchange varies with walking velocity [44] and step length [75]. To evaluate the susceptibility of the human body to conserve mechanical energy during gait, the modeling of the individual by simplified mechanical systems, considered conservative, has for many years attracted the interest of researchers. This hypothesis is based on the principle that the bipedal system can be considered as an ideal pendulum whose characteristics are [76]: (i) the mechanical energy of the system, defined as the sum of kinetic and potential energies, is constant during gait cycle, (ii) the displacement of the COM is the consequence of the reciprocal exchanges between the potential energy and the kinetic energy at the COM, (iii) the variations of kinetic and potential energies at the COM are exactly in opposition of phase.

The conservative energy properties would then require no muscle work. However, the validation of this hypothesis should be subject to biomechanical experiments, since the

analogy between the human leg, even rigid, and an ideal pendulum seems to be a very simplified representation. Indeed, it seems unrealistic that the rigid support leg of the system behaves passively. Rather, it would act like a forced pendulum, with internal work exerted to accelerate/decelerate the body.

2.1.1.4.5 Simplification of the double support phase The simplified gait models simulate the trajectory of the COM only during single support phase and represent double support as the instant of transition between two successive single supports at the contact of the swinging leg extremity with the ground (IC). The system legs, both in support, form a closed kinematic chain in double support [77]. The main characteristic of this phase is that it leads to several solutions for actuation. Thus, for a bipedal system, an optimization problem have to be defined in order to choose the best possible combination of torques.

2.1.2 Complex gait modeling

Human walking involves complex synchronization and control between multiple body segments to provide the most energy-efficient and shock-absorbing forward movement possible [53]. Specific gait features derive from variations in dynamic ranges of motion, muscle strength, the relative shape, position and function of musculoskeletal and neuromuscular structures, and capsular and ligamentous constraints on the joints [14]. Although human walking has been the subject of intense research [10, 53, 78, 79], many aspects remain ambiguous. While the motion capture and gait analysis technologies can document and measure details of human walking, they do not have the predictive capabilities needed to fully understand how different anthropometries and states of health or pathologies affect human gait. Toward this end, virtual humans based on mathematical models representing human anthropometry, kinematics, and dynamics were developed. This field, known as digital human modeling, has a broad range of applications in consumer product evaluation, and biomedical engineering.

Predicting natural walking motion for a digital bipedal model with given anthropometric parameters can involve solution of substantial dynamics problems in which joint rotations, torque profiles, and ground reaction forces are all unknowns. Most of physical constraints on human walking, such as joint angle and torque limits, and lack of ground penetration are commonly specified as inequality constraints. These constraints, which can be active at any given instant, tend to give a realistic and natural walking pattern, but they contribute to the difficulty in solving the dynamics problem.

Due to the indeterminacy of the dynamics problem related to human walking, different approaches have been described in the literature to model human locomotion. These approaches can be classified into those that solve the dynamics problem, and those that deal strictly with the kinematics. For instance, statistical database methods deal strictly with kinematics and are based on searching through pre-established motion databases to find appropriate walking motions that are then scaled to correspond with the anthropometry of the considered digital human model [80, 81]. As these methods do not require solving the dynamics equations of motion, they do not provide articular forces or their related work. Therefore, such methods cannot evaluate the stability of walking motions or energy expenditure, or even adapt to walking on inclined slopes. Such methods cannot provide fine details of human locomotion aspects.

There is a huge variation among human motion generation methods that address the dynamics of human walking. To better understand the previous works in this field, one can distinguish between those used for motion planning of robots, and those directed at generating realistic human gait behaviors. Besides, it is helpful to distinguish between methods that solve the dynamic problem directly, and those that solve the dynamics in an inverse way.

2.1.2.1 Robotic versus human motion

In robotics, fast solution of the dynamics is required to facilitate real-time control. For this reason, several equality constraints are imposed on the robotic gait parameters by a priori specification of limb motions to maintain symmetry of gait stages and static stability [82], or by specifying trajectories in time of the zero moment point (ZMP)¹ and the center of gravity (COG) projection to ensure overall dynamic equilibrium [83]. Although such artificial constraints speed up the solution process by reducing the feasible domain, they can be restrictive to the point where the resulting motions are unnatural, unsmooth, and unable to adapt to changes in the anthropometric data or the ground conditions.

Alternatively, for human walking motion, works are based on performance optimization with only natural constraints, which is suitable for generating realistic human gait trajectories. For numerical simulations, the objective functions measures human performance during gait, and optimization techniques are used to find feasible joint motion histories that extremise the objective functions and satisfy the imposed constraints [84, 85]. The major advantage is that the human movements are dynamically feasible and are not artificially constrained. Optimization-based human motion generation problems can be considered as numerical

¹The zero moment point (ZMP) is discussed in section 4.4.1.2.

optimal control problems [15]. Although this method is more computationally intensive and is not adapted to the real-time control and analysis necessary in robotics, it results in more realistic motions and thus is more suitable for studying the biomechanics of human walking.

2.1.2.2 Forward and inverse dynamics

Both forward and inverse dynamics are used in modeling human locomotion. Forward dynamics formulation starts with initial conditions and known forces to find the unknown joint profiles by numerical integration [86–88]. Integrating forces over time intervals to obtain walking trajectories can be a computationally intensive process. Since the forces are themselves unknown and must be obtained by numerical integration of the system differential equations, the approaches utilizing forward dynamics leads to very long simulation times. In order to deal with the computational intensity of forward dynamics, parallel algorithms and processing techniques have been massively used [89]. Additionally, realistic initial values for state variables (e.g. joint positions and rates) and initial guesses for control inputs (e.g. muscle activations) are needed to obtain reasonable gait patterns [90]. This relies on the availability of measurement data [88, 91] and compromises the efficiency of forward dynamics approach as a predictive modeling tool.

In contrast, inverse dynamics is very efficient computationally as it calculates unknown forces from joint displacement histories, and it does not include numerical integration of differential equations. Since the joint motion histories associated with walking are unknown, they are obtained using optimization methods [84, 92, 93]. Initial values for optimization parameters can be set without the need for measurement data and initial values for the state variables are unnecessary [94]. When applying inverse dynamics in gait prediction, simple mathematical functions are used for approximating the generalized coordinates histories [95], where the interpolation function coefficients depend on the optimization variables.

Examples where inverse dynamics formulation have been employed include the planning of a robotic walking and running using optimization by Chevallereau and Aoustin [84] to determine the coefficients of polynomial approximation for histories of the joint rotations and pelvis translations. This study treated walking as a succession of single support phases and assumed instantaneous double support phases (zero duration) defined by passive impact. For predicting human motions, the work of Lo et al. [96], which treated human locomotion and other tasks, provided a meticulous description of an inverse dynamics framework. By adopting the control points of cubic B-spline curves as design variables, Lo et al. used a quasi-Newton algorithm to extract joint angle profiles minimizing active joint torques

during lifting. Saidouni and Bessonnet [85] solved for a symmetric gait motion in the sagittal plane of a 9-DOF model. The gait cycle was composed of repeated single and double support phases that are symmetric when the right and left feet change roles. By defining the interpolation points for the B-spline functions as well as the time durations of gait phases as design variables, the motions for both the single and the double support were simultaneously optimized to minimize the actuating torque energy. Most of these works considered additional trajectory constraints to simplify the optimization process, either by imposing a constant forward velocity of the considered bipedal model [94], or by constraining the motion of some segments to measured data in order to predict the unmeasured segment rotations [95].

2.1.2.3 Skeletal and musculoskeletal models

For human walking modeling, two categories of models are typically used: (i) skeleton models in which all muscles effects are simply modeled by torques applied to joints; and (ii) musculoskeletal models where muscle groups are involved in dynamics equations and represented by Hill-type elements [89, 90, 97]. Skeletal models are commonly employed in robotic modeling, and are even used in the modeling of human walking due to their relative simplicity and computational efficiency [84, 85, 93]. Examples where musculoskeletal models have been used include an 8-DOF (degree of freedom) 3D model by Yamaguchi and Zajac [97] to restore unassisted natural gait to paraplegics and a 3D musculoskeletal body model (with 23 DOFs and 54 muscles) for normal symmetric walking on level ground by Anderson and Pandy [88]. The problem of forward dynamics optimization when using such musculoskeletal models is often posed to minimize metabolic energy expenditure per unit of traveled distance. Terminal posture constraints are typically imposed to ensure repeatability of the gait cycle, and the simulations results match well with the patterns of ground-reaction forces, body-segmental displacements, and muscle activations obtained from experiments.

2.1.2.4 Limitations of complex gait models

2.1.2.4.1 Inertial modeling of human body To associate forces with motion, it is necessary to determine inertial properties of body segments: masses, inertia tensors and COMs positions. Other than expensive medical techniques (gamma ray scanners, magnetic resonance imaging, etc.), there are several methods to estimate Body Segment Inertial Parameters (BSIPs). The choice of one of these parameters can affect the accuracy of joint torque calculations [98]. Some methods represent the human body segments based on geometric volumes, e.g. cylinders, cones, spheres, with uniform density. Measurement or calculation of lengths and circumferences of body segments are used to calculate their volume [99–101]. It is then

possible to obtain the inertial variables of segments knowing their density. Inertial modeling by geometric representation presents some limits since, on the one hand, the density of a body segment vary with the age of the subject. On the other hand, the mechanical hypothesis of non-deformability of body segments implies that their inertial properties are considered unaffected by segments movements [102].

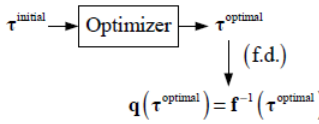
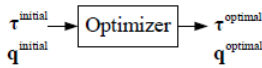
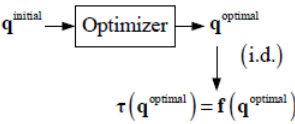
Other methods are based on predictive equations reported in the litterature (Dempster [103]; McConville et al. [104]; Young et al. [105]; Zatsiorsky and Seluyanov [106]) using linear or non-linear regressions. These predictive equations are limited by the measurement techniques and by the population on which they are based [107]. Accordingly, the predictive equations should not be used outside that population. Non-linear regressions should be preferred but scaling equations, based on total body mass and segment length, are more commonly used because of their expediency [108].

2.1.2.4.2 Musculoskeletal system redundancy Simulating human motion and intermediate postures is a difficult task due to the human musculoskeletal system redundancy and other biomechanical factors [81, 109]. The concept of motion prediction using multi-objective optimization techniques provides a feasible approach for predicting intermediate motions of digital human models with a relatively large number of degrees of freedom. Several numerical algorithms for implementing task-based posture prediction using multi-objective optimization techniques have been studied by Yang et al. [110], Mi [111], and Marler [112]. Although viable results have been obtained, the application is limited to kinematics.

Consideration of various effects such as muscle forces, muscle fatigue and anthropometric data is needed for natural motion and realistic digital human modeling. Accordingly, a formulation for motion prediction involving all these parameters is required. Essentially, dynamic equations of motion and constraints have to be satisfied in a defined time interval. The objectives are diverse indexes of human performance, such as energy expenditure, discomfort, or a combination of them. The subsequent optimization problem is then an optimal control problem (OCP) [113]. Optimal control theory has been applied to several human models [52, 89, 114]. Nonetheless, most numerical techniques consider only the control variables (forces/torques) as unknowns, and the state variables are solved by integration of the equations of motion [89]. Recently, direct collocation methods has been used for large-scale neuromuscular control of human motion [115–117].

Nonlinear optimization techniques are used to solve OCP efficiently [118, 119]. The basic method is to discretize the system of differential equations, and then to define parametric representation or finite dimensional approximation for the control and state variables. This idea results in a transformation of the optimal control problem into a nonlinear programming problem (NLP) that is solved numerically. Several viable formulations are available, whose details are listed in Table 2.1. When only the control variables are treated as optimization variables, while the state variables are not included in the system, this is called state variable elimination [120]. If both state and control variables are treated as design variables, the approach is called the direct collocation method [118]. If the control variables are eliminated from the formulation, i.e. only the state variables are considered as optimization variables, the approach is called the differential inclusion method [121]. Wang et al. [15] listed the advantages and disadvantages of these different formulations.

Table 2.1 Different formulations for digital human motion prediction [15].

<p>Design variable: τ</p> <p>Minimize: Single or multiple human performance measures</p> <p>Subject to: $q^L \leq q(\tau) = f^{-1}(\tau) \leq q^U$ (forward dynamics) end - effector</p> <p>Bounds on variables: $\tau^L \leq \tau \leq \tau^U$</p>  <p>State variable elimination</p>	<p>Design variables: q, τ</p> <p>Minimize: Single or multiple human performance measures</p> <p>Subject to: $\tau - f(q, \dot{q}, \ddot{q}) = 0$ (simultaneous) end - effector</p> <p>Bounds on variables: $q^L \leq q \leq q^U$ $\tau^L \leq \tau \leq \tau^U$</p>  <p>Direct collocation</p>	<p>Design variable: q</p> <p>Minimize: Single or multiple human performance measures</p> <p>Subject to: $\tau^L \leq \tau(q) = f(q) \leq \tau^U$ (inverse dynamics) end - effector</p> <p>Bounds on variables: $q^L \leq q \leq q^U$</p>  <p>Differential inclusion</p>
---	--	--

In state variable elimination, the joint angles, velocities and accelerations are obtained through numerical integration of the equations of motion in each optimization cycle. Note that f^{-1} denotes numerical integration in Table 2.1. Design sensitivity analysis is needed in this formulation, since the joint profiles are implicit functions of the optimization variables. Finite difference, adjoint variable method, and direct differentiation method are available to calculate the derivative information for the constraint and objective functions [89, 122, 123]. These methods include numerical integration, which makes the formulation computationally very expensive.

Direct collocation is a computationally efficient alternative to state variable elimination method for solving dynamic optimization problems [115]. In this formulation, the equations of motion are treated as equality constraints since both controls and states are parametrized. The discretized state equations are solved while optimizing the performance criterion, resulting in a non-linear programming problem (NLP) with a large number of optimization variables as compared to state variable elimination methods. Despite the large number of variables, it is not necessary to satisfy the equations of motion at each iteration of the optimization process. They only need to be satisfied at the final solution point. Design sensitivity analysis of the system is not required since the problem functions are all explicit in terms of the variables. With this formulation, these functions are sparse, i.e. each function depends on only a few variables. These sparse properties of the functions must be exploited in the optimization process and, for efficiency, advantage of sparsity of the constraint Jacobians and Hessians is utilized. The resulting optimization problem is solved using powerful sparse NLP algorithms, such as sequential quadratic programming (SQP) [124], and interior point algorithm [125].

When the joint torques are eliminated from the optimization problem so that the unknowns are the joint profiles or their parametric representations, the used formulation is differential inclusion. In this formulation, the governing differential equations are not integrated nor treated as equality constraints. Instead an inverse dynamics procedure is used to determine the joint torques based on the current joint histories. The equations of motion are automatically satisfied in the optimization process. Using differential inclusion, smaller number of optimization variables is obtained in comparison with direct collocation method, and formulations are explicit in terms of variables. The advantage of such a formulation is that constraints on joint profiles can be treated efficiently [15].

2.2 State of the art on arm swinging during walking and its mathematical modeling

Humans tend to swing their arms when they walk while the arm swinging plays no obvious role in human locomotion. It might be costly to use muscles to swing the arms, and it is unclear whether any potential benefits elsewhere in the body justify these metabolic costs. Arm swinging and its effect on human walking gait has been an interesting topic of research over the last decades.

On one hand, many studies argued that the arm swinging is highly passive and analogous to the swing of an unforced pendulum [126]. During gait, human motion can be largely understood as a passive mechanical process. In [48], it is shown that passive-dynamic models might be used to exhibit complex stable motions and to understand some enigmatic aspects of human motion. It might be that human locomotion is largely natural and not heavily controlled. Mathematical models indicate that arm swinging may arise simply from translations of the shoulders [127], although muscle inputs may be necessary for sustained rhythmic swinging [128].

On the other hand, using experimental data, the authors of [129] make arguments that muscle activity is needed to produce human-like walking and that the swing phase in gait cycle cannot be passive. In fact, swing phase kinematics can't only be generated by gravitation because the gravitational forces contribution to the total kinetics is very small. Besides, the kinetics due to gravity do not have the same pattern as a normal swing phase. Other measurements indicated significant shoulder torques [130], although with reported peaks varying as much as three-fold, e.g. 3.8 N·m reported by Jackson et al. [131] and 12 N·m by Hinrichs [132]. Muscular effort is also suggested by observations of significant electromyographic activity, which led to the recommendation that muscular forces dominate upper limbs swinging [133]. How walking may induce arm motion has been mostly studied, but not how arm motion affects walking, thus giving indication of possible benefits.

There are many possible benefits to arm swinging. Suggested effects include reduced vertical displacement of the COM [132, 134], and reduction of angular momentum [130, 132, 135], angular displacement [126, 133] or ground reaction moment [136, 137], all about the vertical axis. Other possible effects include prevention of uncontrolled arm motions [128] and increased walking stability [138]. Also, arm swinging appears to have some physiological benefit, as evidenced by reports of increases in the energetic cost of walking when the arms are prevented from swinging [8, 134, 138].

Collins et al. [8] conducted an interesting experimental study to analyze the effect of human arm swinging on the metabolic energy consumption and gait mechanics while human subjects walk in different walking modes. The studied walking modes are normal, bound, held and anti-normal. First, it was found that vertical ground reaction moment about the COP of each foot and vertical angular momentum about the COM increase in the order normal, bound/held (with no significant difference between the two) and anti-normal (see figure 2.6). On the contrary, it was found that vertical center of mass displacement remains relatively

unaffected, and is nearly the same for normal and anti-normal conditions, the latter therefore serving to isolate this effect from the others. Because the vertical ground reaction moment is transmitted upward from the support foot through the leg and the body, it was hypothesized that muscular effort may be required to resist that moment. Consequently, it was concluded that the metabolic cost increases in the same order of normal, bound/held and anti-normal (see figure 2.7). Finally, the held condition was applied because simulations suggested that it may actually require effort to prevent the arms from swinging naturally, implying that the held mode might require greater energy expenditure than bound condition. In contrast, this work does not experimentally study the effects of walking velocity, which has a strong effect on human arm swinging during walking.

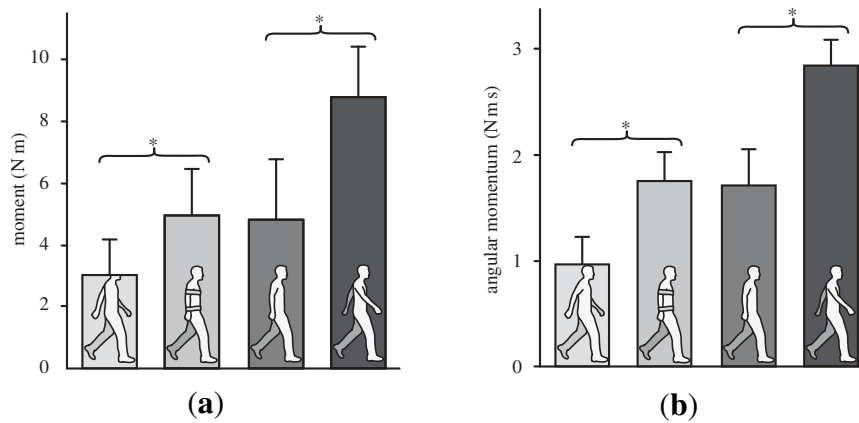


Fig. 2.6 Peak values of (a) vertical ground reaction moment and (b) vertical angular momentum for normal (Light grey), bound (mid grey), Held (dark grey), and anti-normal (black) modes (Collins et al. [8]).

Kaddar et al. [9] studied the arm swinging effects on the walking bipedal gaits composed of impact, single and double support phases. A mathematical approach to study the effect of arm swinging on the bipedal gait was used. The biped used in this study is inspired from HYDROID which is a hydraulic robot built by ANR. The mass inertial properties of this robot approximately correspond to that of an adolescent boy. The two aims of this study are: (i) to verify the effect of arms on a sthenic criterion during walking and (ii) to determine whether the optimal movement of the arms is passive or not. Different evolutions of arms are treated: bound arms, arms having an active motion, and passive arms, where each arm consists of one-link. The comparison of results for different walking velocities show the importance of an active movement of the arms. A passive movement of the arms has large amplitude when the natural frequency of the arms coincides with the frequency of the walking gait. Adding springs at the shoulders allows adjusting the natural frequency of the arms to that of

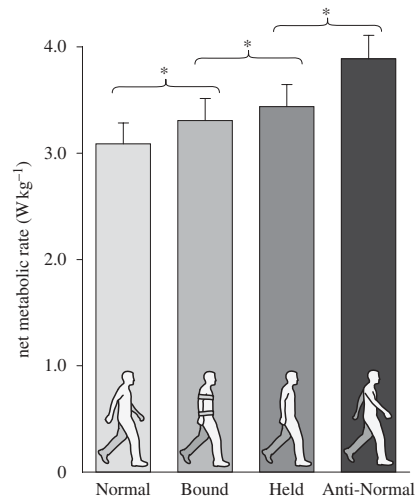


Fig. 2.7 Net metabolic rate for different arm swinging modes (Collins et al. [8]).

walking gait. However, the sthenic criterion with the active arms with or without spring is found to be less than the case with the passive arms for all walking speeds (cf. figure 2.8). In addition, a recent study (Aoustin and Formalskii [139]) based on a ballistic walking gait designed for a 3D biped with two identical two-link legs, a torso, and two identical one-link arms, focused on the optimal swing of the arms. In this study, the biped is controlled with impulsive torques at the instantaneous double support to obtain a cyclic gait. Simulation results showed that for a given time period and a given length of the walking gait step, there is an optimal swinging amplitude of the upper limbs. For this optimal arms motion, the effort cost functional of impulsive control is minimum.

Most of the previous work considers only one link to model the human arm, which is a simplification. However, it does provide us some interesting indications on the arm swinging effects on human walking. Considering a two-link arm would be a closer approximation to the real human arm, and adding a point mass object (handheld device) at the end effector (forearm extremity) could be interesting to model a device attached to human hands for a pedestrian navigation solution.

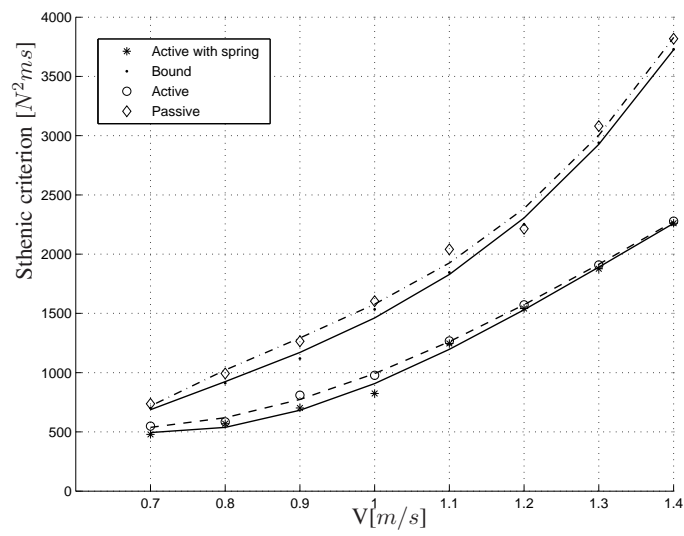


Fig. 2.8 Sthenic criteria versus walking speed for different arm configurations: passive, bound, active, and active with springs (Kaddar et al. [9]).

Chapter 3

Experimental extraction of human gait features

3.1 Introduction

In this chapter, we present overground walking experiments designed to evaluate our simulation approach in modeling cyclic human gait. Walking gait features related to different body parts were extracted from experimental data of one test subject, and were used as comparison criteria to assess simulation outputs based on a biped model fitted to the subject.

3.2 Estimation of body segment inertial parameters

In this thesis, we consider a 3D skeletal model of human structure. To make the biped model fit a given test subject, anatomical definition found in [108] is considered to estimate the segments lengths. In addition, the regressions of Dumas [108], based on the extensive data of McConville [104] and Young [105] (Mass distribution and anthropometric characteristics of adult men and women) are used to estimate the BSIPs (See appendix A). These parameters correspond for each body segment to its mass, its COM position in the body referential and its inertias.

3.3 Overground walking experiments

3.3.1 Experimental walking gait features estimation

3.3.1.1 State of the art on gait features extraction using inertial sensors

The usage of inertial sensors in gait analysis is a promising method for feature extraction, as they are designed to be light, cheap and portable, and to escape from the need for specific experimental environment [140]. They are non-invasive, do not alter the motion patterns [141] and can identify human activity in different environments [142, 143]. The use of 3D sensors provides more information of human motion in three planes [144]. Inertial sensors are mainly used for human motion monitoring, as well as activity recognition and advanced gait analysis [39]. Potential applications of these approaches are healthcare and disease prevention (i.e. fall detection for elderly people [145], assessment of physical activity patterns to detect gait abnormalities [140]) and sports (i.e. gait speed estimation and step count [146]). Recently, gait recognition based on inertial sensors for localization purposes has become indispensable with the appearance of smart devices and wearable systems including these sensors [39]. Gait patterns can be explicitly identified as physiological properties, i.e. 3D joint angle estimation [147], detection of gait cycle phases [142], or estimation of spatio-temporal characteristics (step length, width of walking base, gait symmetry, cadence, etc.) [148]. These patterns can be also expressed using feature extraction techniques that do not exactly provide physiological parameters but implicitly contain information on walking motion [39]. Note that most of the above mentioned applications are only possible with inertial data acquired by fixed sensing device on a single pre-determined position on the human skeleton.

Several types of inertial sensors have been employed for gait analysis either combined, or with other non-inertial sensors [140]. The most used sensor is accelerometer either biaxial or tri-axial. The object frame for accelerometer measurements is the accelerometer case, while the reference frame is inertial space, and measurements of specific force are resolved along the sensitive axes [149]. In general, accelerometers are combined with gyroscopes, that measure angular rate without an external reference [149], to decrease the error induced by accelerometer vibration and to constitute an Inertial Measurement Unit (IMU) system [148] or a self-developed multi-sensors system [142]. IMUs allow computing the position in local frame by integrating acceleration in the case of strap-down mechanization or by step detection within the PDR strategy [149]. The trajectory's directions are given by the integration of angular rates measured by the gyroscope. Magnetometers are also included in

IMU systems [141]. When using more inertial sensors, the accuracy of features estimation is improved thanks to data redundancy and data fusion algorithms [150]. Nevertheless, a compromise between precision and portability should be considered.

Researchers place these sensors in different parts of the body, e.g. attached to lower limbs (foot, thigh) to accurately detect gait phases and displacement features, to upper body (waist, abdomen) or to the arms [140]. The highest locations are ears and head [151]. The acceleration of the upper parts can better assess the body stability and balance during gait [152], and contribute to a more sophisticated gait analysis [140].

3.3.1.2 Selected walking gait features

For overground walking experiments, there are two sets of gait features that are extracted from experimental dataset:

- The displacement features:
 - The gait velocity V ;
 - The stride characteristics i.e. length (d) defined as the distance between two consecutive prints of the same foot, width (w) defined as the lateral distance between the midlines of both feet, and duration (T);
 - The step-level symmetry indexes i.e Temporal Symmetry Index [2] and Spatial Symmetry Index respectively notated TSI and SSI, and defined as:

$$\text{TSI} = \frac{\text{Time duration of step on the device's side}}{\text{Total time duration of the stride}} \quad (3.1)$$

$$\text{SSI} = \frac{\text{Length of step on the device's side}}{\text{Stride length}} \quad (3.2)$$

Note that stride is defined between two successive initial contacts by same foot, and a right step is the interval between left IC and following right IC.

- The acceleration features over GC related to different body parts:
 - Both feet;
 - The waist whose motion reflects the center of mass (COM) kinematics.
 - The hand that is carrying the inertial unit.

3.3.2 Experimental setup

3.3.2.1 Equipment

Two ULISS devices [153] and two PERSY systems [154] designed by IFSTTAR-GEOLOC Laboratory are used for data collection. Each ULISS device contains a nine-DOF inertial and magnetic unit, a high sensitivity GNSS receiver, a battery, and a memory card. It weights 0.129 kg which is approximately the mass of a smartphone. Raw inertial data are collected at 200 Hz frequency. During trials, one ULISS device is held in hand by the subject while the other one is attached to the rear of the belt (cf. Fig. 3.1(b,c)).

PERSY systems has been designed for reference positioning in indoor environments. For this task, they must be attached to both feet (cf. Fig. 3.1(a)). Novel data fusion algorithms are used to obtain trajectories with drift errors less than 0.5%, based on results found in [154]. These reference systems are lightweight, wireless, and comprise an internal logging system and a battery. To obtain the best possible position using MEMS technology, three inertial and GNSS sensors running at 160 Hz are embedded in each PERSY: a high precision IMU STIM300 with a gyro ranging up to 800°/s, a magnetometer HMC5983, and an M8T GNSS receiver. All devices have GNSS running at 5 Hz and autonomy of four hours. All data are timestamped using GPS time.

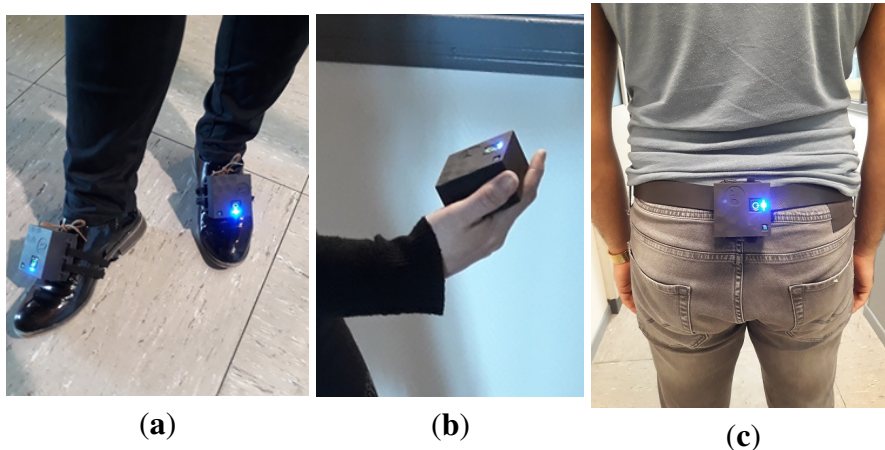


Fig. 3.1 Placement of different devices during walking trials: (a) PERSYs; (b) ULISS 1; (c) ULISS 2.

3.3.2.2 Environment

Experiments took place at the site of IFSTTAR institute in Bouguenais, France. Walking tests were performed indoor in a 55m-long hall, in one of the site's buildings. Before each acquisition, magnetometers calibration in outdoor is needed, as well as a static phase of about one minute to get GPS time for data synchronization. Data collection lasts about 30 minutes for each subject.

3.3.3 Subjects and scenarios

Nine healthy volunteers participated in data collection with the following gender distribution: five men and four women. The age ranges from 23 to 57 with an average of 32 years. The subjects' heights are between 1.6 m and 1.87 m, and weights range from 53 kg to 94 kg.

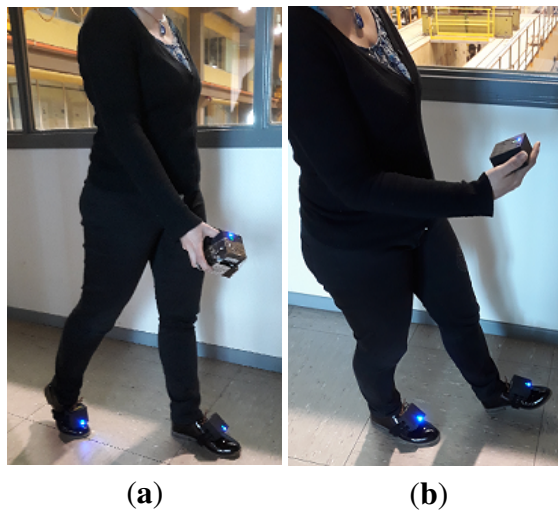


Fig. 3.2 Tested device carrying modes: (a) Swinging; (b) Texting.

The following device carrying modes were tested for straight walking scenarios (cf. figure 3.2):

- *Swinging mode (S1)*: the subject is walking with freely swinging arms, and handling ULISS 1 in the right hand;
- *Texting mode (T)*: the subject is asked to walk while watching the device in hand so that right arm configuration is comfortable for texting or reading;
- *Swinging mode (S2)*: the same as (S1), however an additional mass is taped to ULISS 1 (cf. figure 3.3) and the total handled mass is 0.627 kg. The purpose of this scenario is to test the sensitivity of optimal arm movement to an increased handheld mass.



Fig. 3.3 The additional mass taped to ULISS device.

Each walking scenario was performed at three walking speeds: comfortable (V_2), slow (V_1) and fast (V_3) speeds. These different speeds were self-selected by participants relative to their comfortable pace. To avoid any order effects, subjects were free to select speeds order and the order of carrying modes within the same gait speed. For each speed/carrying mode combination, subjects walked twice along the hall, back and forth between the start and the end of the walkway. The trials were separated by static phases of 10 s. Subjects were instructed to maintain the same speed and a straightforward direction during each trial.

Note that for this thesis, experimental data for one test subject (26-year old, 1.84 m height and weighing 85 kg) were considered for validation of the proposed simulation approach. The whole dataset for all subjects will be used for further work to examine the inter-subject variation of the generated walking parameters.

3.4 Feature validation process

For each walking condition, selected gait features were calculated for 25 consecutive strides centered in trials time interval i.e. out of acceleration/deceleration phases. Since there are two walks by condition, i.e. back and forth, gait features are averaged over 50 strides.

3.4.1 Step characteristics extraction

3.4.1.1 Step detection

Gait cycle is characterized by the occurrence of a stable foot's point during the flat foot phase, which corresponds to step events. The Zero Velocity Detection (ZVD) method has widely been adopted in the navigation field to detect steps. It is applied to extract the step events

from the acceleration data based on an acceleration moving variance detector and it searches for the periods when the foot is stationary [24]. The detected step events correspond, for each foot, to the end of flat foot phase. ZVD was applied to PERSYs specific force in the navigation frame NED (North-East-Down; cf. figure 3.4). Specific force is projected in NED using MAGYQ algorithm [155] that estimates attitude angles of the IMU in the navigation frame.

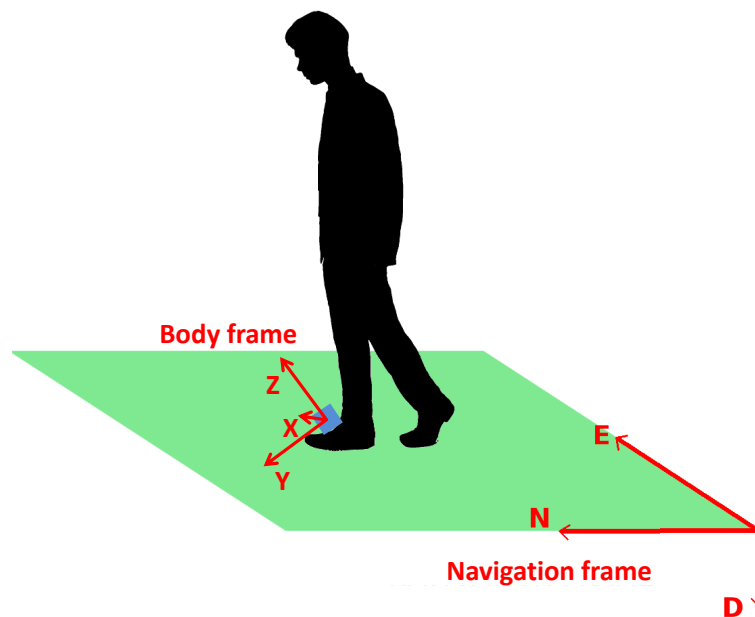


Fig. 3.4 The pedestrian and the associated frames: the navigation frame and the body frame.

The variance of the norm of the acceleration vector is calculated over a sliding window and compared to an adaptive threshold. The variance threshold and the width of the sliding window are adapted by manual tuning so that there is no under/over detection of steps. For higher gait velocities, the variance threshold increases and the sliding window is less wide since stationary phase gets shorter. Note that the same values of width and threshold are used for a given subject/gait speed combination, regardless the carrying mode (see Table 3.1). This step detection method is illustrated in figure 3.5, where the blue dots correspond to the detected stance phases, i.e. the steps. The detection is performed for both the right and left feet in order to estimate the temporal displacement features.

Table 3.1 The values of variance threshold and sliding window width for the different gait speeds

ZVD parameter	Walking speed		
	V_1	V_2	V_3
Variance threshold (m^2s^{-4})	0.32	0.9	1.45
Width of sliding window (ms)	175	125	106

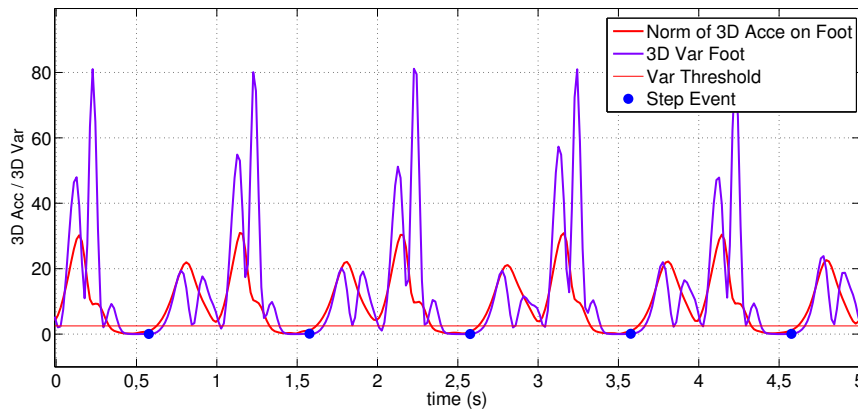


Fig. 3.5 Step detection using the acceleration-moving variance detector. Red and purple curves are respectively 3D acceleration norm and 3D acceleration variance signals, the red line indicates the variance threshold level, and blue dots refer to detected step events.

3.4.1.2 Extraction of displacement features

Once steps are detected, average temporal characteristics were determined for each walking condition. Step instants were used to calculate stride durations. Since there was no difference in mean values between left and right steps, stride duration was calculated in terms of the mean values for both feet. Relative durations between right and left steps detections were used to calculate TSI indexes.

A developed software was used to calculate reference trajectories of both feet with respect to a base station located in the test site, based on data collected with each PERSY. These trajectories allow to obtain footprints coordinates corresponding to step instants. Stride length was calculated from distances between each two consecutive footprints, averaged on both feet. Then, gait velocity was determined from mean stride length and duration. Using relative positions of right footprints with respect to left footprints, as well as walking direction proper to each stride, step width values and SSI indexes were calculated.

3.4.2 Inertial data processing

3.4.2.1 Synchronization with simulation data

In order to compare inertial variables profiles from both simulation and experimental data, we resampled stride time profiles over 100 points from 1 to 100, where 1 denotes the beginning of the gait cycle while 100 marks its end. Since the step detection method detects the end of each flat foot phase as shown in figure 3.5, one gait cycle lasts from the beginning of left rotation subphase about the toe until the end of next flat foot phase of the same foot (see figure 3.6). Note that while double support phases last nearly 20% of the gait cycle [10], they were considered as instantaneous in the simulation.

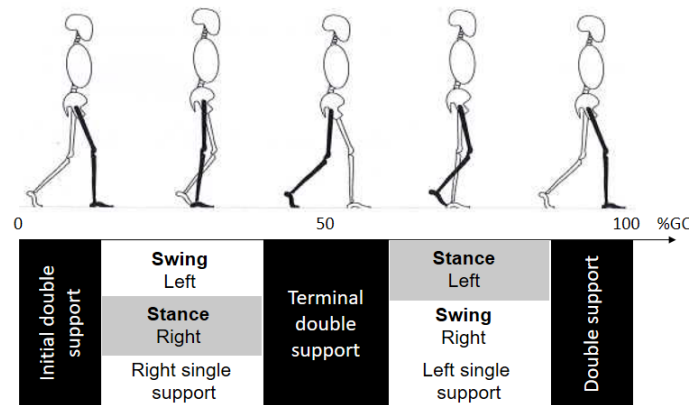


Fig. 3.6 The subdivisions of GC [10].

3.4.2.2 Averaged profiles over a stride

Due to the cyclostationary nature of steady gait, a segmentation of kinematic and inertial data is conducted in order to calculate averaged patterns that can be compared with profiles generated by simulation. Acceleration signals collected from different devices can be synchronized and divided into gait cycles. Gait cycles time intervals are then defined between successive step events of the left foot.

Perturbations caused by small variations in gait velocity can result in temporal variations in walking patterns. First, the lengths of extracted gait cycles are normalized to the mean length, while preserving the same shape of each signal pattern. Spline interpolation is used for this normalization. Second, an optimal matching of stride-specific profiles is needed since alignment impacts the temporal shape of the averaged pattern. Progressive cycle alignment is performed by dynamic time warping (DTW) approach [156] so that amplitude attenuation

and phase shift are avoided for aligned signals. Then, averaged signal patterns are obtained by averaging the corresponding aligned profiles.

3.5 Experimental results

Averaged acceleration profiles related to different body parts are presented in figures 3.7, 3.8 and 3.9, for the walking scenario $V_2/(S1)$. These profiles, in addition to acceleration items depicted in figure 3.10, will be used as evaluation criteria for the simulation outputs.

Figure 3.7 shows 3D acceleration profiles of both feet during gait cycle. Two main peaks of acceleration are observed in single support: the first occurs at initial swing (about 30% of single support) serving as a base for swinging leg advancement, and the second occurs at the landing foot's initial contact with the ground which marks the end of single support phase. Peak values of acceleration profiles for both feet significantly increase with the gait velocity, and within the same velocity, there is no significant impact of carrying mode on these values.

The shape of COM's vertical acceleration profile (cf. figure 3.8) shows two peaks occurring in each double support phase and corresponding to front foot heel rotation and rear foot rotation about the toe. The negative peak amplitude is close to the positive one. Figure 3.10(a) shows the differences between peak and trough values (i.e. differences between maximum and minimum values throughout the gait cycle) of COM vertical acceleration for different walking conditions. Within the same device carrying mode, the peak-trough difference significantly increases with walking speed. For a given walking velocity, differences in vertical acceleration items are mainly due to differences between step length values.

For swinging mode scenarios, experimental data show that peaks of 3D acceleration of the hand occur in double support phases (cf. figure 3.9). The highest acceleration peak (5% GC) correspond to the maximum backward swing of the loaded arm, while the second peak (50% GC) coincides with peak forward swing. Minimum acceleration values occur in single support phases during arm swing motion. Root mean square (RMS) values of hand's 3D acceleration for different walking scenarios are shown in figure 3.10(b). A decrease of the RMS value is observed for the mode (S2) compared to (S1) because of the additional mass carried by the hand. In addition, there is a significant decrease of RMS levels for the mode (T) with respect to swinging modes as a result of the constrained arm configuration. Results also show that, within the same carrying mode, RMS value increases as a function of the gait velocity.

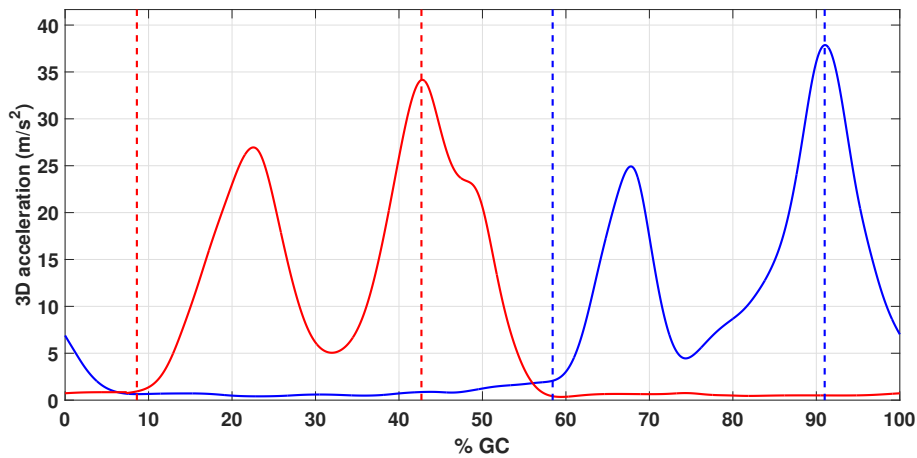


Fig. 3.7 3D acceleration norm profile of the right (blue) and left (red) foot during a GC for the walking condition $V_2/(S1)$. The dashed lines indicate SS phases.

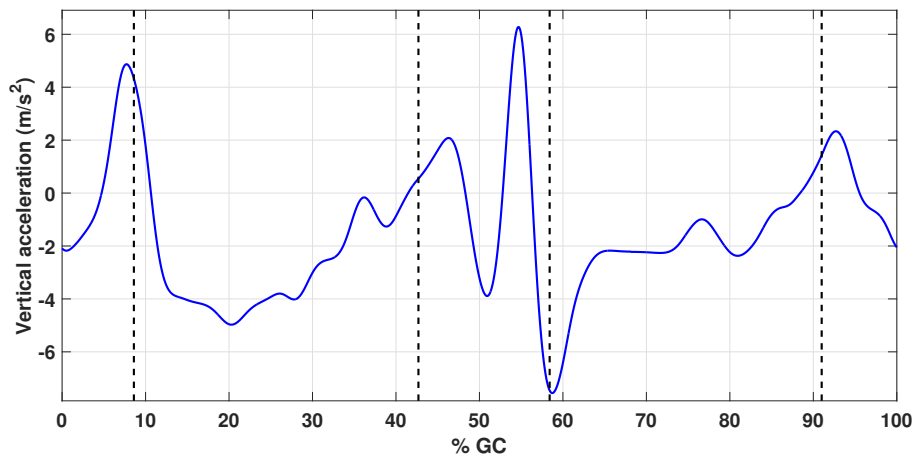


Fig. 3.8 Vertical acceleration profile of the COM during a GC for the walking condition $V_2/(S1)$. The black dashed lines indicate DS phases.

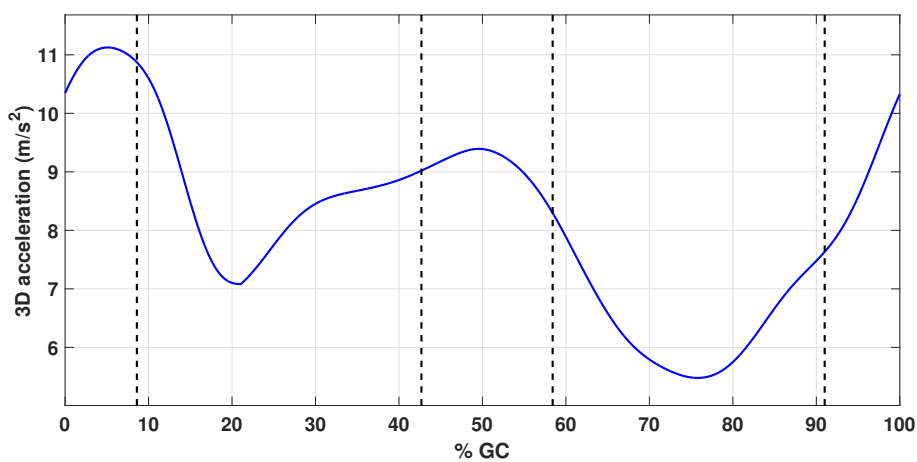


Fig. 3.9 3D acceleration norm profile of the hand during a GC for the walking condition $V_2/(S1)$. The black dashed lines indicate DS phases.

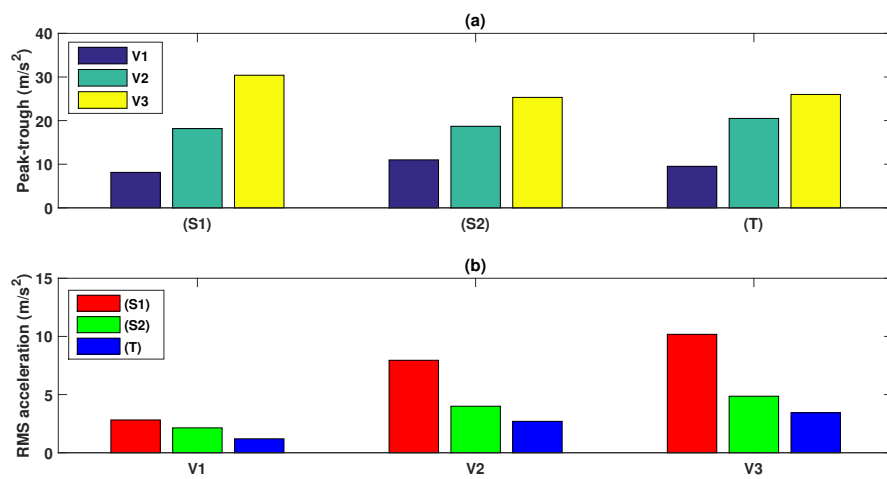


Fig. 3.10 (a) The peak-trough differences of COM's vertical acceleration and (b) RMS values of hand's 3D acceleration for different walking conditions.

Chapter 4

3D modeling of human gait

4.1 Introduction

In this chapter, we present a combined inverse dynamics and optimization method to predict natural human walking in swinging mode. Differential inclusion formulation is adopted in order to have smaller number of optimization variables and explicit formulations in terms of variables. Recent studies (Kumar et al. [157], Kaddar et al. [9]) suggested that to predict human walking with arm swinging, 3D bipedal models should be considered. Therefore, in contrast to previous studies, the simulator considers a 3D skeletal model with a high number of DOFs, which choices are made based on biomechanical observations on normal human gait. Straightforward walking motion is optimized over the step, which is considered as the gait cycle, since in healthy walking each step is very similar to the next and the overall pattern of movement repeats [158]. Step characteristics and joint motions are simultaneously predicted from only one simple gait descriptor: average walking speed, which minimizes the requirements for experimental data.

4.2 Conception of the 3D biped model equipped with hand-held device

This section introduces the geometric model of the proposed anthropomorphic bipedal system used to generate walking movements in a straight forward direction on a flat ground. Choices and assumptions about this model take into consideration biomechanical observations on human gait that are detailed in the following.

4.2.1 Biomechanical observations on normal human walking

In this section, we aim to report observations on normal human walking from biomechanical and motion analysis literature. These observations will justify our modeling choices in terms of segments definition and different defined joints DOF.

4.2.1.1 Locomotor part

Walking gait is a motor task that requires a complex sequence of active muscle to maintain stability and contribute to whole body linear progression.

4.2.1.1.1 Ankle The junction between the foot and the tibia is called ankle, where the main motions are flexion and extension in the sagittal plane [159]. In combination with heel rise, the ankle rotation constitutes a major source of forward displacement during single support phase [10]. In fact, an arc of planar flexion prepares the leg for swing phase; the ankle flexes, stored energy rolls the limb in forward direction over the toe, and flexes the knee. Another arc of dorsal flexion ensures foot take-off and advancement. During each stride, the ankle travels through an average arc of motion of 25° [160]. This motion is critical for body progression and shock absorption [10]. Besides, Correlations have been identified between the ankle's moment and produced power and the gait performance in several populations [58, 161, 162].

In our proposed model (see section 4.2.2), only abduction-adduction and dorsi/plantar flexion motions of the ankle are considered. Note that in our gait model, the pronation-supination of the swing foot is introduced by the pronation-supination of its ipsilateral hip.

4.2.1.1.2 Knee The knee is a very complex connection between the femur and the tibia that are the main segments of the locomotor part. This joint is characterized by a large range of motion in the sagittal plane and small arcs of coronal and transverse mobility [10] (cf. figure 4.1). Knee's arcs of motion lead to remarkable changes in foot and body locations. Knee mobility is crucial for normal walking patterns [10]. The limb stability in stance phase is determined by the knee. In swing phase, the knee flexibility has a significant contribution to the limb's forward progression.

The human knee joint is commonly modeled as an idealized joint based on rotations [163], in most common musculoskeletal models. A planar knee joint is considered in most clinical models [164]. In our model, the last description is considered. Small arcs of coronal and

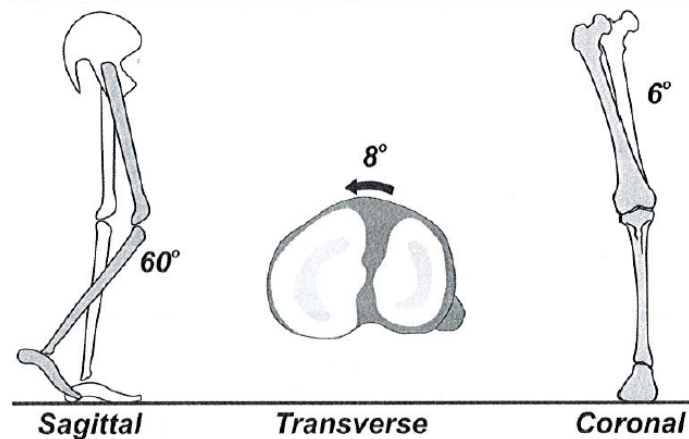


Fig. 4.1 3D knee joint rotations and arcs of motion used in normal walking: sagittal plane flexion (60°); transverse plane rotation (varying from 4° to 8° depending on subject); and coronal plane motion (4° abduction and 2° adduction) [10].

transverse mobility are not considered.

Then, in our model, we make the simplifying assumption that the knee makes no transverse rotation or coronal plane motion during the gait cycle. This reduces the complexity of the biped model without significantly affecting its validity. Only sagittal motion is considered for this joint. It represents a great range of motion from 0° to 60° flexion. During each gait cycle, the knee undergoes two waves of flexion (see figure 4.2) [4, 165–169]. The first wave (smaller flexion peak of 20°) occurs between loading response and mid stance to contribute to controlled shock absorption. The latter wave, which is larger with 60° flexion, happens during initial swing to aid foot clearance. Due to differences in walking velocity, subject individuality and landmarks chosen to indicate body segments alignment, the limits of knee flexion and extension vary across studies.

At the heel contact, the knee is relatively extended with a mean flexion of 5° . However, the normal onset posture may vary from 0° (full extension) to 10° flexion [4]. Faster gait velocities are associated with higher knee flexion at the time of IC compared to slower velocities [170].

Following the beginning of loading response, the knee promptly flexes through weight acceptance (WA). The velocity of flexion at this time approximately equals that occurring in swing phase ($300^\circ/\text{s}$). Forefoot contact at 12% of the GC completes the heel rocker and, thus, the stimulus for knee flexion ceases. At this point, stance knee is at 20° flexion and it is under

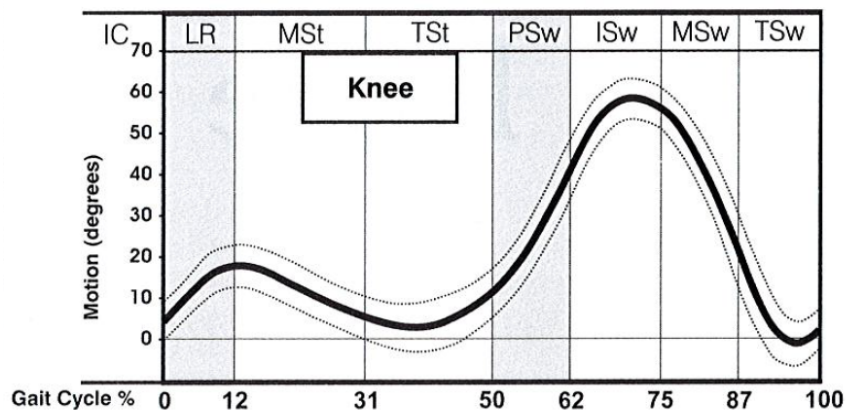


Fig. 4.2 Normal range sagittal plane motion of the knee during a GC. Black line designates the mean values, dotted lines denotes one standard deviation. Gait phase divisions are designated by vertical bars (LR: Loading Response, MSt: Mid Stance, TSt: Terminal Stance, PSw: Pre-Swing, ISw: Initial swing, MSw: Mid Swing, TSw: Terminal Swing) [10].

maximum weight-bearing load.

Walking velocity significantly influences the loading response knee flexion. Slowing the pace of walking results in a great change. For instance, with comparison to walking at 90 m/min, the locomotion at 60m/min led to 67% less knee flexion while raising the gait velocity to 120 m/min increased knee flexion by 38% [4].

With the beginning of mid stance, the knee rapidly begins to extend. The rate of motion is, however, half that of the preceding flexion. Knee joint continues toward extension during the first half of terminal stance. Minimum stance phase flexion averaging 5° is attained about halfway in terminal stance (about 39% GC) and persists for a short time before the joint slightly begins to flex again. At the end of terminal stance (floor contact by the other foot), the knee is flexed 10° . Knee flexion rapidly rises after the onset of DS configuration in pre-swing. 40° flexion is reached by the end of the phase (almost 62% GC). This mainly passive event happens as the trailing leg rolls over the anterior edge of the fore foot.

Knee continues flexing at the same fast rate during initial swing until the swing foot is opposite the support foot. At this time, maximum knee flexion averages 60° , the peak knee angle occurring throughout the GC [171]. Murray et al. [168] reported a 70° maximum flexion based on a strobe system providing only two-dimensional data. To attain this posture

in pre-swing and initial swing phases, the knee flexes at 350°/s.

During mid swing, as the swing foot advances ahead of the stance leg, less knee flexion is needed for foot take-off. Then, after a momentary pause, the knee begins to extend as rapidly as it flexed in the previous phases [170, 172]. Half of the recovery toward peak extension occurs throughout mid swing. As this phase ends, the foot is parallel with the ground and the tibia is in vertical position. Knee extension continues at the same prompt rate until foot extension (0°) is reached just before the end of the swing phase (95% GC approximately). Then the knee tends to drop into a slight degree of flexion. The final knee position at the end of terminal swing almost equals 5° flexion.

4.2.1.1.3 Hip The hip is the junction between the locomotor and passenger units. It differs from other joints in many aspects. Therefore, this joint is designed to overtly provide 3D motion. Hip motion during stance allows the pelvis and trunk to remain erect while the swing leg is moving forward over the stance limb. Sagittal plane motion involves the largest range of motion, while in the coronal and transverse planes, the motion is limited but it is substantial for walking [10].

The hip moves through two arcs of motion during the gait cycle: extension in stance and flexion during swing. The exchange from one direction to another is progressive. In the literature, the normal arc of hip motion is reported to range from 40° to 48° [171, 173–175]. Peak hip extension and flexion are considered respectively as 0° and 40° [173, 175]. Hip motion is defined combining the displacement of the thigh and pelvis. Relatively to vertical position (0°), the thigh maximum positions are 20° for extension during terminal stance and 25° for flexion in mid swing [10]. This motion is independent of the pelvic motion and ensured by the hip sagittal rotation. This motion of the hip significantly contributes to stride length [62].

In the coronal plane, the hip moves with a small magnitude of abduction and adduction as the unloaded part of the pelvis follows the swinging leg [10]. Adduction rises to 10° by the end of loading response as body weight is transferred onto the forward limb. This results from a combination of the femur displacement and contralateral pelvic drop to ensure power absorption and limb's momentum deceleration to prepare for stance [10]. The thigh gets its neutral position in the coronal plane by the middle of swing phase. In each GC, hip abduction attains a maximum of 5° just after toe-off. The abductor moment reflects the amplitude of ground reaction force during stance and counteracts contralateral pelvic drop generated by

the medial alignment of body weight. Motion pattern is similar to that of the sagittal plane but relatively small arcs of motion occur in both men and women [168].

During each GC, the limb moves through an arc of internal rotation followed by a similar arc of external rotation. Maximum internal rotation of the thigh is found at the end of the loading response and peak external rotation occurs at the beginning of swing [176]. The total arc of thigh motion in the transverse plane averages 8° [10]. When the arc is added to the pelvic rotation, total hip rotation averages 15° . Markers show similar magnitude of hip transverse motion, although there are different values among the different gait laboratories [177].

4.2.1.2 Head-Trunk-Pelvis

4.2.1.2.1 Head and trunk: single rigid body The axial core of the body is composed of three rigid structures: head, thorax, and pelvis. From a functional point of view, the head and the neck are considered as a single unit on the top of the trunk. In literature, the definition of trunk is inconsistent. It may refer to all body segments between the hip joints and the base of the neck, except the arms and the pelvis [10]. In our study, this interpretation is considered for gait modeling and analysis.

While the neck allows the head to move independently to expand one's field of vision, the head and trunk travel as one unit during normal human gait. Neither segment displays any observable change in position except that both head and trunk move up and down as the whole body center of gravity (COG) follows the limbs movements in swing and stance phases [10]. However, small arcs of displacement in both the sagittal and frontal planes have been registered by instrumented analysis.

Vertical displacement of head and trunk, shown in figure 4.3, is equal for each segment and follows a double sinusoidal path. The average amount of vertical position change is approximately 4.2 cm [53, 178, 179]. This vertical change varies with the human's walking speed, with greater amplitude for higher velocities. Thorstensson et al. reported that vertical trunk excursion varied from 2.7 cm at 90 m/min to 6.8 cm at 150 m/min [179].

Lateral displacement is also the same for head and trunk segments, averaging 4.5 cm between maximum right and left deviations. However, for each GC, the trajectory in lateral direction is a single sinusoid [179], (see figure 4.4).

Thus, we can model both trunk and head by a single rigid body.

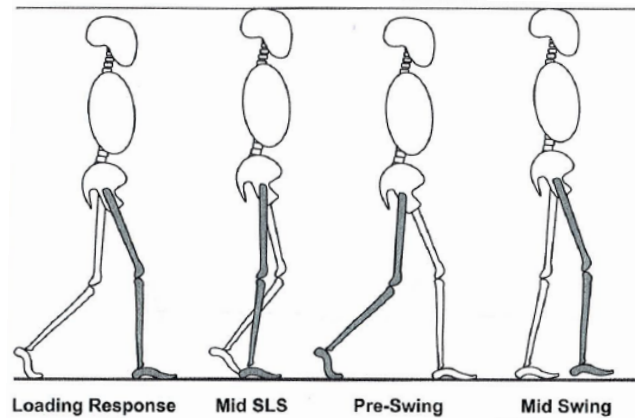


Fig. 4.3 Vertical displacement of the trunk indicated by head height. It is highest in mid single limb stance (SLS) and mid swing and lowest in DS configurations (loading response and pre-swing) [10].

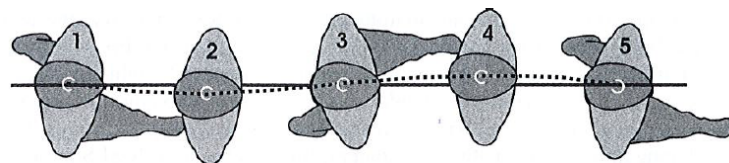


Fig. 4.4 Lateral displacement of the trunk during walking indicated by head location. It is midline during DS phases (1, 3 and 5), displacement to left during left SS (4), and displacement to right during right SS (2) [10].

4.2.1.2.2 Pelvis The greatest amount of motion in the passenger unit occurs at the pelvis. It rotates in all three planes during each GC (cf. figure 4.5). These rotations are induced by the motion of the hip acting like a three DOF ball and socket joint. Small arcs of motion representing a continuous postural pattern are observed in sagittal and frontal planes (4°). For normal men walking, the pelvis rotates through a total arc of motion of 10° in the transverse plane [168]. A significant contribution to the step length of the front leg is ensured by a peak forward rotation of 5° during terminal swing and IC. A peak backward rotation of 5° occurs in terminal stance leading to a trailing leg posture. Mid swing and mid stance transition phases correspond to a null axial rotation of the pelvis.

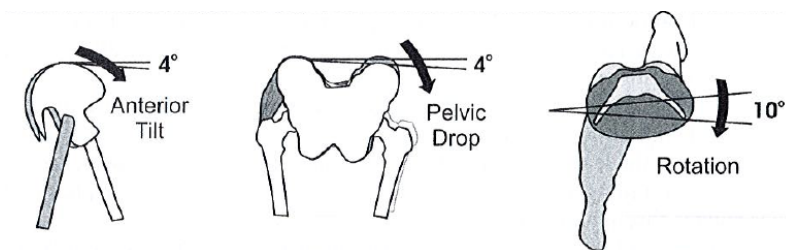


Fig. 4.5 Arcs of motion of the pelvis during a stride: 4° for Anterior tilt, 4° for contralateral pelvic drop, and 10° for the transverse rotation [10].

4.2.1.3 Arms

During each stride, reciprocal dynamic arm swing spontaneously takes place. Arm swing angular momentum in the three anatomical planes is calculated by Elftman [130]. It was found that arm motion pattern is opposite to that of the rest of the body. This calculation is challenged by the findings of energy cost analysis. No differences in oxygen usage is found when walking with free or bound arms [180]. These two results imply that arm swing may be useful to walking but it is not a crucial element of it. Arms flex and extend during walking (cf. figure 4.6). Timing offset between the two upper limbs is 50% of GC, with maximal extension happening when the leg is swinging forward and maximal flexion occurring with contralateral IC. Each limb (arm and leg) moves across a proportionate arc of motion (40° for hip, 32° for shoulder [10]). Thus, the arm is giving a specific counterforce to reduce the whole body rotatory displacement induced by locomotor system mechanics, just as calculated by Elftman [130]. The amount of extension and flexion varies considerably among individuals. The total arc of motion increases when walking faster [10].

4.2.1.3.1 Shoulder During moderate velocity walking (92 m/min), the upper arm rotates with respect to the torso with an average arc of 32° . At the beginning of the stance phase, the

shoulder has peak extension (24°) and then is positioned in 8° flexion position by the end of terminal stance at the next foot-ground collision [10] (see figures 4.6 and 4.7).

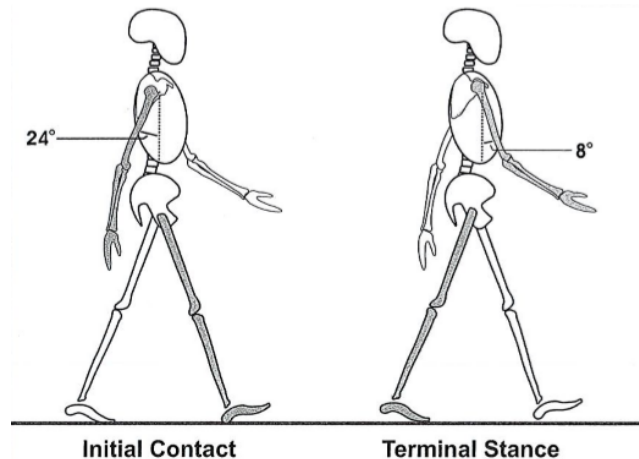


Fig. 4.6 Natural arm swing during free walking. Maximum backward swing (24°) corresponds to IC while peak forward swing (8°) corresponds to terminal stance [10].

The total arc of motion increases with faster velocities [10]. For instance, during gaits at a rapid velocity of 7.7 km/h, the average arc of motion is 39° . At this fast speed, peak shoulder extension increases (maximum of 31°) while maximum shoulder flexion remains unchanged (8°) compared to the motion occurring during moderate speed walking (5.5 km/h). So modeling shoulder rotation in sagittal plane is necessary to have realistic upper limbs movements' patterns. Considering our active arm swing hypothesis, the increased upward rotative acceleration of the shoulder in the sagittal plane leads to increasing its internal rotation in the transverse plane, as the upper limbs tends to counteract the moments produced by the swing lower limbs [126]. Chapman et al. [181] observed a decrease in the amplitude of shoulder transverse rotation with increase in walking velocity when studying walking with different speeds for 10 young men and 10 young women. This trend is noted for 15 subjects over 20. No great difference in transverse rotation range is found between men and women. This transverse rotation is represented in our model by roll angles of each shoulder (q_{17} and q_{21} in figure 4.12).

4.2.1.3.2 Elbow The elbow has a similar excursion pattern as the shoulder. During each stride, an extension motion occurs in ipsilateral swing phase and a flexion arc is produced in ipsilateral stance phase [10]. During moderate and rapid gait, the average magnitude of flexion of the elbow is 30° and 40° , respectively [10]. These ranges are comparable to those of the shoulder joint. The difference is that the elbow remains in flexion position throughout

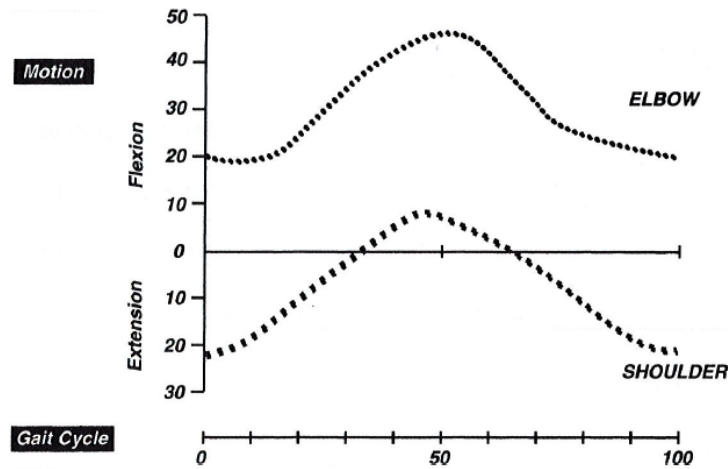


Fig. 4.7 Patterns of shoulder and elbow motion during arm swing for a GC. Horizontal scale indicates % GC beginning with IC [10].

all the GC. Therefore, the flexion position reach its peak at the time of contralateral foot contact with the floor (e.g. 47° at 5.5 km/h; 55° at 7.7 km/h; see figure 4.7). Flexion motion of the elbow is considered in our model (q_{19} and q_{23} angles in figure 4.12). Note that during GC, the transverse rotation of the forearm is introduced by the roll motion of the upper arm generated by the shoulder joint.

4.2.2 Presentation of the 3D bipedal model

Human gait is a complex dynamic activity since human structure has high DOF, and a complex mechanical structure [182]. In order to achieve a human-like natural gait, human's structure and movements has to be modeled accurately. Since the human's gait is composed of dynamic motions of three planes which are sagittal, frontal and transverse (see figure 4.8), the complete bipedal gait can be obtained only if it is analyzed in two or more planes [182].

In this context, an anthropomorphic bipedal model with 19 DOF is proposed to generate realistic walking gaits for human locomotion at the level of locomotor members as well as upper limbs. Such a structure will enable us to get walking movements in the three principal planes mentioned above.

Each lower member has a set of three main bodies (thigh, leg, foot) connected by joints replicating six functional mobilities. These mobilities are distributed as three articulations in the hip, one in the knee, and two in the ankle. The three DOF grouped on the hip joint (ball joint) allow flexion-extension movements, adduction-abduction and internal-external rotation. The knee can simply perform flexion-extension movement. For the ankle, only rotations in

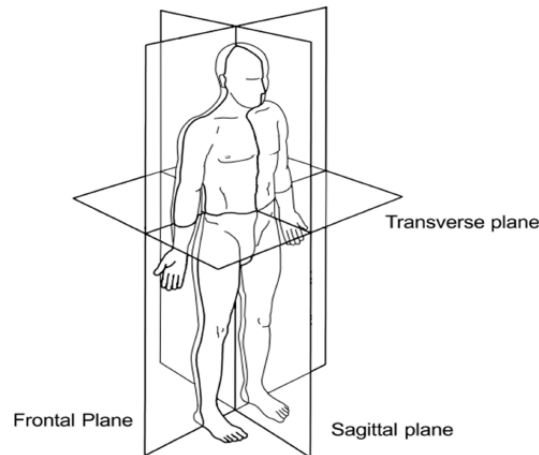


Fig. 4.8 The three reference planes in zoological anatomy in the standard human anatomical position: frontal, sagittal and transverse planes [10].

the sagittal plane (around pitch axis) and the frontal plane (around roll axis) are allowed.

The proposed linkage of locomotive members by revolute joints, all actuated (active), will enable to restore three-dimensional walking patterns. This kinematic chain, which defines a 12 DOF locomotor system, will constitute the kinematic model for studying the 3D human walking for the lower part of human body. This model is inspired from the 14 DOF system used in [183] to test optimal walking trajectories for robot design. In our application, the model is simplified to 12 DOF by not considering the ankle rotation in the transverse plane (about the yaw axis).

The axial core of the model consists of three rigid links: head-neck, trunk, and pelvis. The head-neck segment is longitudinally defined from the Head Vertex (HV) to the Cervical Joint Centre (CJC). The trunk refers to body segments between the CJC and the Lumbar Joint Centre (LJC). As to the pelvis, it is specified from the LJC to the projection of the Hip Joint Centre (HJC) in sagittal plane. More details about these anatomical definitions can be found in [4]. The pelvis and torso can have relative rotation about their longitudinal axis. In contrary, we assume that there is no rotation between the trunk and head-neck segments. Thus, in our gait model, head-neck and trunk travel as a single unit throughout the displacement of whole body COM. Note that these two segments are differentiated in the geometric representation in order to model the distal segments linking the upper extremity of the trunk to the shoulders centers.

Each upper limb is modeled by two-link arms i.e. each composed of an upper arm and a forearm. Each hand is considered as a point mass fixed to the forearm, and its mass and inertial properties are merged with those of the forearm segment. Shoulders and elbows are presented respectively by two DOF and one DOF rotoid connections. Abduction-adduction (coronal plane movements) and flexion-Extension movements (in sagittal plane) can be performed on the shoulders. Only flexion-Extension movements (in the sagittal plane) are enabled for elbows.

4.2.2.1 Geometric description of the 3D biped

The studied anthropomorphic model is illustrated in figure 4.11. All links are considered as rigid, and connected by frictionless joints. All the articulations are revolute. The biped is composed of a head-neck, torso, pelvis, two identical two-link arms with three DOF, and two identical three-link legs with three DOF spherical hips ended with feet bodies. Each knee and elbow contains a one DOF revolute joint. The trunk and pelvis are connected by a revolute joint with one DOF.

The methodology used to describe the biped morphology is based on setting tools developed for typical robot manipulators. In SS phase, the base is the support foot and the end effectors are the oscillating foot, forearms and head end points. Therefore, the model is considered as a tree structure with four open serial kinematic chains (one chain terminated with the swing leg, one chain ending in the head and two chains corresponding to the upper limbs), whose base is the stance foot. We assume that, in SS phase, the stance foot do not take off or slide over the surface and that it makes no motion around yaw axis. In double support configurations, the kinematic chain corresponding to the locomotor system become closed. Thus we have a hybrid structure composed of a parallel structure which bases are the feet and the end effector is the pelvis, in addition to the three serial chains beginning from the pelvis through the torso ending in the three end effectors (head and forearms).

The proposed tree structure is composed of 13 main bodies and 13 virtual bodies which allows to decompose the revolute joints in a chain of joints with one DOF and to depict the distal links dimensions. Then, the whole system consists of $N=26$ bodies, denoted C_0, \dots, C_{N-1} and $N - 1$ revolute joints, $j = 1, \dots, N-1$. The body C_0 refers to the biped's support foot. C_j body is articulated by the articulation j i.e. the joint j connects the body C_j to $C_{a(j)}$ body, where $a(j)$ denotes the index of the predecessor body of C_j in the kinematic chain (see figure

4.9).

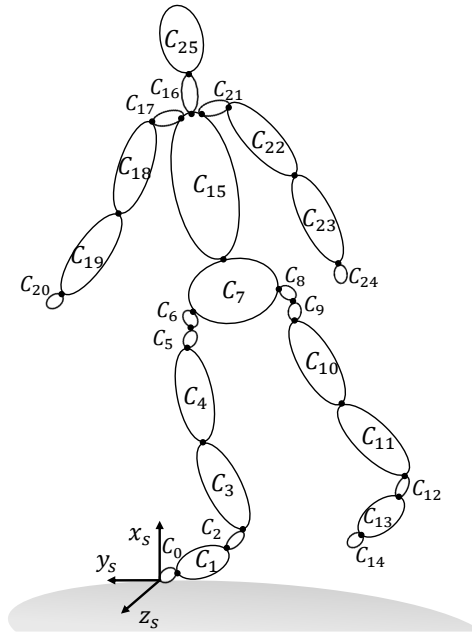


Fig. 4.9 The 3D biped as a tree structure, consisting in $N=26$ bodies and 25 joints. $N_j=19$ joints are variable and the other five joints are fixed. The fixed joints correspond to the virtual bodies added to represent end bodies dimensions as well as the segments relating the trunk to shoulders. The fat bodies represent the main bodies, whereas the thin bodies are fictional bodies (mass, inertias and dimensions are null), they are required to describe the biped through series of one DOF joints.

4.2.2.2 System parametrization

The parametrization of the kinematic chain leads to the introduction of a configuration vector \mathbf{q} with $N_j = 19$ joint variables q_j . The homogeneous description of the articular chain, with a minimum number of parameters, requires the establishment of local frames throughout the tree structure.

The modified convention of Denavit-Hartenberg [184] proposed by Khalil and Kleinfinger [11] was chosen for geometric modeling of the anthropomorphic biped. For this, a coordinate system is attached to each segment. The frame $(O_k - \mathbf{x}_k, \mathbf{y}_k, \mathbf{z}_k)$, denoted R_k , is rigidly attached to the joint k , as shown in figure 4.10. The joint k connects both segments $(k-1)$ and k . The axis \mathbf{z}_k represents the axis of the joint k . Additionally, the origin of R_k , denoted O_k is located at a point where the common normal to \mathbf{z}_k and \mathbf{z}_{k-1} crosses \mathbf{z}_k , whereas the normal

common axis defines \mathbf{x}_k . Moreover, the axis \mathbf{y}_k is such that the axis \mathbf{x}_k , \mathbf{y}_k and \mathbf{z}_k form a direct orthonormal system. This coordinate system is called DH frame. Note that the frame attached to the fixed link (i.e. $O_s - \mathbf{x}_s, \mathbf{y}_s, \mathbf{z}_s$) can be chosen arbitrarily and therefore we can choose the axis \mathbf{z}_s towards the displacement direction (see figure 4.11). Once bodies' frames are established according to these conventions, the relative position and orientation between each two successive frames, R_{k-1} and R_k can be specified using four parameters known as DH parameters. These parameters are illustrated in figure 4.10, they are defined as:

- the twist angle α_k about \mathbf{x}_{k-1} , from \mathbf{z}_{k-1} to \mathbf{z}_k ,
- the body length d_k from \mathbf{z}_{k-1} to \mathbf{z}_k along \mathbf{x}_{k-1} ,
- the joint offset r_k , which is the distance from \mathbf{x}_{k-1} to \mathbf{x}_k along \mathbf{z}_k , and
- the joint angle θ_k , which is the angle between \mathbf{x}_{k-1} to \mathbf{x}_k about \mathbf{z}_k .

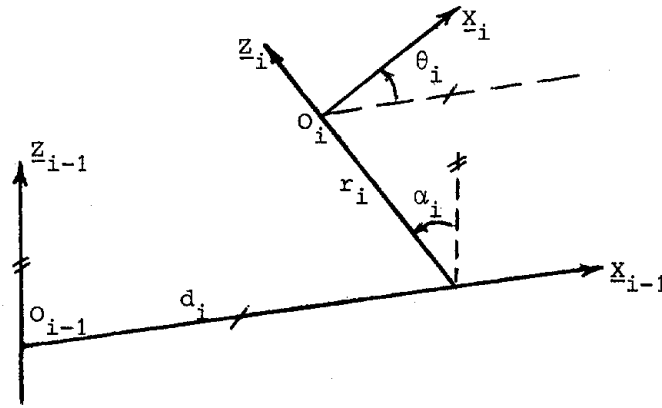


Fig. 4.10 The Denavit-Hartenberg notation modified by Khalil and Kleinfinger [11].

According to the type of joints, i.e. prismatic or revolute, r_k or θ_k is the variable parameter while the other parameters are constant. Since in the case of our model only rotations are possible, only the parameter θ_k will be variable.

Based on the above definition of DH parameters, the 4×4 homogeneous transformation matrix ${}^{k-1}\mathbf{T}_k$ describing the coordinate transformation from R_{k-1} to R_k is given by the multiplication of the matrices corresponding to elementary transformations:

$${}^{k-1}\mathbf{T}_k = \mathbf{Trans}(\mathbf{x}, d_k) \mathbf{Rot}(\mathbf{x}, \alpha_k) \mathbf{Trans}(\mathbf{z}, r_k) \mathbf{Rot}(\mathbf{z}, \theta_k) \quad (4.1)$$

Thus, the DH matrix ${}^{k-1}\mathbf{T}_k$ can be expressed as [11]:

$${}^{k-1}\mathbf{T}_k = \begin{bmatrix} c\theta_k & -s\theta_k & 0 & d_k \\ c\alpha_k s\theta_k & c\alpha_k c\theta_k & -s\alpha_k & -r_k s\alpha_k \\ s\alpha_k s\theta_k & s\alpha_k c\theta_k & c\alpha_k & r_k c\alpha_k \\ 0 & 0 & 0 & 1 \end{bmatrix} = \begin{bmatrix} {}^{k-1}\mathbf{R}_k & {}^{k-1}\mathbf{P}_k \\ 0 & 0 & 0 & 1 \end{bmatrix} \quad (4.2)$$

where $c\theta_k = \cos(\theta_k)$, $s\theta_k = \sin(\theta_k)$, ${}^{k-1}\mathbf{R}_k$ is the 3×3 orientation matrix defining the orientation of R_k with respect to R_{k-1} , and ${}^{k-1}\mathbf{P}_k$ is the 3×1 vector representing the relative position between the two frames R_{k-1} and R_k .

Table 4.1 Modified Denavit-Hartenberg parameters of the 3D biped.

j	$a(j)$	α_j	θ_j	r_j	d_j
0	s	0	0	0	0
1	0	0	q_1	$-L_1$	L_2
2	1	$\frac{\pi}{2}$	q_2	0	0
3	2	0	q_3	0	L_3
4	3	0	q_4	0	L_4
5	4	$-\frac{\pi}{2}$	$q_5 - \frac{\pi}{2}$	0	0
6	5	$\frac{-\pi}{2}$	q_6	0	0
7	6	0	0	0	$\frac{L_5}{2}$
8	7	0	q_8	0	$\frac{L_5}{2}$
9	8	$\frac{\pi}{2}$	$q_9 - \frac{\pi}{2}$	0	0
10	9	$\frac{-\pi}{2}$	q_{10}	0	0
11	10	0	q_{11}	0	L_4
12	11	0	q_{12}	0	L_3
13	12	$\frac{\pi}{2}$	q_{13}	0	0
14	13	0	0	L_1	L_2
15	7	0	q_{15}	L_6	0
16	15	0	0	L_7	0
17	16	$\frac{\pi}{2}$	$q_{17} + \frac{\pi}{2}$	0	$-L_8$
18	17	$\frac{\pi}{2}$	q_{18}	0	0
19	18	0	q_{19}	0	$-L_9$
20	19	0	0	0	$-L_{10}$
21	16	$\frac{\pi}{2}$	$q_{21} + \frac{\pi}{2}$	0	L_8
22	21	$\frac{\pi}{2}$	q_{22}	0	0
23	22	0	q_{23}	0	$-L_9$
24	23	0	0	0	$-L_{10}$
25	16	0	0	L_{11}	0

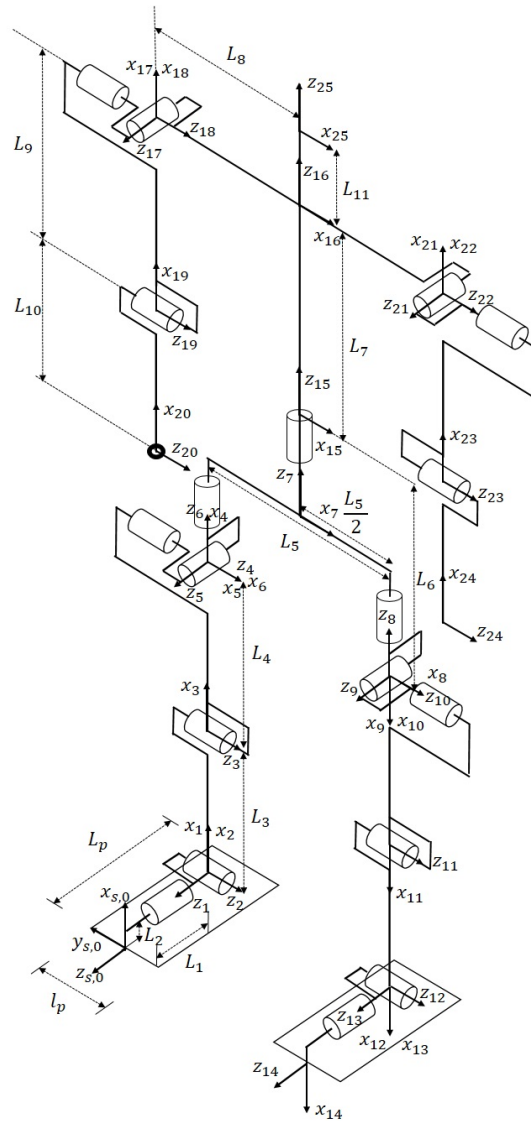


Fig. 4.11 Local frames related to the main bodies of the 3D biped, according to Khalil-Kleinfinger convention [12].

According to the Denavit–Hartenberg convention, the DH frames positions are defined in figure 4.11. The corresponding geometric parameters are presented in Table 4.1. The vector of the N_j+3 generalized coordinates is three DOF for support foot translations (x_p , y_p and z_p) with

$$\mathbf{q} = q_{j \in ind_j} \in \mathbb{R}^{N_j} \quad (4.3)$$

where $ind_j = [1, 2, 3, 4, 5, 6, 8, 9, 10, 11, 12, 13, 15, 17, 18, 19, 21, 22, 23]$ contains the indexes of actuated joints. The absolute angles q_1 and q_2 are respectively the roll and pitch angular positions of the stance leg's ankle. The variable angles q_{12} and q_{13} are respectively the pitch

and roll motions of the swing leg's ankle. The variables q_3 and q_{11} describe the joint angles of the support leg and swing leg knees, respectively. The variable angles q_4 , q_5 and q_6 are the angles defining the spherical joint at the stance leg hip. Similarly, the three DOF swing leg hip is defined by the variables q_8 , q_9 and q_{10} . The variable q_{15} is the articular angle to describe the yaw rotation of the trunk relatively to the pelvis. The variables q_{17} and q_{18} describe the roll and pitch motions of the stance leg's ipsilateral arm (right side pictured in figure 4.11) with respect to the trunk. The angles q_{21} and q_{22} are the joint variables of the contralateral shoulder, respectively about roll and pitch axes. The variables q_{19} and q_{23} denote elbows angles in the sagittal plane. Note that all joints are independently actuated.

L_p and l_p define the foot dimensions. L_i , $i = 1, \dots, 11$ denote the biped dimensions (see figure 4.11 and figure 4.12). L_1 and L_2 define the position of the ankle center with respect to the toe end. L_3 and L_4 are the length of each shank and thigh respectively. L_5 represents the distance between hips centers along the transverse axis. L_6 , L_7 , and L_{11} are the longitudinal lengths of pelvis, trunk, and head-neck segments respectively. The dimensions of the arms and the forearms are respectively given by L_9 and L_{10} . L_8 is the distance between each shoulder center and the trunk segment.

4.3 Gait cycle definition

4.3.1 Gait cycle composed of a single support phase and instantaneous impact

In the model, we consider that the biped gait is periodical and that the step is considered as its cycle. The walking cycle is composed of a single support phase (one foot is on the ground and the other is swinging from the back to the front) and a double support phase at its end (cf. figure 4.13). Double support phase is supposed to be instantaneous. The initial configuration is a double support configuration, in which both feet are on the ground, and oriented in walking direction as we consider straightforward walking gait scenarios. The absolute frame R_s ($O_s - \mathbf{x}_s, \mathbf{y}_s, \mathbf{z}_s$) is attached to the right foot which is assumed to be the stance foot during gait cycle.

In initial double support, we assume that the rotation of the pelvis in frontal plane is null. Besides, the axial rotation of the torso in this instantaneous phase is defined so that it compensates the transverse rotation of the pelvis, in order to keep the head pointing forward.

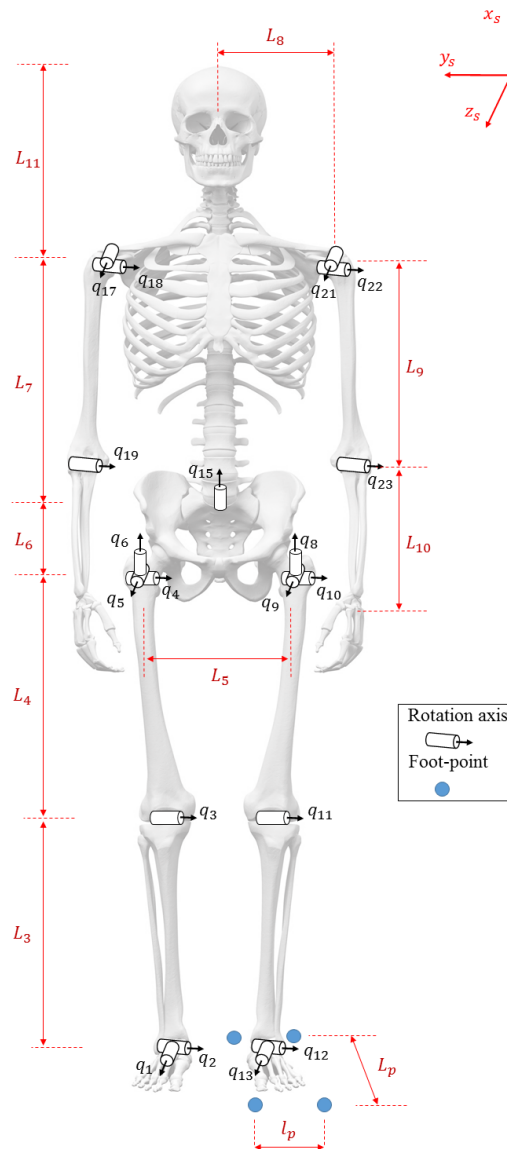


Fig. 4.12 The 19 DOF human linkage model with joint rotations (denoted by cylinders) and dimensions ($l_p, L_p, L_i, i = 1, \dots, 11$).

Considering a cyclic gait motion over a right step (where the support foot is the right foot) of length d_1 and width w , in a time interval of $[0, T_1]$, the configurations during the second step i.e. left step are deduced using the following transformations:

- Multiplication of configurations vectors by the switching matrix \mathbf{E} , that will be presented in section 4.3.2, to express the symmetric role of legs and arms from one step to another;

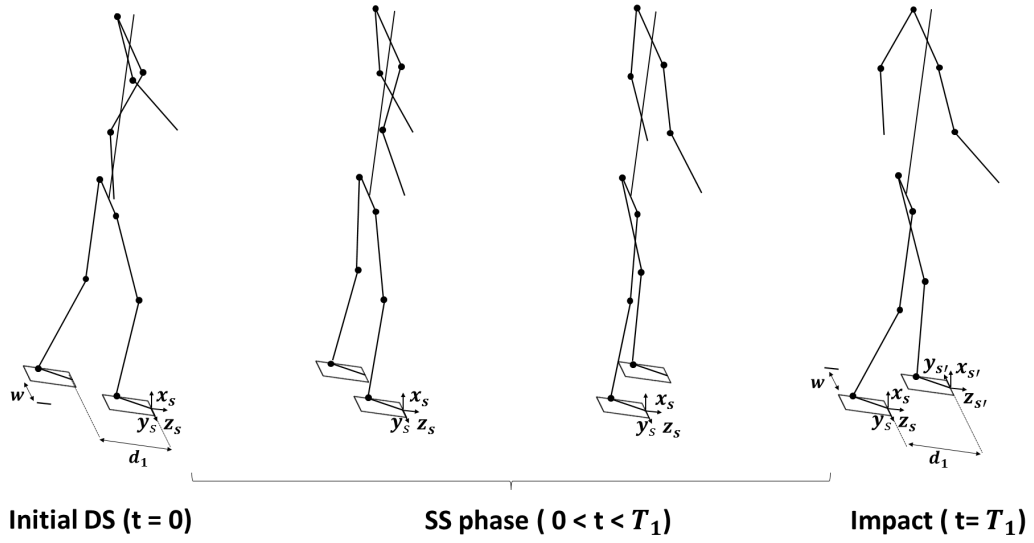


Fig. 4.13 GC composed of a SS phase and an instantaneous impact.

- Multiplication of coordinates vectors by the following transformation matrix:

$${}^s\mathbf{T}_{s'} = \begin{bmatrix} {}^s\mathbf{R}_{s'} & {}^s\mathbf{P}_{s'} \\ 0 & 1 \end{bmatrix} = \begin{bmatrix} 1 & 0 & 0 & 0 \\ 0 & -1 & 0 & -w \\ 0 & 0 & 1 & d_1 \\ 0 & 0 & 0 & 1 \end{bmatrix} \quad (4.4)$$

where ${}^s\mathbf{P}_{s'}$ reflects the translation of reference frame from right foot toe to landed left foot toe and ${}^s\mathbf{R}_{s'}$ is the rotation matrix used to direct the $y_{s'}$ axis of the new reference frame $R_{s'}$ towards the outside of the left foot (cf. figure 4.13).

Note that step length and width are optimized in step-level optimization process and they are determinant variables in calculating the locomotor system configuration in double support.

4.3.2 Switching matrix

For each step, the position of the reference frame is shifted so that it remains linked to the stance foot. Thus, we can assume that there is an exchange of role of the biped's articulations after the impact. This marks the beginning of next swinging phase. In order to express this exchange, a switching matrix must be used.

We first define the switching matrices for the locomotor system and the arms. The 12×12 anti-diagonal matrix describing the exchange of role of legs from a current step j to the next step $j+1$ is defined as:

$$\mathbf{E}_{loc} = \begin{bmatrix} \mathbf{0}_{6 \times 6} & \mathbf{E}_l^\top \\ \mathbf{E}_l & \mathbf{0}_{6 \times 6} \end{bmatrix} \quad (4.5)$$

where \mathbf{E}_l is an anti-diagonal matrix of dimension 6×6 expressing the left leg joint angles providing the same leg configuration as a given right leg joint angles, it is defined as:

$$\mathbf{E}_l = \begin{bmatrix} \mathbf{0}_{2 \times 1} & \mathbf{0}_{2 \times 3} & \mathbf{J}_2 \\ \mathbf{0}_{3 \times 1} & -\mathbf{J}_3 & \mathbf{0}_{3 \times 2} \\ \mathbf{J}_1 & \mathbf{0}_{1 \times 3} & \mathbf{0}_{1 \times 2} \end{bmatrix} \quad (4.6)$$

in which \mathbf{J}_n is an anti-diagonal identity matrix of dimension $n \times n$.

Similarly, there is an exchange of role of the arms after the impact and the right arm configuration just before the impact $\mathbf{q}_{j,14:16}(T_j)$ is given as function of the left arm configuration just after the impact $\mathbf{q}_{j+1,17:19}(t=0)$ as:

$$\mathbf{q}_{j,14:16}(T_j) = \mathbf{E}_a \cdot \mathbf{q}_{j+1,17:19}(t=0) \quad (4.7)$$

where \mathbf{E}_a is an anti-diagonal matrix of dimension 3×3 expressing the left arm joint angles providing the same arm configuration as a given right arm joint angles, it is given by:

$$\mathbf{E}_a = \begin{bmatrix} -1 & 0 & 0 \\ 0 & 1 & 0 \\ 0 & 0 & 1 \end{bmatrix} \quad (4.8)$$

The 6×6 matrix describing the exchange of role of arms from a current step to the next step is defined as:

$$\mathbf{E}_{arm} = \begin{bmatrix} \mathbf{0}_{3 \times 3} & \mathbf{E}_a \\ \mathbf{E}_a & \mathbf{0}_{3 \times 3} \end{bmatrix} \quad (4.9)$$

Then, the 19×19 switching matrix for the whole biped can be expressed as function of switching matrices for the locomotor system and the arms as:

$$\mathbf{E} = \begin{bmatrix} \mathbf{E}_{loc} & \mathbf{0}_{12 \times 1} & \mathbf{0}_{12 \times 6} \\ \mathbf{0}_{1 \times 12} & -1 & \mathbf{0}_{1 \times 6} \\ \mathbf{0}_{6 \times 12} & \mathbf{0}_{6 \times 1} & \mathbf{E}_{arm} \end{bmatrix} \quad (4.10)$$

See appendix B for an overview of this matrix with the dimension 19×19 .

In order to provide a continuous walking behavior, we use this orthogonal matrix to calculate the final joint positions of each step from the initial joint positions of the following step:

$$\begin{aligned}\mathbf{q}_1(T1) &= \mathbf{E} \cdot \mathbf{q}_2(t = 0) \\ \mathbf{q}_2(T2) &= \mathbf{E} \cdot \mathbf{q}_1(t = 0)\end{aligned}\tag{4.11}$$

Similarly, the joint velocities we get from the impact model are relabeled in order to find the initial joint velocities for the next step.

4.4 Dynamic and impact models

4.4.1 Dynamic modeling using Newton-Euler formalism

A walking cycle is described by several phases to generate dynamically stable gait patterns, involving prompt movements of the bodies of the bipedal structure. Therefore, a dynamic model is necessary to represent the evolution of different body links. Here, we use the Newton-Euler algorithm to limit the time of computation when solving the dynamic model of the 3D biped. The formalism of Newton-Euler is based on the balance of forces for each body.

4.4.1.1 Dynamic model in single support

During single support phases, the support foot in flat contact with the ground cannot move i.e., there is no sliding or taking off motion. The configuration of the biped in single support is described by the vector of generalized coordinates:

$$\mathbf{q} = (q_1, \dots, q_{N_j})^\top \in \mathbb{R}^{N_j}\tag{4.12}$$

where $(q_i)_{1 \leq i \leq N_j}$ defined as in (4.3), denote the relative angles of the articulations.

The inverse dynamic model which defines the relation between the torques (and/or forces) applied to the actuators and the joint configurations, rates and accelerations, is represented by the equation of form:

$$\mathbf{\Gamma} = \text{IDM}(\mathbf{q}, \dot{\mathbf{q}}, \ddot{\mathbf{q}})\tag{4.13}$$

where:

- $\mathbf{\Gamma} = (\Gamma_1, \dots, \Gamma_{N_j})^\top \in \mathbb{R}^{N_j}$ is the vector of joint actuation torques;

- $\dot{\mathbf{q}} = (\dot{q}_1, \dots, \dot{q}_{N_j})^\top \in \mathbb{R}^{N_j}$ is the vector of joint velocities;
- $\ddot{\mathbf{q}} = (\ddot{q}_1, \dots, \ddot{q}_{N_j})^\top \in \mathbb{R}^{N_j}$ is the vector of joint accelerations;

4.4.1.2 Zero Moment Point position

4.4.1.2.1 ZMP definition Let us consider a support foot on the ground (figure 4.14). Let the ankle of the support foot be defined by the point A such that:

$${}^0\mathbf{OA} = (-L_1 \ 0 \ L_2)^\top \quad (4.14)$$

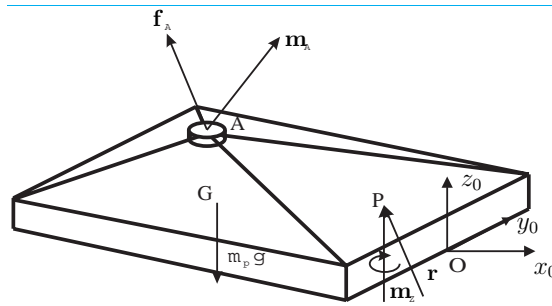


Fig. 4.14 Forces and moments acting on the support foot of a humanoid robot [13].

The action of the biped on the point A is defined by a force \mathbf{f}_A and a moment \mathbf{m}_A . If the foot does not slide on the ground, then the friction forces between the ground and the sole are such that the components (r_x, r_y) in the contact plane of the ground reaction force \mathbf{r} on the sole of the foot compensate the horizontal component of the force \mathbf{f}_A . The vertical component m_z of the moment of ground reaction forces on the sole of the foot \mathbf{m} compensates for the vertical component of the moment \mathbf{m}_A as well as that of the moment induced by the force \mathbf{f}_A . Since the contact between the ground and the foot base is unilateral, the horizontal components of the active moments can only be compensated for by changing the position of the application point P of the force \mathbf{r} inside the base of support (BOS) at each instant. A necessary and sufficient condition to ensure that there is no tilting of the humanoid robot's support foot is therefore that for the point P of the sole, where the reaction force \mathbf{r} is applied, the horizontal components of \mathbf{m} are equal to:

$$\begin{aligned} m_x &= 0 \\ m_y &= 0 \end{aligned} \quad (4.15)$$

This point P is called Zero Moment Point (ZMP) [13]. It is the point of application of the resulting force of the distributed loads that characterize the contact between the foot and the ground. It has a major role in the analysis, synthesis and control of gaits for humanoid robots. Its first practical application was the realization of the dynamic balance for the biped WL-10RD during a walking task, in 1984 [185].

4.4.1.2.2 Calculation of ZMP position The resultant of non-contact forces driven by inertia and gravity \mathbf{R}^{IGF} is given by:

$$\mathbf{R}^{\text{IGF}} = m\mathbf{g} - m\ddot{\mathbf{x}}_{\text{COM}} \quad (4.16)$$

where $\ddot{\mathbf{x}}_{\text{COM}}$ is the instantaneous acceleration of the body's COM, \mathbf{g} is the gravitational acceleration, and m is the body's total mass.

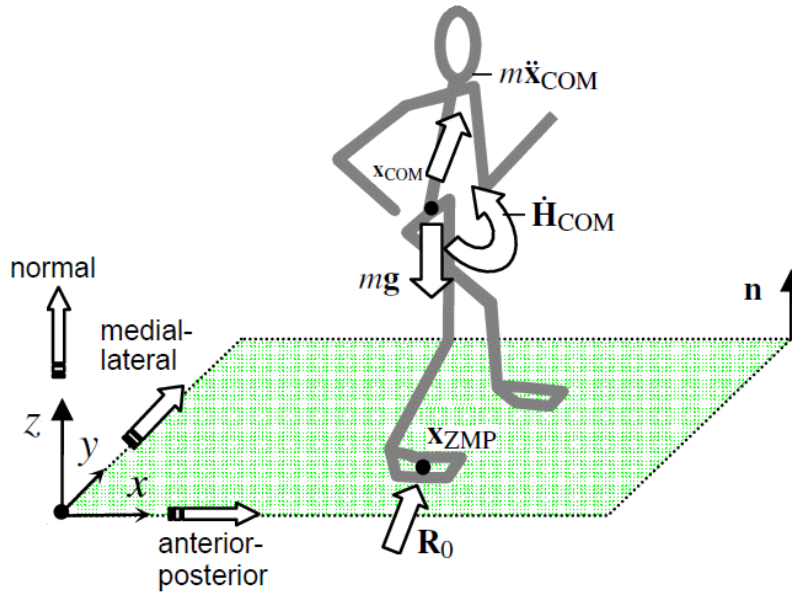


Fig. 4.15 Forces exerted on the biped during walking: ground reaction forces \mathbf{R}_0 , inertial force $(-m\ddot{\mathbf{x}}_{\text{COM}})$, inertial moment $(-\dot{\mathbf{H}}_{\text{COM}})$ and gravity force $m\mathbf{g}$ [14].

The resultant moment of \mathbf{R}^{IGF} about the ZMP (point \mathbf{x}_{ZMP} in figure 4.15) is expressed as:

$$\mathbf{M}_{\text{ZMP}}^{\text{IGF}} = (\mathbf{x}_{\text{COM}} - \mathbf{x}_{\text{ZMP}}) \times \mathbf{R}^{\text{IGF}} - \dot{\mathbf{H}}_{\text{COM}} \quad (4.17)$$

in which \mathbf{x}_{COM} and \mathbf{x}_{ZMP} are respectively the instantaneous COM and ZMP positions, and $\dot{\mathbf{H}}_{\text{COM}}$ is the rate of angular momentum about \mathbf{x}_{COM} . If the point denoted O is the origin of a Cartesian coordinate system that lies on the ground plane (cf. figure 4.15), the resultant

moment about this point, denoted $\mathbf{M}_O^{\text{IGF}}$, is given as:

$$\mathbf{M}_O^{\text{IGF}} = \mathbf{x}_{\text{COM}} \times \mathbf{R}^{\text{IGF}} - \dot{\mathbf{H}}_{\text{COM}} \quad (4.18)$$

Equation (4.17) can thus be rewritten as:

$$\mathbf{M}_{\text{ZMP}}^{\text{IGF}} = \mathbf{M}_O^{\text{IGF}} - \mathbf{x}_{\text{ZMP}} \times \mathbf{R}^{\text{IGF}} \quad (4.19)$$

Since the tipping moment of \mathbf{R}^{IGF} about \mathbf{x}_{ZMP} is null, one can write:

$$\begin{aligned} \mathbf{0} &= \mathbf{n} \times \mathbf{M}_{\text{ZMP}}^{\text{IGF}} \\ &= \mathbf{n} \times \mathbf{M}_O^{\text{IGF}} + (\mathbf{n} \cdot \mathbf{x}_{\text{ZMP}}) \mathbf{R}^{\text{IGF}} - (\mathbf{n} \cdot \mathbf{R}^{\text{IGF}}) \mathbf{x}_{\text{ZMP}} \end{aligned} \quad (4.20)$$

where \mathbf{n} is a unit vector normal to ground plane. Since ZMP is in the ground plane, $\mathbf{n} \cdot \mathbf{x}_{\text{ZMP}} = 0$ and the ZMP's position vector in the Cartesian reference system is obtained from equation (4.20) as follows:

$$\mathbf{x}_{\text{ZMP}} = \frac{\mathbf{n} \times \mathbf{M}_O^{\text{IGF}}}{\mathbf{n} \cdot \mathbf{R}^{\text{IGF}}} \quad (4.21)$$

4.4.2 Impact modeling

At the end of single support phase, the swinging foot gets in contact with the ground and the velocity of the previous stance foot may be different from zero. Since the biped's segments are rigid and non-deformable, the contact between the foot and the ground is inelastic such that the legs do not slip. The studied impact model is impulsive [186, 187].

During the impact, the forces are considered with a very high amplitude during an infinitely small time period Δt . The impulsive forces are then presented as the integral of the contact forces during the time interval Δt . Moreover, Δt is assumed to be small enough so that there is no position variation during the impact [188] and the impulsion forces can be defined by a Dirac function of magnitude equal to impulsive reaction magnitude [189].

Impulsive impact model is used to determine the velocities just after the impact of the swing foot with the ground, as well as the impulsive forces, for given joint positions and velocities just before the impact. The following hypotheses are taken into account:

- The impact is instantaneous at the instant the flat contact between the advancing foot and the ground;
- The biped's configuration is constant during impact;

- There is an instantaneous variation of joint velocities at the impact.

The impact model is obtained by integration of dynamics during the infinitesimal time Δt . The dynamic model must take into account contact forces on both feet, and consider any linear and angular velocities of both feet. The previous stance foot may leave the ground due to the impact. In the following paragraph, we introduce the extended dynamic model allowing to deduce the impact equations.

4.4.2.1 Dynamic model in double support

The 3D biped has a kinematic model with $N_j = 19$ DoF. In this dynamic model we will describe the configuration of the biped by $(N_j + 6)$ variables to be able to take into account any velocity of the foot in support. To be consistent with the determination of the dynamic model with the Newton-Euler approach, we will use in addition to the N_j DoF defining the internal configuration of the biped six DoF which allow to represent the stance foot (right foot) variables by the Eulerian variables corresponding to its linear and angular velocities: $\mathbf{v}_0, \boldsymbol{\omega}_0$. The foot's coordinates will be represented by the vectors \mathbf{x}_0 and $\boldsymbol{\alpha}_0$ which define respectively the position and orientation of the frame R_0 with respect to the reference frame R_S .

The biped's generalized coordinates are expressed by $\mathbf{X} = (\mathbf{x}_0; \boldsymbol{\alpha}_0; \mathbf{q}) \in \mathbb{R}^{(N_j+6)}$; the biped velocity is $\mathbf{V} = (\mathbf{v}_0; \boldsymbol{\omega}_0; \dot{\mathbf{q}}) \in \mathbb{R}^{(N_j+6)}$ and its acceleration is $\dot{\mathbf{V}} = (\dot{\mathbf{v}}_0; \dot{\boldsymbol{\omega}}_0; \ddot{\mathbf{q}}) \in \mathbb{R}^{(N_j+6)}$. The dynamic model in DS phase can be written in the classical form of Lagrange equations:

$$\mathbf{D}(\mathbf{X})\dot{\mathbf{V}} + \mathbf{C}(\mathbf{V}, \mathbf{q}) + \mathbf{G}(\mathbf{X}) + \mathbf{D}_J(\mathbf{q})\mathbf{R}_{14} = \mathbf{D}_\Gamma\boldsymbol{\Gamma} + \mathbf{D}_0\mathbf{R}_0 \quad (4.22)$$

where:

- $\mathbf{D} \in \mathbb{R}^{(N_j+6) \times (N_j+6)}$ is the symmetric definite positive inertia matrix;
- $\mathbf{C} \in \mathbb{R}^{(N_j+6)}$ is the vector representing Coriolis and centrifugal forces;
- $\mathbf{G} \in \mathbb{R}^{(N_j+6)}$ is the vector of gravity;
- $\mathbf{D}_J^\top \in \mathbb{R}^{6 \times (N_j+6)}$ is the Jacobian matrix reflecting the effects of ground reaction on the landing foot (left foot);
- $\mathbf{D}_\Gamma = (\mathbf{0}_{6 \times N_j}; \mathbf{I}_{N_j \times N_j})$ is a matrix of dimension $(N_j + 6) \times N_j$ allowing to take into consideration the joint torques in the dynamic model. Only the joints $q_1 \dots q_{N_j}$ are actuated;
- $\mathbf{D}_0 = (\mathbf{I}_{6 \times 6}; \mathbf{0}_{N_j \times 6})$ is a matrix of dimension $(N_j + 6) \times 6$ allowing to take into account the effects of ground reaction on the stance foot (right foot);

- $\mathbf{R}_0 = [{}^0\mathbf{f}_0, {}^0\mathbf{m}_0]^\top$ is the wrench of ground reaction forces on the stance foot expressed by forces and moments applied to the origin of the frame R_0 and expressed in R_s ;
- $\mathbf{R}_{14} = [{}^{13}\mathbf{f}_{14}, {}^{13}\mathbf{m}_{14}]^\top$ is the wrench of forces exerted by the swing foot on the ground;

4.4.2.2 Impulsive impact model

From the dynamic model (4.22), the impulsive impact model can be obtained by integrating it during the impact duration which tends to zero. The integration of the vectors \mathbf{C} , \mathbf{G} , and $\mathbf{\Gamma}$ which have finite values, give a zero result. Then these vectors have no influence on the impact model. Therefore, the impact model is:

$$\mathbf{D}(\mathbf{X}(T))\Delta\mathbf{V} = \mathbf{D}_0\mathbf{I}_0 - \mathbf{D}_J\mathbf{I}_{14} \quad (4.23)$$

where:

- \mathbf{I}_0 and \mathbf{I}_{14} are the intensity of Dirac delta functions for the forces \mathbf{R}_0 and \mathbf{R}_{14} ;
- $\Delta\mathbf{V} = (\mathbf{V}^+ - \mathbf{V}^-)$ is the variation of velocity at the impact;
- $\mathbf{V}^+ = (\mathbf{v}_0^+; \boldsymbol{\omega}_0^+; \dot{\mathbf{q}}^+)$ is the velocity of the biped after the impact;
- $\mathbf{V}^- = (\mathbf{v}_0^-; \boldsymbol{\omega}_0^-; \dot{\mathbf{q}}^-)$ is the velocity of the biped before the impact;
- $\mathbf{X}(T)$ is the biped's configuration at the impact;

This impact model will be used in a context of optimal movements definition, then some assumptions have to be made in accordance with the desired biped motion in order to include them in the constraints related to impulsive forces resulting from the impact model. Thus, we impose that the foot which swings to touch the ground, remains in contact with the ground without taking off, sliding and without any rotation.

The flat foot contact with the ground is supposed to be inelastic. Then, the velocity of the landing foot touching the ground is zero after impact. After the impact, either the previous stance foot (right foot) takes off the ground or both feet remain on the ground. In the first case, the velocity of the taking-off foot must be directed upwards just after the impact and its impulsive ground reaction forces are equal to zeros $\mathbf{I}_0 = \mathbf{0}_{6 \times 1}$. In the second case, the right foot velocity must be zero just after the impact. This implies that impulsive ground forces are produced in both feet and the impulsive ground reactions have vertical components directed upwards. Since we are interested in walking movements which are composed of simple SS phases only, the first case is considered and the previous stance foot is allowed to take off.

The equation (4.23) has $(N_j + 6)$ equations with $(N_j + 12)$ unknown variables. Additional equations based on assumptions on the biped's behavior at the impact are needed. Previous studies with planar robots [190] have shown that it is not possible to obtain movements after impact (with variation of joint velocities) without observing a take-off of the previous support foot. This corresponds to a zero velocity of the landing foot. An impacting foot with zero velocity at impact, is a valid solution for our bipedal gait model. There is no impact and the velocity of the two feet after impact is null. Then we have:

$$\mathbf{D}_J^\top \mathbf{V}^+ = \mathbf{0}_{6 \times 1} \quad (4.24)$$

Equations (4.23) and (4.24) give the impact model:

$$\begin{bmatrix} \mathbf{D}(\mathbf{X}(T)) & \mathbf{D}_J \\ \mathbf{D}_J^\top & \mathbf{0}_{6 \times 6} \end{bmatrix} \begin{bmatrix} \mathbf{V}^+ \\ \mathbf{I}_{14} \end{bmatrix} = \begin{bmatrix} \mathbf{D}(\mathbf{X}(T))\mathbf{V}^- \\ \mathbf{0}_{6 \times 1} \end{bmatrix} \quad (4.25)$$

Since \mathbf{D} is a definite positive matrix and \mathbf{D}_J has full rank, the impulse forces \mathbf{I}_{14} and the biped's velocity vector just after the impact \mathbf{V}^+ are determined by:

$$\begin{bmatrix} \mathbf{V}^+ \\ \mathbf{I}_{14} \end{bmatrix} = \begin{bmatrix} \Delta_v \\ \Delta_{I_{14}} \end{bmatrix} \mathbf{V}^- \quad (4.26)$$

where:

$$\Delta_{I_{14}} = (\mathbf{D}_J^\top \mathbf{D}^{-1} \mathbf{D}_J)^{-1} \mathbf{D}_J^\top \quad (4.27)$$

and:

$$\Delta_v = -\mathbf{D}^{-1} \mathbf{D}_J \Delta_{I_{14}} + \mathbf{I}_{N_j+6} \quad (4.28)$$

4.4.2.3 Calculation of the matrices \mathbf{D} and \mathbf{D}_J

The calculation of the elements of matrices \mathbf{D} and \mathbf{D}_J is carried out by the Newton-Euler algorithm modified by Walker and Orin [191] for the calculation of the direct dynamic model. This method is based on the formulation provided by the Lagrangian approach on the dynamic model to reconstruct the elements of the matrices column by column.

For given articular positions \mathbf{q} , stance foot coordinates $(\mathbf{x}_0; \alpha_0)$, biped's velocities \mathbf{V} and accelerations $(\dot{\mathbf{v}}_0; \dot{\omega}_0; \ddot{\mathbf{q}})$, and for given contact forces \mathbf{R}_{14} , it is possible to calculate the joint torques and forces and moments $(\mathbf{F}^r, \mathbf{M}^r)$ of ground reaction on the right foot using the double recursive calculations of Newton-Euler algorithm. We observe that the matrices \mathbf{D}_Γ and \mathbf{D}_0 on the right-hand side of the dynamic model (4.22) have a particularly simple

expression, allowing us to obtain \mathbf{F}^r , \mathbf{M}^r and $\mathbf{\Gamma}$ on the left-hand side of the direct dynamic model equation:

$$\begin{bmatrix} \mathbf{F}^r \\ \mathbf{M}^r \\ \mathbf{\Gamma} \end{bmatrix} = \mathbf{D}(\mathbf{X}) \begin{bmatrix} \dot{\mathbf{v}}_0 \\ \dot{\boldsymbol{\omega}}_0 \\ \ddot{\mathbf{q}} \end{bmatrix} + \mathbf{C}(\mathbf{V}, \mathbf{q}) + \mathbf{G}(\mathbf{X}) + \mathbf{D}_J(\mathbf{q})\mathbf{R}_{14} \quad (4.29)$$

For the following choice of desired velocities, accelerations, contact forces on the left foot, and particular gravity acceleration:

$$(\dot{\mathbf{v}}_0; \dot{\boldsymbol{\omega}}_0; \ddot{\mathbf{q}}) = \mathbf{e}_i, \quad \dot{\mathbf{q}} = \mathbf{0}_{N_j \times 1}, \quad g = 0, \quad \mathbf{R}_{14} = \mathbf{0}_{6 \times 1} \quad (4.30)$$

where \mathbf{e}_i is a unit vector of dimension $(N_j + 6) \times 1$ which the i^{th} element is equal to 1, and the other are equal to 0, the vector $(\mathbf{F}^r; \mathbf{M}^r; \mathbf{\Gamma})$ is equal to the i^{th} column of $\mathbf{D}(\mathbf{X})$. By assigning all the successive values of \mathbf{e}_i for $i = 1$ to $N_j + 6$ to the vector $\dot{\mathbf{V}}$, the matrix $\mathbf{D}(\mathbf{X})$ can then be determined column by column.

The Jacobian matrix $\mathbf{D}_J(\mathbf{q})$ can also be obtained by applying the same method with:

$$(\dot{\mathbf{v}}_0; \dot{\boldsymbol{\omega}}_0; \ddot{\mathbf{q}}) = \mathbf{0}_{(N_j+6) \times 1}, \quad \dot{\mathbf{q}} = \mathbf{0}_{N_j \times 1}, \quad g = 0, \quad \mathbf{R}_{14} = \mathbf{e}_i \quad (4.31)$$

where \mathbf{e}_i is a vector of dimension 6×1 .

4.4.2.4 Determination of final velocity parameters

Taking into account the symmetry of biped's structure, introduced in section 4.3.2, and according to which the final configuration of the right part of the biped is equal to the initial configuration of the left one, the joint velocities after the impact between two successive steps labeled $i-1$ and i can be determined in function of joint velocities just before the impact. From the expression (4.26) we have:

$$\mathbf{V}^+ = \Delta_v \begin{bmatrix} \mathbf{v}_0 \\ \boldsymbol{\omega}_0 \\ \dot{\mathbf{q}}_{i-1}(T_{i-1}) \end{bmatrix}^- \quad (4.32)$$

Considering the equation (4.32) and the switching matrix \mathbf{E} , which describes left and right joints permutation, the initial velocity vector $\dot{\mathbf{q}}_i(t_0 = 0) = (\dot{q}_{i,1}^0, \dots, \dot{q}_{i,N_j}^0)^\top$ can be calculated by:

$$\dot{\mathbf{q}}_i(t_0) = \mathbf{E}\mathbf{R}\mathbf{V}^+ \quad (4.33)$$

where $\mathbf{R} = (\mathbf{0}_{6 \times (N_j+6)}; \mathbf{I}_{N_j \times (N_j+6)})$ is a matrix of dimension $(N_j+6) \times (N_j+6)$ allowing to take into account only the joint velocity variables, since the final velocity vector $\dot{\mathbf{q}}_{i-1}^f = \dot{\mathbf{q}}_{i-1}(T_{i-1}) = (\dot{q}_{i-1,1}^f, \dots, \dot{q}_{i-1,N_j}^f)^\top$ is defined as a vector of parameters of dimension $N_j \times 1$.

4.5 Description of joint motion

A model of a locomotor system, to generate walking gait patterns specific to human locomotion, was introduced in section 4.2.2. Such a model, represented by equations of motion and various constraints related to the dynamics of motion, will directly lead to a problem of dynamic optimization under constraints. Indeed, such an optimization problem consists in extracting from the dynamics equations a solution minimizing a performance criterion based on a set of decision variables. The solution consists, therefore, in generating configurations at different instants of gait cycle, by a finite number of independent variables, for the generation of optimal gaits including cyclic steps or strides.

Optimal gaits, thus generated by a finite number of parameters, require the formulation of a finite dimension problem. The problem of walking gait modeling in steady state is studied. Conversion to a finite dimension problem consists of representing the decision variables by a finite number of discrete parameters. This implies expressing the criterion to be minimized as a function of parameters expressing the configuration variables by interpolation functions.

Interpolation functions are most often spline functions, polynomial functions, trigonometric functions, Fourier series decompositions, or piecewise-defined functions. C^2 -class spline functions were chosen so that we have continuous second derivative functions for accelerations in joint space. This choice also facilitates joints rates and accelerations calculation and has the benefit of saving computational effort.

For a step of duration T_1 , we consider N intermediate configurations in single support. Then, there is $(N+1)$ time intervals between each two consecutive double support configurations. Intermediate configurations are uniformly spaced in time, then each interval duration is equal to $h = \frac{T_1}{(N+1)}$.

A trajectory generation problem is solved on the global time interval denoted by $\Omega = \{t_0, t_{N+1}\}$. On this global interval, a sequence of monotonically increasing time values are called knots and the number of values in the sequence is equal to $N+2$. The set of time knots is $\{t_0, t_1, t_2, \dots, t_N, t_{N+1}\}$ with $t_0 = 0$ and $t_{N+1} = T_1$. These knots define the discrete set of

segments that constitute the global time interval as follows:

$$\Omega = \bigcup_{k=0}^N \Omega_k \quad \text{where } \{\Omega_k = t \mid t_k \leq t < t_{k+1}\} \quad (4.34)$$

In order to approximate a model DoF q_j , a spline function $\phi_j(t)$ is defined on Ω and obtained by the concatenation of $N+1$ polynomial functions successively defined on the intervals Ω_k , and connected two by two at time knots t_k :

$$\phi_j(t) = \begin{cases} \varphi_{j,0}(t) & \text{if } t \in \Omega_0 \\ \varphi_{j,1}(t) & \text{if } t \in \Omega_1 \\ \vdots & \\ \varphi_{j,N}(t) & \text{if } t \in \Omega_N \end{cases} \quad (4.35)$$

where $\varphi_{j,0}(t), \dots, \varphi_{j,N}(t)$ are 3rd order polynomials such that:

$$\varphi_{j,k}(t) = \sum_{l=0}^3 a_{j,k}^l (t - t_k)^l, \quad k = 0, \dots, N \quad \forall t \in \Omega_k \quad (4.36)$$

where $a_{j,k}^l$ are the coefficients expressed as a function of the values at the time knots to be interpolated.

Considering that for each function $\phi_j(t)$ there are $N+1$ polynomials with 4 coefficients, $4(N+1)$ independent conditions are necessary to define each function $\phi_j(t)$. These conditions are then listed:

1. The spline function must provide all the configuration values corresponding to the time knots. This includes position continuity conditions at intermediate time knots:

$$\begin{cases} \varphi_{j,k}(t_k) = a_{j,k}^0 = q_{j,k} \\ \varphi_{j,k}(t_{k+1}) = a_{j,k}^0 + a_{j,k}^1 h + a_{j,k}^2 h^2 + a_{j,k}^3 h^3 = q_{j,k+1} \end{cases}, \quad k = 0, \dots, N \quad (4.37)$$

where $q_{j,k}$ is the configuration at the knot t_k .

2. Connections between successive polynomials must ensure continuity of velocity and acceleration at the intermediate knots in single support:

$$\begin{cases} \dot{\varphi}_{j,k}(t_{k+1}) = \dot{\varphi}_{j,k+1}(t_{k+1}) \Rightarrow a_{j,k}^1 + 2ha_{j,k}^2 + 3h^2 a_{j,k}^3 = a_{j,k+1}^1 \\ \ddot{\varphi}_{j,k}(t_{k+1}) = \ddot{\varphi}_{j,k+1}(t_{k+1}) \Rightarrow a_{j,k}^2 + 3ha_{j,k}^3 = a_{j,k+1}^2 \end{cases}, \quad k = 0, \dots, N-1 \quad (4.38)$$

3. The limit conditions, velocities at the initial instant, $\dot{q}_{j,0}$, and at the final instant, $\dot{q}_{j,N+1}$, are imposed in such a way that:

$$\begin{cases} \dot{\phi}_{j,0}(t_0) = a_{j,0}^1 = \dot{q}_{j,0} \\ \dot{\phi}_{j,N}(t_{N+1}) = a_{j,N}^1 + 2ha_{j,N}^2 + 3h^2a_{j,N}^3 = \dot{q}_{j,N+1} \end{cases} \quad (4.39)$$

For each function $\phi_j(t)$, the conditions from (4.37) to (4.39) represent $4(N+1)$ equations: $2(N+1)$ equations for (4.37), $2N$ equations for (4.38) and two equations for the limit conditions (4.39). Then, these conditions constitute a system of equations that can be rewritten in matrix form as:

$$\mathbf{A}_i \begin{bmatrix} a_{j,0}^0 \\ a_{j,0}^1 \\ a_{j,0}^2 \\ a_{j,0}^3 \\ a_{j,1}^0 \\ \vdots \\ a_{j,N-1}^3 \\ a_{j,N}^0 \\ a_{j,N}^1 \\ a_{j,N}^2 \\ a_{j,N}^3 \end{bmatrix} = \mathbf{b}_j = \begin{bmatrix} q_{j,0} \\ q_{j,1} \\ \vdots \\ q_{j,N} \\ q_{j,1} \\ q_{j,2} \\ \vdots \\ q_{j,N+1} \\ \mathbf{0}_{2N \times 1} \\ \dot{q}_{j,0} \\ \dot{q}_{j,N+1} \end{bmatrix} \quad (4.40)$$

Where \mathbf{A}_i is a $(4N+4) \times (4N+4)$ matrix function of the duration h and deduced from the previous conditions. This results in a linear system of dimension $4N+4$. The unique solution, \mathbf{C}_j , of the system to be solved can then be determined:

$$\mathbf{C}_j = \mathbf{A}_i^{-1} \mathbf{b}_j \quad (4.41)$$

The configuration variables $q_j(t)$ for any $t \in \Omega$ can then be rewritten as a function of the $4N+4$ coefficients \mathbf{C}_j and time:

$$q_j(t) = \phi_j(\mathbf{C}_j, t), \quad t \in [t_0, t_{N+1}] \quad (4.42)$$

The vector of biped's configuration $\mathbf{q}(t)$ is then defined by the function Φ as:

$$\mathbf{q}(t) = \Phi(\mathbf{C}, t) \quad (4.43)$$

where

$$\Phi(\mathbf{C}, t) = [\phi_1(\mathbf{C}_1, t), \dots, \phi_{N_j}(\mathbf{C}_{N_j}, t)]^\top \quad (4.44)$$

The matrix \mathbf{C} of dimension $(4N+4) \times N_j$ gathers the vectors \mathbf{C}_j of the polynomial coefficients. For a given joint and a given step, these coefficients are defined according to:

- Initial and final double support configurations: two parameters;
- Initial and final velocities: two parameters;
- Intermediate positions in single support: N parameters.

We therefore need $19 \times (N+4)$ interpolation parameters for step-level optimization.

4.6 Choice of optimization variables

For a step, the number of variables defining the motion can be significantly reduced with respect to the number of required parameters for interpolation due to:

- Cyclicity condition expressed by the switching matrix i.e. final joint positions can be deduced from initial joint position of the next step $i+1$: 19 variables less;
- The dependence of initial joint velocities on final joint positions and velocities of the previous step $i-1$, as illustrated by the impact model: 19 variables less;
- The hypothesis that the axial rotation between the trunk and the pelvis is defined at initial double support as function of the rotation of the distal segment connecting the hip centers about the vertical axis ($\mathbf{q}_{13}^0 = -p_5$): one variable less;
- The choice of a minimal number of variables to parameterize the legs closed loop configuration at initial double support (seven parameters instead of 12 parameters; see figure 4.16): five variables less;

Then, thanks to modeling assumptions, the optimized vector is reduced by 44 variables for optimization over step. This allows to make the convergence of the optimization process towards a local minimum less complex and more efficient.

4.6.1 Optimization variables for step-level optimization

For N intermediate configurations, the following variables are optimized during the process of step-level optimization:

- $\mathbf{q}(t_i)$, $i=1, \dots, N$: Intermediate configurations of the biped in SS phase ($N \times 19$ parameters);

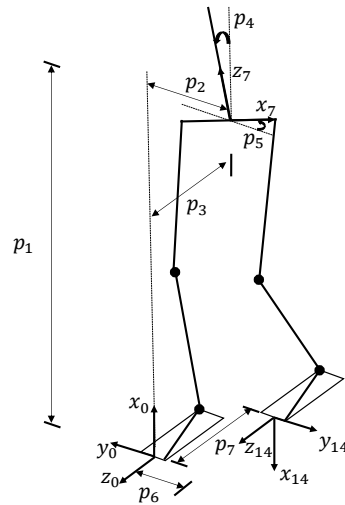


Fig. 4.16 The seven variables determining the locomotor system configuration at initial DS: five variables for pelvis situation with respect to the stance foot, and two parameters for step length and width.

- $\dot{\mathbf{q}}(T_1)$: Final joint velocities of the biped just before the impact (19 parameters);
- (p_1, p_2, p_3) : The hips center coordinates in initial DS (three parameters);
- (p_4, p_5) : The pelvis orientations in the sagittal and transverse planes for the initial double support, respectively (two parameter);
- (p_6, p_7) : The width and length of the step, respectively (two parameters);
- $\mathbf{q}_{arm}(t = 0)$: The initial arms configuration in DS (6 parameters);

Thus, for a cyclic walking gait over a step, we have $19N+32$ optimization variables that are the subjects of a cost functional minimization.

4.6.2 Determination of limit configuration parameters

In initial double support configurations, the biped has both feet in flat contact with the ground (figure 4.16). The parameters of these configurations are dependent. Then, it is more suitable to define such configurations in function of Cartesian coordinates instead of joint coordinates, since it allows to have less parameters considering the following assumptions in DS:

- The swing foot (left foot) has vertical coordinate equal to zero since it is on the ground;
- The swing foot has the same orientation as the stance foot (right foot) since we consider a straight forward walking pattern;

- There is no roll rotation of the pelvis segment at double support phase. There are only rotation angles in the sagittal and transverse planes.

Both legs configurations are defined by 12 articular positions q_1, \dots, q_{12} . The configuration vector at the instant $t_0 = 0$ is $\mathbf{q}^0 = \mathbf{q}(t_0) = (q_1^0, \dots, q_{12}^0)^\top$, and we aim to find a minimal set of parameters \mathbf{P}_{IGM} that allows to define a desired situation of the locomotor system. This formulated problem leads to solve the inverse geometric model (IGM) for each leg of the biped. To define the specific configuration \mathbf{q}^0 , two desired situations are defined:

- a desired situation that defines the position and orientation of the pelvis, defined by the situation of the frame R_7 ($O_7, \mathbf{x}_7, \mathbf{y}_7, \mathbf{z}_7$) with respect to the frame R_0 ($O_0, \mathbf{x}_0, \mathbf{y}_0, \mathbf{z}_0$) linked to the right foot;
- a desired situation that defines the position and orientation of the left foot, whose associated frame is defined as R_{14} ($O_{14}, \mathbf{x}_{14}, \mathbf{y}_{14}, \mathbf{z}_{14}$).

Taking into account the assumptions in double support, those situations can be parametrized with only seven variables:

- $(p_1, p_2, p_3, p_4, p_5)$: parameters defining the position and orientation of the frame linked to the pelvis (R_7) with respect to the reference frame R_0 , at the initial double support.
- (w, d_1) : The width and length of the step, respectively.

The number of parameters in this minimal set allows to reduce the number of optimization variables. Using the first four parameters, the following transformation matrix is calculated:

$${}^0\mathbf{T}_7 = \begin{bmatrix} & {}^0\mathbf{R}_7 & {}^0\mathbf{P}_7 \\ 0 & 0 & 0 & 1 \end{bmatrix} = \begin{bmatrix} 0 & \sin(p_4) & \cos(p_4) & p_1 \\ -\cos(p_5) & \cos(p_4)\sin(p_5) & -\sin(p_4)\sin(p_5) & p_2 \\ -\sin(p_5) & -\cos(p_4)\cos(p_5) & \sin(p_4)\cos(p_5) & p_3 \\ 0 & 0 & 0 & 1 \end{bmatrix} \quad (4.45)$$

where ${}^0\mathbf{P}_7 = (x_7 = p_{1,j}, y_7 = p_{2,j}, z_7 = p_{3,j})^\top$ is the vector of cartesian position and ${}^0\mathbf{R}_7 = \mathbf{rot}(y, \theta_7 = \frac{\pi}{2}) \cdot \mathbf{rot}(z, \phi_7 = -p_4) \cdot \mathbf{rot}(x, \psi_7 = p_5 - \frac{\pi}{2})$ is the the rotation matrix defining the situation of R_7 with respect to R_0 . ϕ_7 , θ_7 and ψ_7 are respectively the roll, pitch and yaw angles. Similarly, the position and orientation of the left foot, R_{14} , in the reference R_0 is defined as:

$${}^0\mathbf{T}_{14} = \begin{bmatrix} & {}^0\mathbf{R}_{14} & {}^0\mathbf{P}_{14} \\ 0 & 0 & 0 & 1 \end{bmatrix} = \begin{bmatrix} -1 & 0 & 0 & 0 \\ 0 & -1 & 0 & -w \\ 0 & 0 & 1 & -d_1 \\ 0 & 0 & 0 & 1 \end{bmatrix} \quad (4.46)$$

where ${}^0\mathbf{T}_{14}$ are the transformation matrix defining the frame R_{14} with respect to the frame R_0 . Assuming that at the instant t_0 the left foot is on the floor and oriented in a straight walking direction, the position vector is ${}^0\mathbf{P}_{14} = (x_{14} = 0, y_{14} = -w, z_{14} = -d_1)^\top$ and the orientation matrix is given by ${}^0\mathbf{R}_{14} = \mathbf{rot}(y, \theta_{14} = -\pi) \cdot \mathbf{rot}(z, \phi_{14} = 0) \cdot \mathbf{rot}(x, \psi_{14} = -\pi)$. In order to use the same IGM for both legs, a new frame R_f linked to the left foot is defined, it has the same origin $O_f = O_{14}$ of R_{14} . This frame has the same orientation with respect to the left foot as that of the frame R_0 with respect to the right foot. This implies that the unit vector \mathbf{y}_f must be directed towards the outside of the left foot i.e. $\mathbf{y}_f = -\mathbf{y}_0$. Then, the transformation matrix between the frame R_{14} and the added frame R_f , ${}^f\mathbf{T}_{14}$ is:

$${}^f\mathbf{T}_{14} = \begin{bmatrix} {}^f\mathbf{R}_{14} & \mathbf{0}_{3 \times 1} \\ 0 & 0 & 0 & 1 \end{bmatrix} \quad (4.47)$$

where ${}^f\mathbf{R}_{14} = {}^f\mathbf{R}_0 {}^0\mathbf{R}_{14}$, and ${}^f\mathbf{R}_0 = \begin{bmatrix} 1 & 0 & 0 \\ 0 & -1 & 0 \\ 0 & 0 & 1 \end{bmatrix}$.

Using these transformation matrices, the situation of the pelvis with respect to the left foot on the ground is given by:

$${}^f\mathbf{T}_7 = {}^f\mathbf{T}_{14} \cdot {}^0\mathbf{T}_{14}^{-1} \cdot {}^0\mathbf{T}_7 \quad (4.48)$$

The configuration vector $\mathbf{q}(t_0)$ is then obtained by the solution of the MGI:

$$\mathbf{q}_{1:6}^0 = \text{IGM}_R(p_1, p_2, p_3, p_4, p_5) \quad (4.49)$$

and:

$$\mathbf{q}_{7:12}^0 = \text{IGM}_L(w, d_1) \quad (4.50)$$

where the expression (4.49) represents the solution for the right leg satisfying the matrix (4.45) while (4.50) gives the solution for the left leg according to the matrix (4.48). The equation (4.50) has a finite number of solutions because it is implicitly imposed that $x_{14} = 0$, $\phi_{14} = 0$, $\theta_{14} = -\pi$, $\psi_{14} = -\pi$. The solution (4.50) for the left leg depends indirectly on the conditions imposed by the matrix (4.45). Each matrix of (4.45) and (4.48) implies six equations, three for rotations and three for positions, and is related to six unknown articular variables, $\mathbf{q}_{1:6}^0$ and $\mathbf{q}_{7:12}^0$ respectively. Then, a unique vector of initial configuration is obtained:

$$\mathbf{q}^0 = (\mathbf{q}_{1:6}^0, \mathbf{q}_{7:12}^0)^\top \quad (4.51)$$

for a minimal set of seven parameters, grouped in the vector:

$$\mathbf{P}_{\text{IGM}} = (p_1, p_2, p_3, p_4, p_5, w, d_1)^\top \quad (4.52)$$

Taking into account the symmetry of the locomotor system's kinematic chain, from one leg to the other, the inverse problem for the left leg can be expressed in function of the IGM for the stance leg:

$$\text{IGM}_L = \mathbf{E}_l \cdot \text{IGM}_R \quad (4.53)$$

where \mathbf{E}_l is the anti-diagonal matrix of dimension 6×6 defined in equation (4.6).

4.7 Definition of constraints and cost functions

Infinite number of sets of variables values result in a gait cycle satisfying the nonlinear constraints that will be listed in paragraph 4.7.1. A constrained optimization algorithm is used to find an optimal solution minimizing the cost function. The problem can be written as:

$$\begin{cases} \text{Minimize } C_f(\mathbf{P}) \\ \text{Subject to } g_k(\mathbf{P}) < 0, \quad k = 1, 2, \dots, l_g \end{cases} \quad (4.54)$$

where $C_f(\mathbf{P})$ is the cost functional to minimize, $g_k(\mathbf{P})$ are the nonlinear inequality constraints, and l_g is the number of constraints. MATLAB function "fmincon" [192] from optimization toolbox is used to solve this problem. Active set algorithm is used, which is based on SQP method [193] suitable for highly nonlinear constrained problems.

4.7.1 Constraints

Many constraints have to be imposed to have a human-like gait cycle and possible trajectories:

a) Biomechanical constraints:

- Each actuator has its bounds such that:

$$|\Gamma_j| - \Gamma_{j,max} < 0, \quad \text{for } j \in \text{ind}_j \quad (4.55)$$

where $\Gamma_{j,max}$ is the maximum torque for each actuator.

- Joint rates must not exceed their limits:

$$|q_j| - q_{j,max} < 0, \quad \text{for } j \in \text{ind}_j \quad (4.56)$$

where $q_{j,max}$ stands for the maximum rate for each joint.

- Lower and upper bounds are imposed for different joints during GC:

$$q_{j,min} < q_j < q_{j,max}, \text{ for } j \in ind_j \quad (4.57)$$

where $q_{j,min}$ and $q_{j,max}$ denote the minimum and maximum joint position limits, respectively.

b) Stability constraints:

- Constraints on the ground reaction ${}^0\mathbf{f}_0 = [{}^0f_{0x}, {}^0f_{0y}, {}^0f_{0z}]^\top$ for the support foot in single support phases and the impulsive forces $\mathbf{I}_{14} = [I_{14x}, I_{14y}, I_{14z}]$ of the landing foot at impacts must be considered. Ground reaction for single support configurations and the impact forces in instantaneous double support must be inside a friction cone of a coefficient μ :

$$\sqrt{{}^0f_{0y}^2 + {}^0f_{0z}^2} < \mu {}^0f_{0x} \quad (4.58)$$

$$\sqrt{I_{14y}^2 + I_{14z}^2} < \mu I_{14x} \quad (4.59)$$

- No take-off constraint must be taken into consideration so ground reaction forces during single support and impact forces at the double support must be directed upward:

$${}^0f_{0x} > 0 \quad (4.60)$$

$$I_{14x} > 0 \quad (4.61)$$

- To satisfy unilateral contact between the support foot and the ground, the ZMP needs to be constrained inside the BOS. The BOS in single support is the polygon defined by the four corners of the support foot. Since feet are modeled by rectangles of l_p width and L_p length, the ZMP must satisfy:

$$\frac{-l_p}{2} < y_{ZMP} < \frac{l_p}{2} \quad (4.62)$$

$$-L_p < z_{ZMP} < 0 \quad (4.63)$$

The condition of ZMP must be verified during single support phases and impacts.

- In order to generate contralateral swing of the arms, the Zero Yawing Moment (ZYM) constraint [14] keeps the resultant yawing component (in the vertical (x) direction) of IGF moment about the ZMP under a small upper bound of magnitude ($=0.1$ N.m in this study).

The IGF moment about the ZMP is given by:

$$\mathbf{Y}^{IGF} = \sum_{i=1}^{n_s} (\mathbf{x}_{\text{COM}}^i - \mathbf{x}_{\text{ZMP}}) \times m_i (\mathbf{g} - \ddot{\mathbf{x}}_{\text{COM}}^i) \quad (4.64)$$

where \mathbf{x}_{ZMP} is the ZMP position, $\mathbf{x}_{\text{COM}}^i$ and $\ddot{\mathbf{x}}_{\text{COM}}^i$ are the i^{th} segment's COM position and acceleration, respectively, \mathbf{g} is the gravity vector, m_i is the i^{th} segment's mass, n_s is the number of body segments.

c) Geometric constraint at double support configurations:

- The distance between the stance ankle joint center and its ipsilateral hip center must remain under a maximum limit l_{max} to avoid singularities at the knee level, and above a minimum value of l_{min} to avoid crouch gait, i.e. non human-like gait that is energetically not efficient, and that may typically be avoided by the minimization of the sthenic criterion:

$$l_{min} < d(O_1, O_4) < l_{max} \quad (4.65)$$

where $l_{min} = 0.92(L_3 + L_4)$, $l_{max} = 0.99(L_3 + L_4)$, L_3 and L_4 are respectively shank and thigh lengths as shown in figure 4.12.

d) Geometric constraints in single support configurations:

- Constraints on the positions of the four corners of the swing foot are imposed in order to avoid collision between the swing leg and the stance leg or the ground.
- A constraint to avoid collision issue of the upper extremities against the torso is added.

4.7.2 Cost function

It has been proved that normal arm swinging may need some muscular effort but it decreases the overall metabolic expenditure of human walking [8]. Then, we aim at minimizing the joint actuators energy dissipated over a step of duration T_1 to travel the distance d_1 . we consider a cost functional $C_{\Gamma,1}$ that is the integral of the norm of joint torques, approximated

by a finite sum of torques function values at the chosen time samples [84]:

$$C_{\Gamma,1} = \frac{1}{d_1} \int_0^{T_1} \mathbf{\Gamma}_1(t)^\top \mathbf{\Gamma}_1(t) dt \quad (4.66)$$

where $\mathbf{\Gamma}_1$ is the $N_j \times 1$ vector of joint torques during the step.

Additionally, a potential cost functional involves the deviation of the trunk segment from upright position [14] which is amounted to the following function:

$$C_{UTP,1} = \int_0^{T_1} (\mathbf{p}_7(t) - \mathbf{p}_h(t)) \cdot \mathbf{g} dt \quad (4.67)$$

where \mathbf{p}_h is the cartesian coordinates of the hips middle point, \mathbf{p}_7 is the cartesian coordinates of the 7th Cervicale corresponding in our biped model to the origin O_{16} , $\mathbf{g} = (-9.81, 0, 0)^\top$ is the gravity vector and the operator \cdot denotes the scalar product.

Consequently, the cost functional for a step is given by:

$$C_f = C_{\Gamma,1} + \rho \cdot C_{UTP,1} \quad (4.68)$$

where $\rho > 0$ is a penalty factor.

4.8 Validation with experimental data

4.8.1 Numerical examples of simulation outputs

As shown in figure 4.17, we consider $N = 2$ intermediate knots and then we have four time knots for joint trajectory interpolation. For each step i of duration T_i , each joint profile is approximated at five uniformly spaced instants in each time interval. Since we have $(N + 1)$ time intervals, $n_s = 5(N + 1) + 1 = 16$ time samples: $t_k = kT_{s,i}$, $k = 0, \dots, n_s-1$, are considered for each step where $T_{s,i} = \frac{T_i}{n_s-1}$ is the sampling period. At each of these instants, the vector of constraints is calculated in order to check if they are satisfied during the global time interval. In simulation tests, we define the following matrices which are the results of trajectory interpolation corresponding to each step labeled i , $i=1,2$:

- \mathbf{Q}_i : The 19×16 matrix containing the vectors of biped's configuration corresponding to time samples;
- $\dot{\mathbf{Q}}_i$: The 19×16 matrix containing the vectors of joints rates corresponding to time samples;

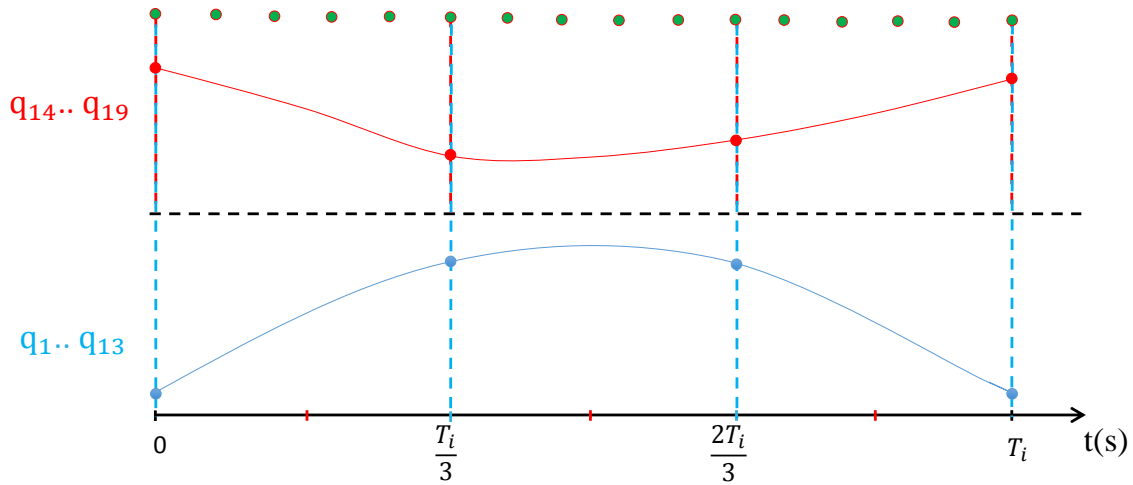


Fig. 4.17 Example of interpolation of joint positions for $N = 2$ intermediate time knots. The red/blue dots represent the values from which trajectories are interpolated. The green dots represent the instants where the constraints are evaluated.

- $\ddot{\mathbf{Q}}_i$: The 19×16 matrix containing the vectors of joints accelerations corresponding to time samples;

Note that all matrices for both right ($i=1$) and left ($i=2$) steps, are expressed in the same model of a right step, where the right foot is the stance foot and the frame R_0 is linked to it. Then, the switching matrix must be used to relabel the different joints. For instance, the 3rd line of \mathbf{Q}_2 corresponds to the inverse of the left knee rotation, and the 19th line of \mathbf{Q}_2 corresponds to the right elbow rotation, during the left step.

In order to check continuity and cyclicity conditions, right and left shoulders pitch angles and rates profiles are plotted (see figures 4.18 and 4.19) for our specific case: the optimized variables that correspond to the first step are equal to those corresponding to the left step, with symmetry indexes equal to 0.5. These profiles are presented on three successive steps in order to check continuity conditions at the two impact instants corresponding to $t = T_1$ and $t = T = 2T_1$.

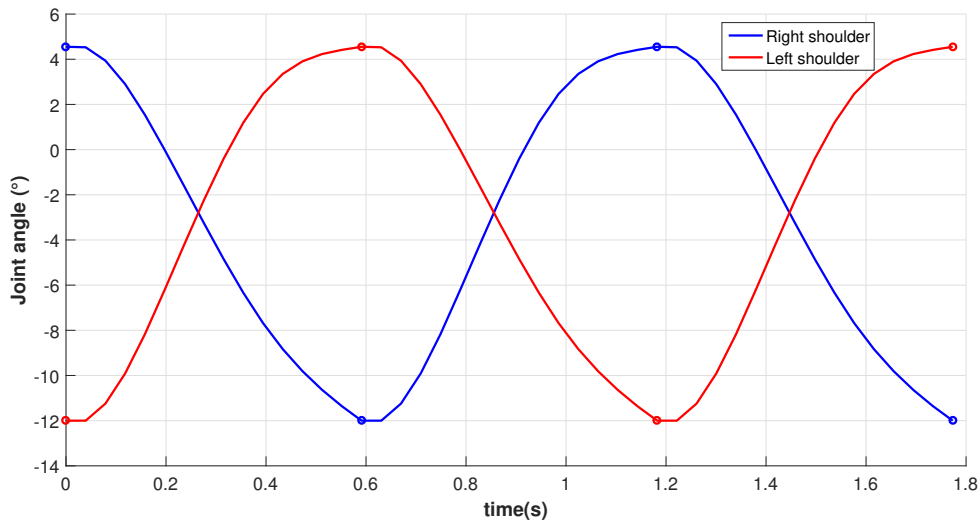


Fig. 4.18 Right and shoulder pitch angle histories during three consecutive steps following the sequence right-left-right. The dots correspond to the values at impacts instants.

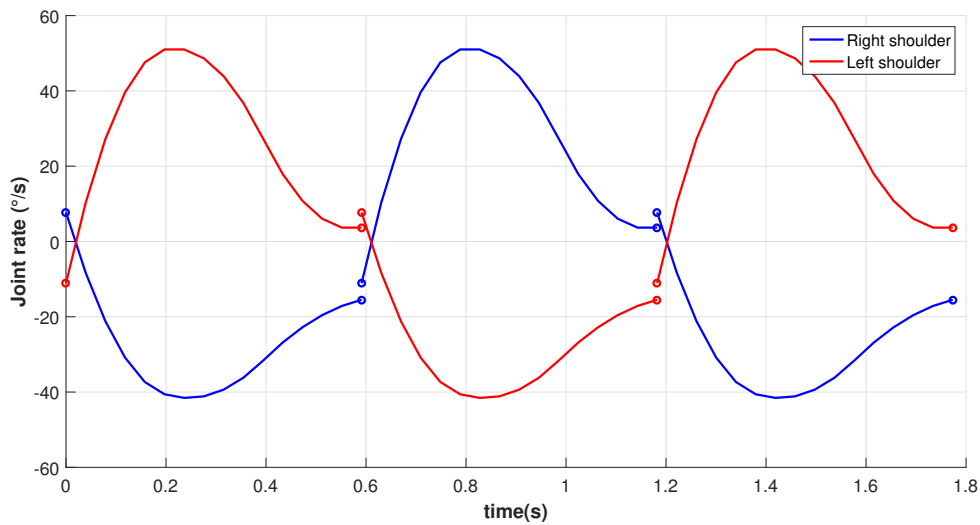


Fig. 4.19 Right and shoulder pitch joint velocities histories during three consecutive steps following the sequence right-left-right. The dots correspond to the values at impacts instants.

From these plots, it can be deduced that these conditions are verified:

- Joint position profiles are continuous during single support phases and at the instants of impacts;
- Joint velocity profiles are continuous during single support phases;

- There is a discontinuity of joints velocities at the impact instants. Consequently, joints accelerations are discontinuous at these instants;
- The joint position and velocity profiles of the right shoulder during the first step are equal to the profiles that correspond to the left shoulder during the second step, due to the exchange of role of arms after each impact, and to the fact that a cyclic gait over a step is considered.

4.8.2 Estimation of selected gait parameters

4.8.2.1 Assessment of natural aspects of walking

In this section, we consider stride profiles of salient variables related to natural aspects (unloaded swinging case, i.e. a symmetrical gait) of walking. Profiles are extracted from simulation and compared with kinematic data from motion capture experiments on the same test subject, which experimental setup will be presented in section 5.2.1.

4.8.2.1.1 Arm motion Appendix C provides right shoulder and elbow motion in the sagittal plane during gait cycle. The same patterns of arcs of motion are obtained for both simulation and experimental approaches. The shoulder reaches his maximum extension (20°) during initial double support phase and then flexes to a peak position in terminal double support. After holding this position, the shoulder extends through the next single support phase. In simulation, although the peak flexion remains the same, the total arc of motion increases with faster gait velocities with values close to experimental ones. A similar pattern is obtained for the elbow. Flexion arc occurs in ipsilateral foot stance phase and extension arc is performed during ipsilateral foot swing. Both experimental and simulation profiles show that the range of motion of the elbow increases for faster walking.

4.8.2.1.2 COM displacement The gait model reproduced the same displacement patterns in both lateral and vertical directions (appendix D). The COM is displaced following a double sinusoidal path in vertical direction and single sinusoidal path in lateral direction. The lateral displacement is increased for low speeds while vertical displacement is greater for faster velocities. In double support phases, neutral position in lateral direction and minimum vertical position of the COM are reached. Difference in lateral displacement magnitudes between both approaches is due to the difference between step width values since lateral displacement depends on walking base [53].

4.8.2.2 Step characteristics

Table 4.2 provides step characteristics values over the three overground walking velocities for both experiments (E) and simulation (S). In both approaches, step length showed an increasing trend as walking speed increased and higher step cadence is obtained for faster walking velocities (V_2 and V_3) compared to low velocity. For simulation, step length and width results were close to those found in experiments. However, an inverse trend is observed for optimal step width values.

Table 4.2 Step characteristics across three gait velocities for experimental and simulation data. (E): experimental data, (S): simulation data.

Gait speed	Step length (cm)		Step width (cm)		step cadence (s^{-1})	
	(E)	(S)	(E)	(S)	(E)	(S)
V_1	54.9	57.1	13.2	12.4	1.58	1.51
V_2	73.4	68.4	10.5	12.6	1.91	2.05
V_3	81.5	79.2	9.9	13.9	2.01	2.08

4.8.2.3 Acceleration features estimation

Preliminary results show a difference in magnitude between acceleration signals from experiments and simulation due to the simplifying assumptions considered in the model, then a qualitative evaluation of our simulation results is conducted. This evaluation includes comparison with experimental data based on normalized acceleration patterns, as well as variation tendencies of some acceleration items across walking velocities. Normalized signals are obtained by dividing each signal by its maximum value throughout the gait cycle.

4.8.2.3.1 Acceleration profiles Figures 4.20, 4.21 and 4.22 present normalized acceleration profiles related to different body parts, for both experimental and simulation approaches. Experimental profiles correspond to the speed/carrying mode combination $V_2/(S1)$, while simulation data correspond to the walking scenario V_2 /unloaded swinging.

Figure 4.20 shows 3D acceleration profiles of both feet for experimentation and simulation. For both cases, similar shapes of acceleration are observed in single support. In simulation, a first smaller acceleration peak occurs at initial swing (about 30% of single support), and the larger acceleration peak occurs at the initial flat foot contact with the ground which marks the impact instant (50% GC). In contrast to experiments, where a smooth transition in acceleration signal is observed, there is an abrupt jump in simulation signal from peak

acceleration to zero at the impact instant, because the double support is considered instantaneous. In the experimental signals, the values of peak accelerations of the swinging foot are slightly different between the two steps. In contrast, these values are identical in simulation because the definition of the walking gait cycle implies that both legs have exactly the same movement during the swinging phase.

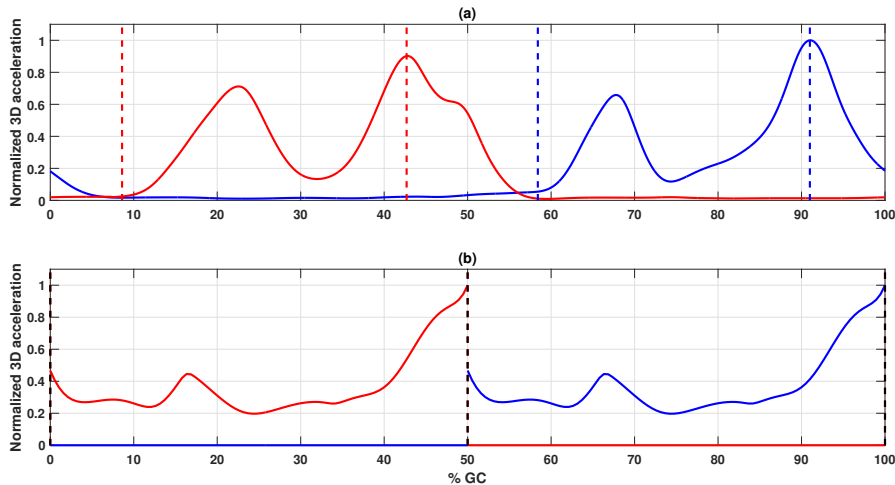


Fig. 4.20 3D acceleration profile of the right (blue) and left (red) foot during a GC: (a) experimental data for the walking condition $V_2/(S1)$, (b) simulation data (V_2 /unloaded swinging). The dashed lines indicate SS phases for (a) and impact instants for (b).

Similar shapes of COM's vertical acceleration profiles are obtained for simulation and experimental cases (cf. figure 4.21). In experiments, two peaks occur in each double support and for simulation, peaks occur at initial and final subphases of single support. A very small difference in peaks values is mainly due to the difference between joint velocities and accelerations before and after the instantaneous impact. In contrast, there is a large difference between each two peaks occurring at the same double support phase. In both approaches, the negative peaks are attained in single support phases. In simulation, the same COM vertical acceleration profile is obtained for both single support phases. However, in experiments, acceleration profiles during these phases are quite different.

Figure 4.21 shows shapes of 3D acceleration of the hand during gait cycle. In experimental data, peaks of 3D acceleration are observed in double support phases. In simulation, maximum values of hand's acceleration are obtained just after the impact instants. In both experiments and simulation, minimum acceleration values are reached in single support phases during arm swing motion.

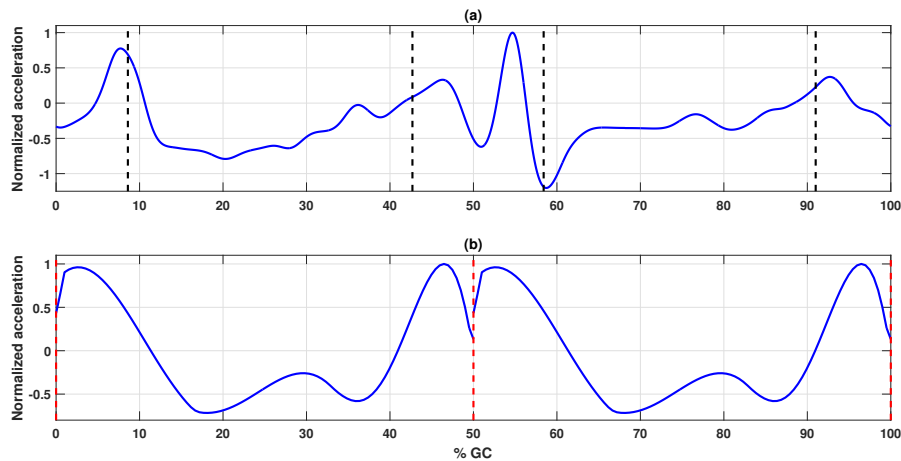


Fig. 4.21 Vertical acceleration profile of the COM during a GC: (a) experimental data for the walking condition $V_2/(S1)$, (b) simulation data (V_2 /unloaded swinging). The black dashed lines indicate DS phases, and red dashed lines indicate impact instants.

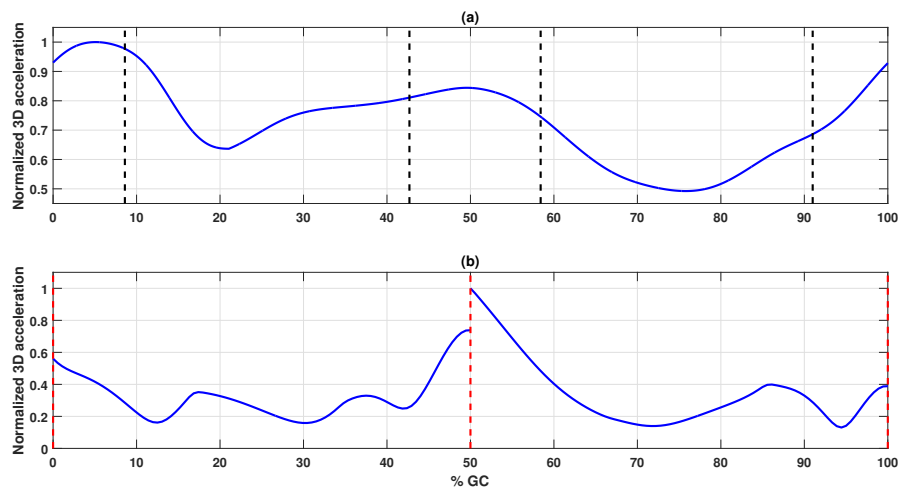


Fig. 4.22 3D acceleration profile of the hand during a GC: (a) experimental data for the walking condition $V_2/(S1)$, (b) simulation data (V_2 /unloaded swinging). The black dashed lines indicate DS phases, and red dashed lines indicate impact instants.

4.8.2.3.2 Acceleration items Figure 4.23 shows data related to acceleration parameters of the COM and hand. It is observed that acceleration items have the same variation trend in terms of gait velocity. In both experimentation and simulation, these variables increase for faster gait velocities. This is due to greater arm swing magnitude, and to an increased vertical displacement of the COM. COM's vertical acceleration items are lower in simulation than in experimental case (except for low velocity), which means that the gait model successfully produces smooth displacement of the COM, even at high gait velocities. In contrast, when

it comes to the hand, an inverse observation is made: simulation values are higher than experimental ones, with a two-fold increase.

For hand's RMS acceleration, the large difference between experimental values and those of simulation is mainly due to the fact that the double support is considered instantaneous and to the limited number of intermediate knots considered in simulation (two intermediate knots). A double support phase with finite duration should be considered in future work to avoid high acceleration jump at the impact, and a higher number of intermediate knots should be considered in order to have smoother joint acceleration profiles (for shoulder and elbow joints) and consequently acceleration related characteristics closer to experimental ones.

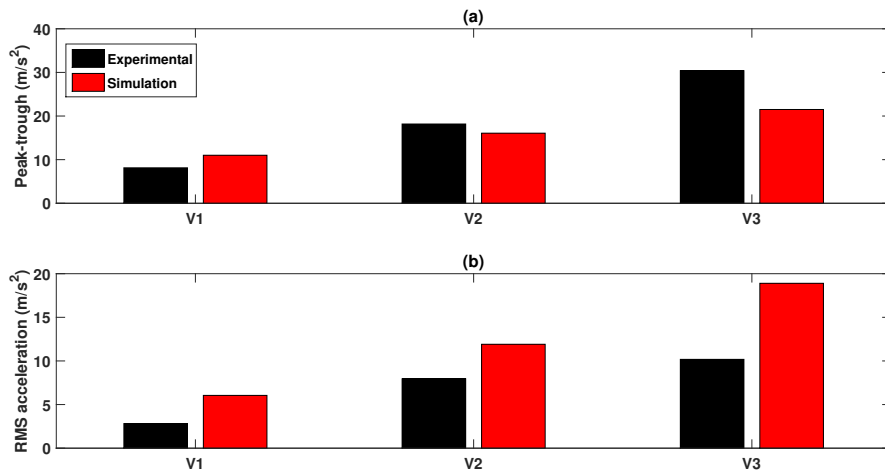


Fig. 4.23 (a) The peak-trough differences of COM's vertical acceleration and (b) RMS values of hand's 3D acceleration according to different gait velocities.

4.9 Conclusions and contributions to autonomous geolocation

In this chapter, we presented a 3D human gait model capable of coping with some human gait variability in terms of physical properties and walking speed. To check the validity of this model, we compared simulation outputs with kinematic profiles and accelerometric features obtained from walking experiments presented in Chapters 3 and 5. Results showed that the model reproduces similar fundamental patterns of walking found in experiments. Furthermore, the same variation trend of acceleration related items in function of gait velocity is observed for both simulation and experimental approaches. Based on these results,

simulation approach can serve to simultaneously predict user's displacement characteristics (e.g. step length) and features of acceleration signals sensed by handheld devices. With further improvements, if the framework is able to predict the gaits that constitute normal locomotion with a high degree of confidence, relationships between both data can be established for more accurate step length estimation.

In comparison with previous human walking models, the main contribution of our model is the accuracy of step length estimation. In fact, in the majority of previous walking models that optimize gait motion to minimize the energy required, the step length is either predetermined a priori (Aoustin and Formalskii [139], Kim et. al [14]), or constrained by empirical relationship with the gait speed and leg length (Alexander [46, 194], Minetti et al. [74]). If instead the step length is optimized during the process, an overly low prediction of step length is obtained. For instance, Alexander [194] adopted an inverse pendulum model to predict optimal walking gaits. When this simple mathematical model was used to calculate costs for different stride lengths, it showed very short strides as optimal. Besides, Kumar et al. [157] optimized human gait motion in the sagittal plane using an 11-link skeletal model. For the studied speed range 0.4-1.6 m/s, the optimal step length was no more than 60 - 70% of its experimental value. In contrast, our 3D gait model successfully predicts the optimal step length for the tested gait velocities with an estimation error lower than 7%. Note that the introduced pelvis rotation in transverse plane at double support configuration (the variable p_5 in figure 4.16) had a major contribution to having longer steps as optimum.

Despite the disparities between signals from simulation and experiments, our model contributes to better estimating hand acceleration feature with respect to planar human gait modeling. For instance, the 2D human gait model in the sagittal plane developed by Kumar [195], taking into account the same assumptions for double support (i.e. instantaneous impact with flat foot contact with the ground), produced a very poor prediction of hand acceleration signals during gait cycle. In fact, the 2D norm of handheld device's acceleration calculated from simulation showed a very large acceleration jump at impacts, and the magnitude of 2D acceleration norm was at least 10 times that of 3D acceleration norm calculated from the experiments (see appendix F). In contrast, our generated gait cycles showed only a two-fold increase of acceleration items related to the hand.

In contrast to simulation signals, experimental acceleration patterns related to feet and COM have shown different profiles for each single support phase. Given the adopted gait cycle definition, our model is unable to cope with the asymmetry observed in these acceleration

profiles, since the walking motion of the second step is generated from the optimized first step motion using the symmetry property of the skeletal structure. The asymmetry in acceleration signals must be the result of asymmetric movements of the locomotor system limbs from one step to the other. We suggest that these asymmetric movements are likely to result in a step-level asymmetry of displacement features.

The temporal aspect of this asymmetry will be investigated in the next chapter to find out whether the asymmetry level of gait cycle during steady walking, probably caused by handling a mass in hand, is significant in the context of pedestrian navigation solution. This investigation will help us to determine if it is necessary to extend the presented optimization procedure to the stride level, for a more reliable prediction of human walking movements during gait cycle.

Chapter 5

Study of walking gait asymmetry induced by a handheld device

5.1 Introduction

One of the disparities found between the proposed gait model and real walking is that the latter produces asymmetric acceleration patterns for relatively stable parts of human body. This asymmetry is probably the result of a difference between right and left steps characteristics (i.e. duration, length). This defeats the general assumption in PDR strategy: the presence of a device in hand does not impact the gait symmetry and all steps are identical for a fixed walking speed. This hypothesis, which is commonly used to estimate the traveled distance, is investigated in this chapter with an experimental study with several subjects, designed to study the influence of a mass carried in hand on the walking gait cycles. Either a temporal or spatial step-level asymmetry resulting in a significant error on the estimation of traveled distance can justify the need of extending the gait model presented in the previous chapter to the stride level. We choose to make the hypothesis that the presence of a device in hand may alter the temporal step level symmetry of the walking gait. Experiments are supported with a walking gait simulator in the sagittal plane designed for a 2D biped with two identical three-link legs, a head-trunk, and two identical two-link arms linked by actuated revolute joints. Both approaches results are analyzed to find out whether the step durations are still equal when holding a 0.19 kg mass in one hand, equivalent to a smartphone mass.

5.2 Human motion capture experiments

5.2.1 Experimental setup

The experiments were conducted in a motion capture room where a treadmill was installed (cf. figure 5.1). 17 reflective clusters of markers were placed on each subject's feet, legs, pelvis, trunk, head, arms, forearms and hands for getting accurate reference trajectories of these locations. While each subject walked on a treadmill, an 8-camera (four on the floor and four close to the ceiling) ART IR tracking system recorded the displacement of the markers in three-dimensional space at 60 Hz sampling frequency (cf. figure 5.1). Inertial data were also collected using an ULISS device held by the right hand of the subject. Optical markers' assembly was tapped to this device (cf. figure 5.2) in order to project sensor's data in motion lab frame. The handheld mass weighed 0.19 kg, which corresponds to the mass of a smartphone.

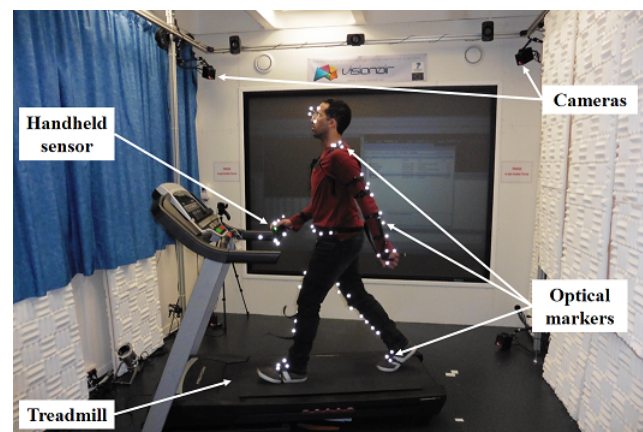


Fig. 5.1 Experimental setup of motion capture experiments

Walking on a treadmill is acknowledged as being different from natural walking. It is demonstrated that the treadmill induces a more symmetric and consistent gait pattern [196–198]. However, the study requires accurate measurements of the markers' positions in order to derive gait features. This was made possible with a qualified motion capture system whose workspace is limited to approximately 10 m². Natural walking could not be possible in this room because only too short distances (in circles) could be traveled by the individuals in this space. Therefore, the use of a treadmill, located in the center of the motion capture room, was preferred to test straight walking scenarios. Another advantage of this alternative is that the study could be conducted for several steady walking speeds.



Fig. 5.2 Handheld device equipped with an optical markers' assembly

5.2.2 Subjects and scenarios

Ten healthy individuals, six men and four women, with a 31 year average age (age range 21-52 years), 1.72 m average height (with shoes) and 74.9 kg average mass, volunteered to participate in this experimentation. All participants were provided written informed consent (institutional review board ethical process). The trials started after all participants were acquainted with the treadmill and the device at the three following velocities: $V_1 = 3.6$ km/h (1 m/s), $V_2 = 5$ km/h (1.39 m/s) and $V_3 = 5.8$ km/h (1.61 m/s). Data record started only after a participant had reached a steady state at each walking speed. In addition, all participants were unaware of the specific data processing.

The experiments were conceived to test the influence of holding a connected object in hand on the gait cycle. Therefore, experiments were conducted for three different device carrying modes, corresponding to different scenarios. They are:

- the *unloaded swinging mode*: the participant is naturally walking with no mass in hand, i.e. the arms are freely oscillating during the walk;
- the *loaded swinging mode*: the participant is naturally walking while holding the device in his/her swinging hand;
- the *texting mode* that corresponds to a body fixed device carrying mode: the participant is instructed to walk watching his/her device's screen so that the right upper limbs configuration is comfortable for reading or texting on the device.

Each scenario was performed for all three testing velocities V_1 , V_2 and V_3 .

5.2.3 Parameters used to assess the gait symmetry

First, the ZVD method (presented in section 3.4.1.1) is applied to extract the step events from the acceleration data. It is obtained by double differentiating the feet markers' positions, which are tracked by the motion capture system. In order to remove the noise induced by the derivation, the data are low-pass filtered with a zero-phase forward and reverse second order Butterworth filter with a cut-off frequency of 10 Hz. Then, three different features are defined to analyze the symmetry of the walking gait:

- *Step Duration*. This is the time elapsed between two successive detected steps. Step durations are calculated for both legs. Labels are used to differentiate right step duration from left step duration.
- *Temporal Symmetry Index (TSI_{step}) over step*. TSI over step is defined as the ratio of time duration of the step on the device's side over the total duration of a stride [2] as defined in (3.1). This index is useful for studying the temporal step symmetry. For step symmetric walking gait, TSI over step should be 0.5.
- *Temporal Symmetry Index (TSI_{stride}) over stride*. Similarly, TSI over stride is defined as the ratio of time duration of the first stride over the duration of two successive strides. This index is useful for assessing the step detection method. An accurate step detection should result in a stride level symmetric gait irrespective of the presence of mass in one hand [78].

5.3 Evaluation of walking gait step-level symmetry

5.3.1 Experimental results

200 continuous steps (100 continuous strides) were analyzed for each trial using the ZVD method. To assess the accuracy of this step detection method, TSI over strides were analyzed. It was found that for all subjects, and across any of the conditions evaluated, the TSI_{stride} values follow Gaussian distributions and are centered around 0.5, with all standard deviations remaining below $6 \cdot 10^{-3}$. This result asserts the precision of ZVD method.

The analysis of the walking gait symmetry over steps is conducted using the two-factor repeated measures analyze of variance (RM ANOVA) [199]. To apply the ANOVA analysis, all TSIs are expected to follow Gaussian distributions for the different scenarios [199]. This is effectively observed with the experimental data sets and illustrated in figure 5.3, figure 5.4 and figure 5.5 where the TSI_{step} and the associated probability density functions are plotted

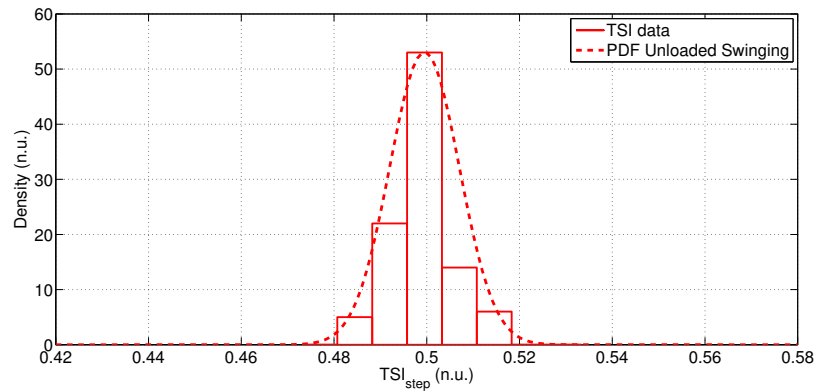


Fig. 5.3 Probability density function of the TSI_{step} for the unloaded swinging mode at 5 km/h for one typical test participant

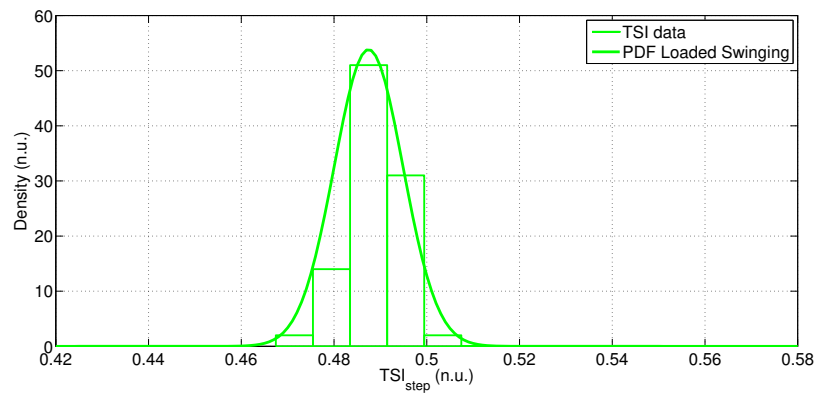


Fig. 5.4 Probability density function of the TSI_{step} for the loaded swinging mode at 5 km/h for one test participant

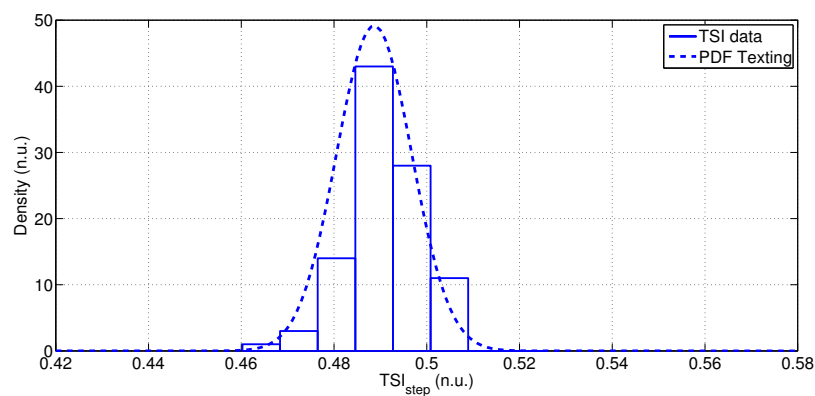


Fig. 5.5 Probability density function of the TSI_{step} for the texting mode at 5 km/h for one test participant

for the three different scenarios at 5 km/h for one test subject. A shift of the Gaussian mean is observed on these three figures between the natural unloaded arm swinging case that is centered at 0.5 and the two other cases.

In total, 9000 strides were analyzed corresponding to the three carrying modes and the three walking speeds. RM ANOVA is applied to the TSI_{step} to assess possible changes of the walking gait symmetry over steps induced by the presence of a mass in hand. Two RM factors are considered. They are the device carrying mode factor and the walking speed factor. For the analysis, the three carrying modes and the three walking speeds are all processed together. The results of the RM ANOVA are given in Table 5.1.

Table 5.1 Results of the repeated measures analysis (RM ANOVA) applied to TSI_{step}

influencing factor	SS	df	MS	F	p
Carrying mode (CM)	9.3×10^{-4}	2	4.65×10^{-4}	5.530	0.013
Walking speed (WS)	8.8×10^{-5}	2	4.42×10^{-5}	0.243	0.7870
CM x WS	7.6×10^{-4}	4	1.90×10^{-4}	2.986	0.0316

In the RM ANOVA analysis, an F-test is used to find out whether the factors of interest affect the TSI_{step} . The analysis is conducted using a variance ratio of two sets of TSI_{step} values. We used the classical 5% threshold for the p-values below which an effect will be considered significant. In Table 5.1, it is found that the carrying mode has a significant influence on the TSI_{step} , and therefore the gait symmetry, with a 1.34% p value. On the contrary, the analysis shows that the walking speed factor has no significant influence on the gait symmetry since the corresponding p value is much greater than 5% (78.7%). The p value for the interaction of the factors "Carrying mode" and "Walking speed" equals 3.16%, which indicates that the influence of the carrying mode on the gait symmetry depends on the walking velocity. To deepen this analysis, the RM ANOVA is conducted on the TSI_{step} for each walking speed (V_i , $i=1, 2, 3$) individually. The results are given in Table 5.2.

Table 5.2 Effect of carrying mode factor on TSI_{step} for the different gait speeds

Walking speed	Effect of carrying mode factor		
	MS	F	p
$V_1=3.6$ km/h	5.1×10^{-4}	12.487	3.97×10^{-4}
$V_2=5$ km/h	1.71×10^{-4}	6.639	6.92×10^{-3}
$V_3=5.8$ km/h	1.66×10^{-4}	1.142	0.341

The carrying mode has a significant influence on the gait symmetry at the step level for the low and medium speeds. The carrying mode effects are essentially the same for the two velocities (a decrease in TSI value). On the contrary, for the highest walking speed with a

34.1% p value, no significant effect of the carrying mode on gait step symmetry is observed.

Looking at each test participant, figure 5.6 shows the average TSI_{step} for all walking speeds with the three device carrying modes. All TSI numbers are expressed to four significant digits. A tendency may be concluded for the loaded swinging and texting cases with respect to unloaded swinging mode. Indeed, average TSI_{step} decreases for 8 participants out of 10 between the unloaded swinging mode and the two others. The average TSI_{step} mean value for all participants in the unloaded swinging mode is 0.4997. In loaded swinging and texting modes, a 0.4920 and 0.4943 average TSI_{step} are found respectively.

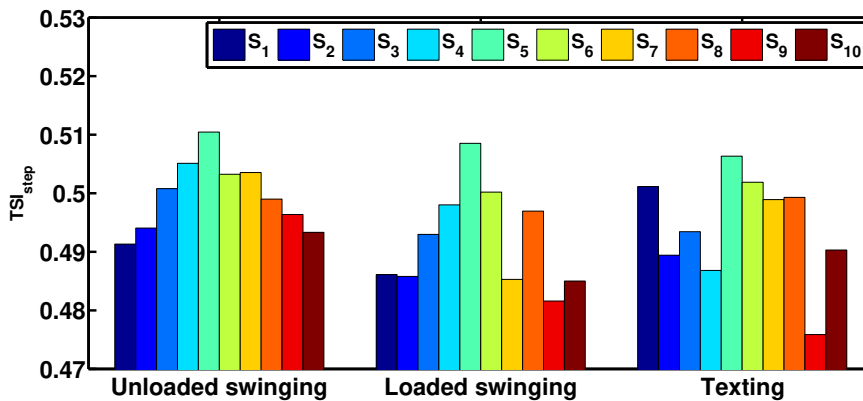


Fig. 5.6 Averaged TSI_{step} of each participant in the three device carrying modes (considering all the walking velocities). TSI_{step} mostly decreases for the loaded swinging and texting cases with respect to unloaded swinging mode.

A post-hoc analysis using Tukey's HSD test shows that the unloaded swinging and loaded swinging modes are significantly different and none of these two modes is significantly different from the texting case. This is further illustrated in figure 5.7 where the texting and unloaded swinging modes, in blue and red respectively, overlap.

Note that the asymmetry levels found in experiments are low compared to those found by clinicians. In fact, the asymmetries observed are of the same order as what is conventionally observed for healthy people, in normal condition (i.e. a non-pathological person, walking in unloaded swinging condition at comfortable speed) [200, 201]. This could result from the use of a treadmill, the large number of strides considered (100 per trial), or the step instant detection method: we used the ZVD on filtered and differentiated kinematic data instead of the more classical methods used in biomechanics (e.g. Zeni et al. [202]). Generally, we have higher asymmetry indexes than the average indexes observed in loaded swinging and

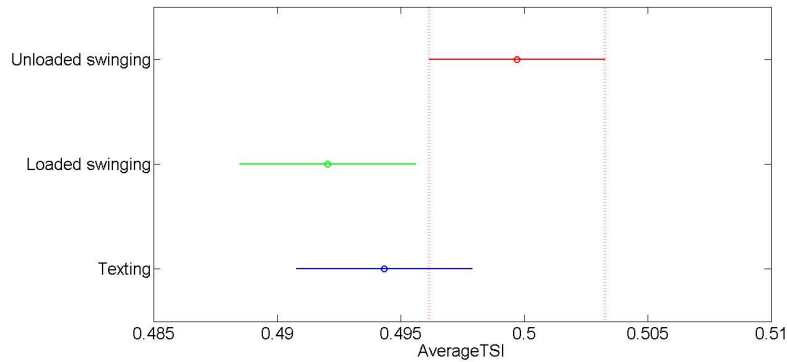


Fig. 5.7 Tuckey's HSD test for the three device carrying modes (considering all the walking velocities). Each group mean is represented by a small circle, and each comparison interval is represented by a bar extending out from the mean value. Two group means are significantly different if their intervals are disjoint. They are not significantly different if their intervals overlap.

texting cases. However, these relatively low gait asymmetries may have a significant impact on the estimated traveled distance for pedestrian navigation applications, which leads to accumulative errors throughout the user's displacement. This impact will be investigated in section 5.3.3.

5.3.2 Simulation results from a human gait model in the sagittal plane

To support the results of our experimental analysis, the 2D biped model, shown in appendix E, is fitted to one test subject (mass = 100 kg, height = 1.85 m). DeLeva regressions [203] are used for BSIPs estimation, and the anatomical definition proposed in the anthropometric tables [108, 203] are used for segments lengths estimation. Gait motion in the sagittal plane was predicted using parametric optimization technique. A handheld mass linked to the right forearm is considered in order to observe the temporal step-level symmetry in different device carrying modes. The stride is assumed as the gait cycle, and it is also assumed that both steps have the same length but their durations can be different. When the handheld mass is set to zero, i.e. unloaded swinging case, a cyclic gait motion is achieved with single support and instantaneous double support phases that are symmetric with an exchange of role of legs after each step. In fact, The TSI_{step} is found to be 0.5 for varying walking velocities within the speed range 0.4-1.6 m/s.

When switching the load mass to 0.19 kg, the gait cycle is no longer symmetric over steps in both swinging and texting scenarios. For instance, in loaded swinging mode, TSI_{step} is

found to be 0.4984 for the gait velocity V_2 (5 km/h) i.e. the durations of both steps (right and left) are no longer equal. Since the simulation starts from the right step, it is found that right leg stance phase duration is a bit greater than the left one when a mass is carried in the right hand.

5.3.3 Impact on the estimation of traveled distance for pedestrian navigation applications

Existing step length models in pedestrian navigation algorithms usually assume that the walking gait is step/stride symmetric irrespective of the presence of a mass in hand. Our results have shown that this is not the case. Because pedestrians can change directions at every step, it would not be sufficient to estimate only stride length. The risk would be to miss some angular changes in the walking direction and accumulate errors in the estimated PDR trajectories. Consequently it is interesting to assess the impact of this assumption on the traveled distance estimate.

5.3.3.1 Position estimation error

Let us quantify the position estimation error due to the walking gait asymmetry in a step symmetric modeling. An example of step length model is given by [20]. In this model, the step length s is related to the step frequency f and user's height h by:

$$s = h(af + b) + c \quad (5.1)$$

Where $\{a, b, c\} \in \mathbb{R}$ is a set of real parameters adjusted to the person. Thus, if all steps are identical as assumed in PDR navigation algorithms, we have:

$$\Delta_{S_D} = \Delta_{S_G} \quad (5.2)$$

where Δ_{S_D} is the right step duration and Δ_{S_G} is the left step duration. In this case, the stride duration is given by:

$$\Delta_{\text{Stride}} = \Delta_{S_D} + \Delta_{S_G} = 2\Delta_{S_D} \quad (5.3)$$

Considering the asymmetry induced by the handheld device, equation (5.2) becomes:

$$\Delta_{S_D} = \text{TSI} \cdot \Delta_{\text{Stride}} \quad (5.4)$$

Thus, it is possible to estimate the induced error ε and the error ratio $\varepsilon\%$ that are given by the following equations:

$$\begin{cases} \varepsilon = (2 - \frac{1}{\text{TSI}})\Delta S_D = (\frac{2\text{TSI}-1}{\text{TSI}})\Delta S_D \\ \varepsilon\% = | \frac{2\text{TSI}-1}{\text{TSI}} | \times 100 \end{cases} \quad (5.5)$$

5.3.3.2 Predicted errors based on empirical data

In the experiments, TSI_{step} mean value is $\mu_{\text{TSI}_1} = 0.4920$ for the loaded swinging mode and $\mu_{\text{TSI}_2} = 0.4943$ for the texting mode, representing respectively the error ratios $\varepsilon_{1\%} = 3.25\%$ and $\varepsilon_{2\%} = 2.3\%$. For a constant walking velocity, and considering 1 m long strides, the estimated error over a 100 m traveled distance without considering the gait asymmetry equals 3.25 m and 2.3 m for the loaded swinging and the texting modes respectively. These errors are significant for pedestrian navigation applications. Since the treadmill tends to make the gait more symmetric, higher errors are expected for overground walking. This suggests that the step length models should be improved for the context of handheld sensors.

Table 5.3 Error ratio $\varepsilon\%$ in % over the traveled distance for each participant and for the different trials

participant	Loaded Swinging			Texting		
	$\varepsilon\%(V_1)$	$\varepsilon\%(V_2)$	$\varepsilon\%(V_3)$	$\varepsilon\%(V_1)$	$\varepsilon\%(V_2)$	$\varepsilon\%(V_3)$
S ₁	10.26	3.02	4.00	5.39	2.25	8.47
S ₂	14.94	0.82	2.34	6.78	5.72	0.56
S ₃	4.40	2.91	1.25	6.38	3.30	1.54
S ₄	0.07	1.14	3.66	0.19	3.53	13.38
S ₅	3.22	3.09	3.73	2.75	0.70	4.00
S ₆	2.54	2.22	0.50	0.26	0.58	1.92
S ₇	7.02	0.92	10.47	2.76	1.44	2.70
S ₈	6.02	0.93	1.23	0.89	0.26	0.21
S ₉	5.13	1.54	16.86	0.26	9.78	22.09
S ₁₀	9.57	4.10	4.95	0.86	8.61	2.53
Mean	6.32	2.07	4.90	2.65	3.61	5.74

In Table 5.3, the position estimation error ratio $\varepsilon\%$ corresponding to each trial (carrying mode / walking speed) is reported for all test participants. These values correspond to the average TSI_{step} values. In the loaded swinging mode, the impact on traveled distance estimation is found to be greater at lower speed ($\varepsilon\%(V_1) = 6.32\%$) than at higher walking velocities. Indeed, at higher speed, the synchronization between the arms and the legs increases and the impact of the added mass is found to be less significant. On the contrary, for the texting mode, the fact of walking with rigid upper limbs has a greater impact on the position estimation

at higher walking velocities ($\varepsilon_{\%}(V_3) = 5.74\%$). In this scenario, the loaded arm is not synchronized with the legs movement. This outcome completes the results found in table 5.2.

5.3.3.3 Comparison with predicted errors from simulation

Based on simulation model, the position estimation error ratio is calculated for the walking velocities V_1 , V_2 and V_3 to compare with the results based on the empirical data. The error ratios corresponding to loaded swinging and texting modes are shown in table 5.4.

Table 5.4 Error ratio $\varepsilon_{\%}$ in % based on simulation results for all testing speeds and for different carrying modes

Gait speed	Loaded Swinging			Texting		
	V_1	V_2	V_3	V_1	V_2	V_3
$\varepsilon_{\%}$	1.94	1.38	1.87	1.08	2.52	3.04

The error ratios calculated based on the conceived human gait model are much lower than mean values found with experimentation data. This is due to several limitations of the proposed model. The identified limitations and recommendations for enhancement of the current model are the following:

- It has been assumed that most features of human walking can be captured by analyzing it in sagittal plane. This can be true for leg movements. However, the observation of the positions of the hand markers shows that humans tend to increase their movement in the horizontal plane with an increase in walking speed. Hence, to study human walking with arm swinging, 3D model should be considered.
- For the simplicity of walking gait cycle design, double support phases were neglected. Humans have a well-defined double support phase which should not be neglected to capture all the features of human walking gait in the simulation.
- The simulation tool is unable to model the cognitive effects of interacting with a device (dual-task paradigm), interaction with other individuals, and making maneuvers.

5.4 Conclusions and contributions to autonomous geolocation

The impact of the handheld mass on the walking gait is studied with experimental data collected with 10 test participants and a 0.19 kg handheld device in a motion capture laboratory. It is shown that the presence of a mass in hand changes the gait symmetry at the

step level whereas the gait remains stride symmetric. As compared to a naturalistic walking (i.e. without any mass in hand), it is also found that both carrying modes: mass held in a swinging hand and in a "texting" hand, have impact on the walking gait. For swinging mode, the impact of carrying a mass in hand is found to be greater at lower speeds than at comfortable/faster speeds, which is expected because parasitic motion is more likely to occur at slow speeds since the energy conservation problem is less constraining. In contrast, an inverse tendency is observed for texting mode. These findings tend to prove the importance of natural arm swinging that could be captured with handheld devices.

This study is completed with a walking motion generator based on robotics and designed for a humanoid with a mass in hand. This generator computes the joints' trajectories based on a stride level optimization. Human walking motion is simulated only in the sagittal plane to compare with 3D experimental data. Globally, the same trend (i.e. modification of the walking gait symmetry at the step level) is found even if some disparities are observed. The hypothesis is that they are mainly due to the fact that the model is restricted to the sagittal plane.

Another important result for the field of pedestrian navigation based on inertial navigation systems is that the presence of a handheld mass should be considered to adapt step length models that are used in PDR processing strategy. Indeed, it is commonly assumed in the literature that all the steps are identical when a human is walking with a handheld device at a steady velocity. The outcome of this research shows that this assumption is a source of significant error in the computation of the cumulative traveled distance. Therefore, predicting gait motion over a stride is more viable to solve for the direct modeling problem of pedestrian navigation.

Chapter 6

3D human gait simulator extended to stride level

6.1 Introduction

In the previous chapter, it was proven that, for steady walking, both steps are no longer identical due to the presence of a mass in hand. The induced asymmetry is significant for the estimation of traveled distance for pedestrian navigation solutions. Therefore, asymmetric gait patterns are considered in the new formulation of the optimization problem, and step lengths and durations for the two sides may be different. The new gait cycle is then defined as two consecutive steps (i.e. a stride), and modifications on optimization variables, constraint and cost functions will be detailed. For loaded swinging and texting scenarios, gait motions over a stride are predicted for three gait descriptors: average gait velocity, stride characteristics (length, width), and step-level symmetry indexes. The last two descriptors have been added compared to the previous model to specify the characteristics of the steps and to simulate the acceleration of the hand resulting from the induced movement of the loaded arm. Note that these two descriptors will reduce the solution space for the locomotor system.

6.2 Gait cycle composed of two consecutive steps with instantaneous impacts

For stride-level optimization, we consider a gait cycle composed of a right single support phase, an instantaneous double support, a left single support phase, and a second instantaneous double support. In both double support phases, we consider the same assumptions

adopted for the previous gait cycle definition.

We consider a cyclic gait motion over a stride of length d and width w , in the time interval $[0, T]$, where T is the stride duration. For an imposed gait velocity V , the stride duration is given by $T = \frac{d}{V}$. Then, the duration and length of the step i , respectively T_i and d_i , $i = 1, 2$, are determined using the imposed step-level symmetry indexes (TSI, SSI):

$$\begin{aligned} T_1 &= \text{TSI} \times T, & T_2 &= (1 - \text{TSI}) \times T \\ d_1 &= \text{SSI} \times d, & d_2 &= (1 - \text{SSI}) \times d \end{aligned} \quad (6.1)$$

Note that both right and left steps have the same width w since steady straightforward gait is studied.

In order to facilitate gait modeling over a stride, we aim at using the same parameterization of geometric model for both steps. This implies that the right foot remains as the support foot with the reference frame R_s linked to it. A left step (left support foot) with a mass carried in the right hand is dynamically equivalent to a right step with the same mass carried in the left hand, since in both cases we have the same mass distribution with respect to the structure's fixed base (support foot). From this statement, the cycle can be modeled by the following phases (cf. figure 6.1):

- A right single support phase with the mass carried in the right hand ($0 < t < T_1$);
- An instantaneous impact where the front foot is the left foot distant from the rear foot by d_2 along the \mathbf{z}_s axis ($t = T_1$);
- A right single support phase with the mass carried in the left hand ($T_1 < t < T$);
- An instantaneous impact where the front foot is the left foot distant from the rear foot by d_1 along the \mathbf{z}_s axis ($t = T$).

Then, the configurations during the second step, i.e. left step, are deduced from the configurations of the last two phases listed above, using the same transformations mentioned in section 4.3.1, while considering the length of the second step d_2 :

$${}^s\mathbf{T}_{s'} = \begin{bmatrix} 1 & 0 & 0 & 0 \\ 0 & -1 & 0 & -w \\ 0 & 0 & 1 & d_2 \\ 0 & 0 & 0 & 1 \end{bmatrix} \quad (6.2)$$

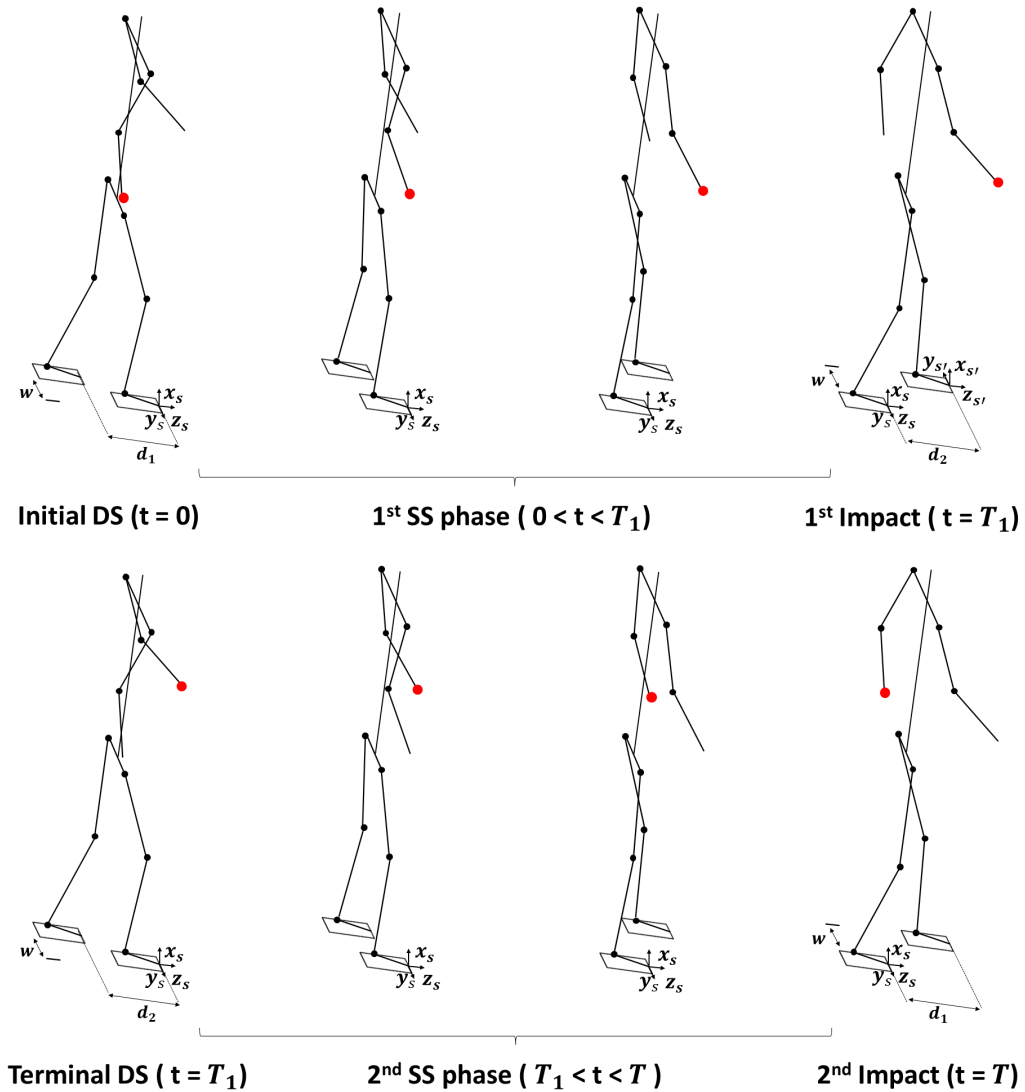


Fig. 6.1 GC composed of two SS phase and two instantaneous impacts (the red dot stands for the carried mass).

6.3 Optimization variables for stride-level optimization

Since joint histories are interpolated over two steps, $38 \times (N+4)$ interpolation parameters are needed for stride-level optimization. Thanks to modeling assumptions detailed in section 4.6, the optimized vector is reduced by 88 variables for optimization over stride. Four additional parameters, which are $(p_{6,j}, p_{7,j})$, $j=1,2$, are subtracted from the optimization variables since the spatial parameters of the steps are predetermined.

For a cyclic walking gait over a stride, the optimized set comprises for each step the variables presented in Table 6.1. The number of variables is reduced in texting mode due to the constrained arm configuration. Corresponding joint rate variables are set to zero and joint positions are fixed so that the hand has a defined position with respect to the head i.e. The position of the origin O_{20} linked to the hand with respect to the origin O_{16} linked to the head is ${}^{16}\mathbf{P}_{20} = (\frac{-L_8}{2}, \frac{-2L_{10}}{3}, \frac{-L_7}{2})_{R_{16}}$, where L_7 , L_8 , and L_{10} are respectively the trunk length, the lateral distance between the head and shoulder joint center, and forearm length.

Table 6.1 Optimization variables corresponding to the step labelled j , $j=1,2$ and to N intermediate time knots. (S): Swinging mode, (T): Texting mode.

Set of variables	Number of variables	
	(S)	(T)
$\mathbf{q}_j(t_{i,j})$, $i=1, \dots, N$: Intermediate configurations	$19N$	$16N$
$\dot{\mathbf{q}}_j(T_j)$: Joint velocities just before the impact	19	16
$(p_{1,j}, p_{2,j}, p_{3,j})$: Hips center position in initial DS	3	3
$(p_{4,j}, p_{5,j})$: Initial pitch and yaw orientations of the pelvis	2	2
$\mathbf{q}_{j,arm}(t=0)$: Arms configuration in initial DS	6	3

Thus, for a cyclic walking gait over a stride, we have $38N+60$ optimization variables for swinging mode and $32N+48$ optimization variables for texting mode. As for step-level optimization, "fmincon" function based on the active set algorithm is used to determine the optimal set of variables.

One can notice that the extension of gait cycle definition to the stride level led to a significant increase in the number of optimization variables. In an attempt to avoid the convergence to local minima, we tested an optimization strategy called variables block strategy [204]. This strategy consists in solving the problem iteratively by dividing variables into blocks according to their physical significance and optimizing each block mainly in the corresponding sub-iteration. There are three blocks in our case: joint velocities variables, locomotor system configuration variables, and upper body configuration variables. By applying variables block strategy with dynamic adjustment on constraints, optimization results are improved and the optimized cost functional is lower. However, this strategy is discarded because of its very long computational time, but it may be considered in future developments. The results that will be presented in section 6.5 correspond to optimizing all variables simultaneously.

6.4 Specific constraints and cost functions

For the cyclic walking gait over a stride, the constraints in single and double support configurations, listed in section 4.7.1, are imposed for both steps. In texting mode, the biomechanical and geometric constraints on the constrained arm are not applied. In this scenario, an additional constraint keeps the same distance between the carried mass and the head.

In stride-level optimization process, we aim at minimizing the joint actuators energy dissipated over a stride of duration T to travel the distance d . For each step labeled j , of period T_j and length d_j , we consider a cost functional $C_{\Gamma,j}$ given by:

$$C_{\Gamma,j} = \frac{1}{d_j} \int_0^{T_j} \mathbf{\Gamma}_j(t)^\top \mathbf{\Gamma}_j(t) dt \quad (6.3)$$

where $\mathbf{\Gamma}_j$ is the $N_j \times 1$ vector of joint torques during the step j . The energetic cost function of the stride C_Γ can be expressed in function of cost functionals of both steps $C_{\Gamma,1}$ and $C_{\Gamma,2}$ as follows:

$$\begin{aligned} C_\Gamma &= \frac{1}{d} \int_0^T \mathbf{\Gamma}(t)^\top \mathbf{\Gamma}(t) dt \\ &= \frac{d_1}{d} \cdot \left(\frac{1}{d_1} \int_0^{T_1} \mathbf{\Gamma}_1(t)^\top \mathbf{\Gamma}_1(t) dt \right) + \frac{d_2}{d} \cdot \left(\frac{1}{d_2} \int_{T_1}^T \mathbf{\Gamma}_2(t-T_1)^\top \mathbf{\Gamma}_2(t-T_1) dt \right) \\ &= \text{SSI} \cdot \left(\frac{1}{d_1} \int_0^{T_1} \mathbf{\Gamma}_1(t)^\top \mathbf{\Gamma}_1(t) dt \right) + (1 - \text{SSI}) \cdot \left(\frac{1}{d_2} \int_0^{T_2} \mathbf{\Gamma}_2(t)^\top \mathbf{\Gamma}_2(t) dt \right) \\ &= \text{SSI} \cdot C_{\Gamma,1} + (1 - \text{SSI}) \cdot C_{\Gamma,2} \end{aligned} \quad (6.4)$$

Note that in the specific case of a step symmetric walking gait, we have $\text{SSI} = 0.5$ and $C_{\Gamma,1} = C_{\Gamma,2}$, we thus have $C_\Gamma = C_{\Gamma,1}$.

Similarly to step-level optimization, we consider the deviation of the trunk from upright posture, which is amounted to the following function:

$$C_{UTP} = \int_0^T (\mathbf{p}_7(t) - \mathbf{p}_h(t)) \cdot \mathbf{g} dt \quad (6.5)$$

where \mathbf{p}_h and \mathbf{p}_7 are the Cartesian coordinates of the hips middle point and the 7th Cervicale, respectively, \mathbf{g} is the gravity vector and the operator \cdot denotes the scalar product.

Consequently, the cost functional for a stride is given by:

$$C_f = C_\Gamma + \rho \cdot C_{UTP} \quad (6.6)$$

where $\rho > 0$ is a penalty factor.

6.5 Validation results

In this section, we present results of the extended human gait model considering the same numerical parameters as for the step-level simulator, i.e. $N = 2$ intermediate knots and $n_s = 5(N + 1) + 1 = 16$ time samples for each step.

6.5.1 3D acceleration of the feet

Figure 6.2 shows the normalized 3D acceleration profiles of both feet throughout the walking cycle. One can notice that the durations of simple support are no longer equal for the model extended to the stride because of the imposed experimental TSI index that is different from 0.5. Although the signal shapes are similar, the temporal and spatial asymmetry between the two steps induced some differences between the acceleration profiles specific to each foot. First, there is a difference in acceleration values before/after impact between the two feet. Second, the relative time of acceleration peak instants during the swing phase changes from one step to the next (about 30% and 50% for the first and second steps, respectively). The disparities in signals between the two steps, which are not negligible for the experimental data, highlights the correlation between arm movement and foot acceleration. Moreover, optimizing the walking movement over a stride allows to obtain acceleration patterns closer to experimental ones. Indeed, for the extended model, the base of the first acceleration peak is wider and the value of the normalized maximum acceleration is higher.

For both simulation and experiments, peak values of acceleration profiles significantly increase with the gait velocity, and within the same velocity, there is no significant impact of carrying mode on these values.

6.5.2 COM's vertical acceleration

Normalized vertical acceleration profiles of the COM are depicted in figure 6.3. In contrast to the case of step-level optimization, the new gait cycle definition results in a remarkable difference between the two acceleration peaks occurring before and after each impact instant:

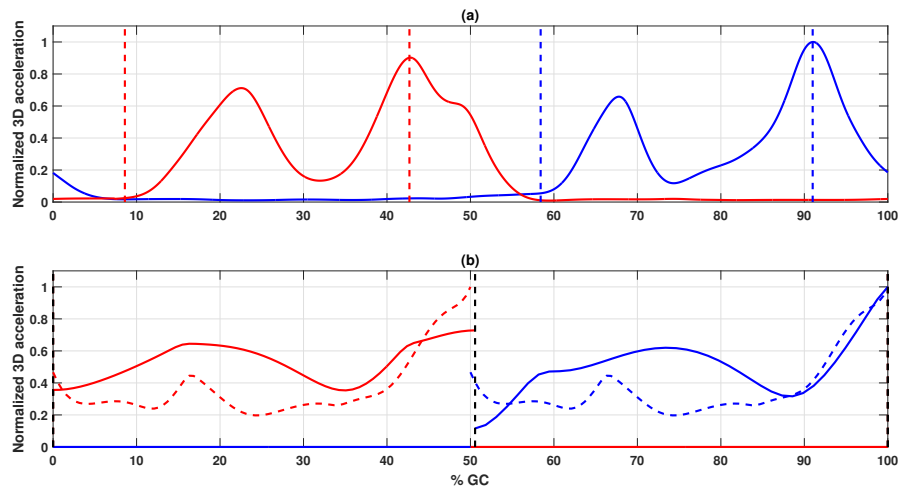


Fig. 6.2 3D acceleration profile of the right (blue) and left (red) foot during a GC for the walking condition $V_2/(S1)$: (a) experimental data, (b) simulation data (continuous/dashed curves correspond to optimization over stride/step). The dashed lines indicate SS phases for (a), and impact instants for (b).

the acceleration peak before the impact remains similar while the acceleration peak after the impact is largely reduced in the "optimization over stride" simulation. Besides, the magnitude of vertical acceleration jump at impacts is reduced for the extended simulator with respect to the previous gait model. Another difference between both models is that for stride-level simulator, higher magnitudes of negative acceleration are achieved in single support phases.

Figure 6.4 shows the differences between peak and trough values of COM vertical acceleration for different walking conditions. Our simulator provides the same variation trend in terms of gait velocity as in experimentation. Within the same device carrying mode, the peak-trough difference significantly increases with walking speed. For a given walking velocity, differences in vertical acceleration items are mainly due to differences between step length values.

In comparison with step-level optimization, the extended simulator provides lower vertical acceleration items of the COM, given the walking velocity (e.g. a 44% decrease for the velocity V_2). Therefore, it can be concluded that optimizing gait motion over a stride results in a smoother trajectory of the COM, but also in a related acceleration item further away from the experimental data.

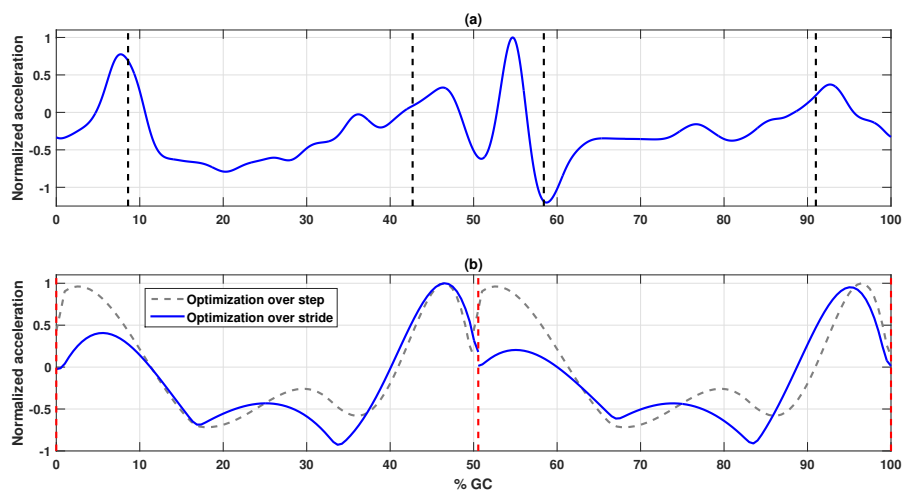


Fig. 6.3 Vertical acceleration profile of the COM during a GC for the walking condition $V_2/(S1)$: (a) experimental data, (b) simulation data. The black dashed lines indicate DS phases, and red dashed lines indicate impact instants.

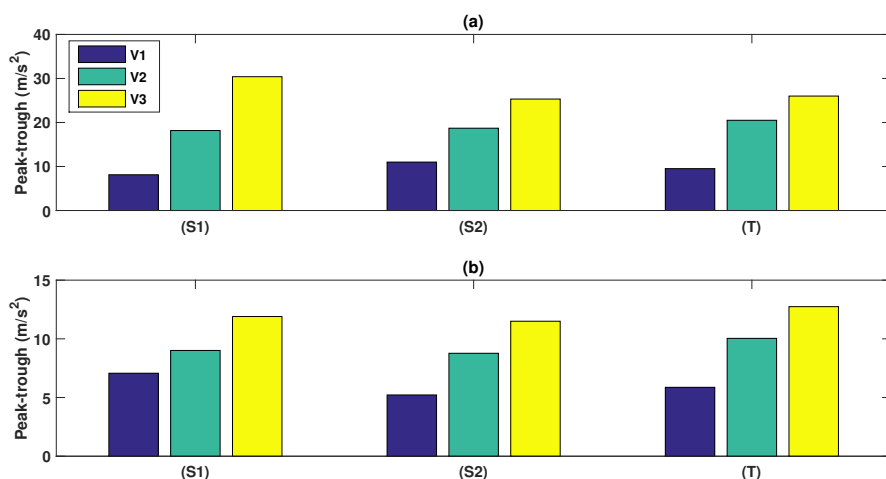


Fig. 6.4 The peak-trough differences of COM vertical acceleration for different walking conditions: (a) experimental data, (b) simulation data.

6.5.3 Hand's 3D acceleration

Normalized profiles of 3D acceleration of the right hand are presented in figure 6.5. When extending the gait cycle definition to the stride, simulation data still show peak acceleration values just after impacts, and minimum values attained during arm swing. A noticeable difference between both models is that in stride-level optimization, the small acceleration peaks during arm swing are smoothed, which gives an acceleration pattern more similar to that found in experimental data. However, 3D acceleration jumps at impact instants are

higher in stride-level optimization than in step-level optimization.

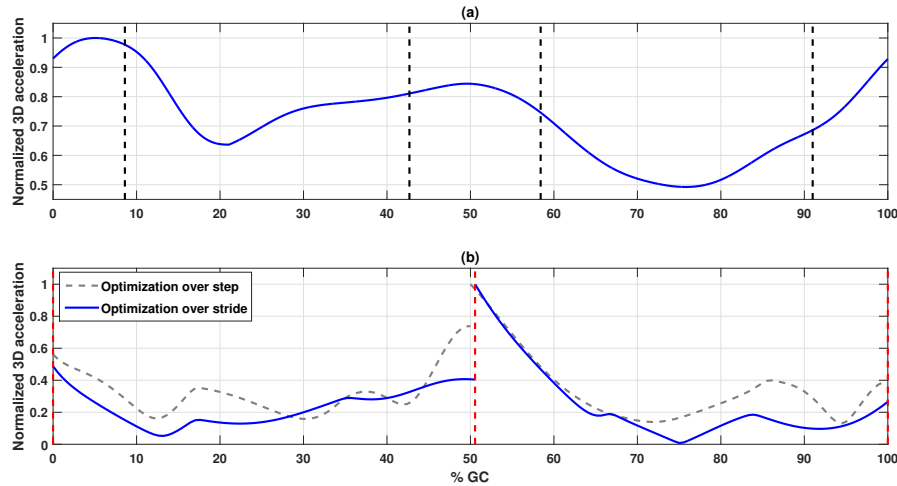


Fig. 6.5 3D acceleration profile of the hand during a GC for the walking condition $V_2/(S1)$: (a) experimental data, (b) simulation data. The black dashed lines indicate DS phases, and red dashed lines indicate impact instants.

RMS values of hand's 3D acceleration for different walking scenarios are shown in figure 6.6. In simulation data, a slight decrease of the RMS value is observed for the mode (S2) compared to (S1) since the additional mass considerably decreases the optimal swing magnitude of the loaded arm during gait cycle. In addition, there is a significant decrease of RMS levels for the mode (T) with respect to swinging modes since the loaded arm configuration is constrained to stabilize the distance between the hand and the head. Both results show that, within the same carrying mode, RMS value increases in function of the gait velocity.

For the carrying mode (S1), the extended 3D simulator provides RMS levels of hand's acceleration higher than in step-level simulator (unloaded swinging). This increase in RMS value is more significant for lower velocity (e.g. 130% and 8% increase for the velocities V_1 and V_3 , respectively).

6.6 Conclusions and contributions to autonomous geolocation

The extended gait cycle definition allows to consider the handheld mass in the skeletal model, and to simulate loaded swinging modes as well as body fixed device carrying modes (e.g. texting mode). Results have shown that, for given stride characteristics and symmetry

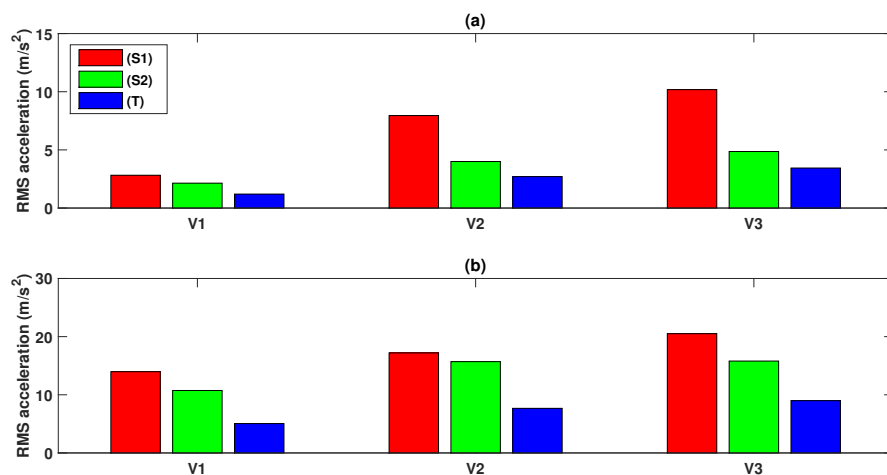


Fig. 6.6 RMS values of hand's 3D acceleration for different walking conditions: (a) experimental data, (b) simulation data.

indexes, the extended simulator allows to observe an asymmetry in acceleration profiles of feet and COM with respect to step-level simulator. Another interesting contribution is that the extended model results in a more energy efficient locomotion movements. Figure 6.7 depicts the variation of the sthenic criterion with walking velocity for different simulation scenarios. We notice a significant decrease of the energy criterion by proceeding to the stride-level optimization. The difference in energy cost between both gait models is expected, since metabolic cost depends on both step length and step frequency [7, 205]. The cost of transport is bigger with short step length than long step length because the hip joint torque consumes more energy for the leg swinging under the situation of fast walking speed and short step length [205], and cost per distance increases approximately with the second power of frequency [7]. This justify the fact that the decrease in sthenic criterion is more remarkable for the comfortable and rapid walking speeds (64% and 76% decrease rates respectively), since for these velocities, lower step length and higher step cadence (with respect to experimental values) are predicted in step-level optimization. Overall, this result supports the observation made by Zarrugh et al. [206] stating that the natural step length at any given walking speed is the one that minimizes energy consumption. The high energy cost observed in the case of step-level optimization is also the result of the implicit constraint of symmetry of walking movement from one step to the next. Although this constraint significantly reduces the number of optimization variables and leads to more rapid convergence, the feasible solution domain of the motion generation problem becomes more restricted. Thus, one can anticipate a higher optimal criterion value.

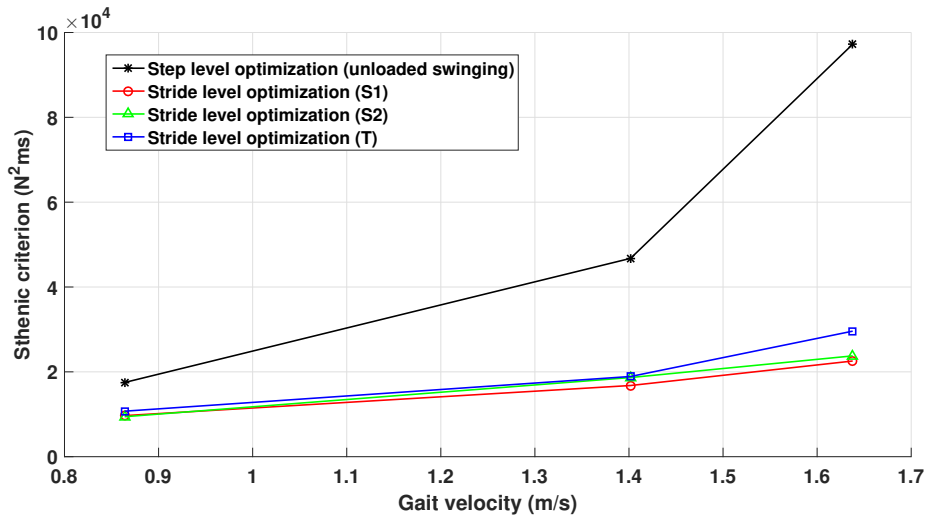


Fig. 6.7 Sthenic criterion versus walking velocity for different simulation scenarios.

Despite the decreased optimal arm swing magnitude, the carrying mode (*S2*) results in a slight increase in sthenic criterion with respect to the mode (*S1*). This indicates the sensitivity of the energy efficiency of the predicted gait motion to a change in the added mass value. This constitutes an improvement with respect to 2D human gait modeling studied in [195], where no remarkable difference in sthenic criterion is observed between unloaded swinging and loaded swinging (with 0.139 kg in hand) scenarios (see appendix G, figure G.1). In addition, the energy cost for texting mode is higher than for swinging modes, as found in the case of planar walking model (cf. figure G.2). This result is consistent with the observation made by Kaddar et al. [207], stating that the lower cost functional in the case of arms swing can be explained by the application of more torques to the arm joints that leads to less important torques in other joints, especially in the stance leg. It also supports the findings of Collins et al. [8] who reported an increase in metabolic cost when human subjects walk in any other way than the natural arm swinging behaviour.

The evaluation of simulation outputs with overground walking data collected with one test subject showed similarities between acceleration profiles related to different body parts. Furthermore, the same variation tendencies of some acceleration items as function of carrying mode and gait velocity are observed for both data. However, the difference in amplitude of the acceleration signals linked to the hand persists, resulting in predicted acceleration features much higher than the experimental values. This issue is inherent to the impulsive nature of the considered impact model and to the discretization scheme of state variables. In fact, in the proposed method, the number of control points for spline functions approximation is the control parameter for the trajectories smoothness in time acting as an implicit con-

straint. There is no general method of determining the minimum number of intermediate time knots required to ensure the feasibility of the optimization problem. Though more control points can increase the smoothness of joint motion and secure the problem feasibility, the computational cost considerably increases with it.

The main objective of this thesis was to develop a realistic walking simulator to generate upper body motion data for given displacement features. The simulator successfully reproduces the kinematic data of human walking for the lower and upper body systems. It also reproduces the same natural evolutions of hand acceleration during single support phases, in swinging mode. The main limitation is the difference in amplitude between simulated and experimental signals, which suggests introducing double support modeling in order to be able to predict acceleration signals over a complete gait cycle, i.e. including finite double support phases, and to avoid significant hand acceleration jumps near impact events. Several improvements were made to our model during this work, in an attempt to get closer to real gait patterns. However, simplifying assumptions in the definition of the walking cycle (e.g. only flat foot contact with the ground) and in the skeletal model (e.g. rigid bodies, frictionless rotations between segments) need to be revisited, and solutions must be considered to limit numerical issues arising from the discretization of state variables and constraints evaluation, and those related to motion optimization performance. These possible enhancements can surely lead to a more reliable modeling framework that will assist in the development of novel autonomous pedestrian geolocation algorithms.

Chapter 7

General conclusion and perspectives

For indoor positioning, PDR is the most used strategy when it comes to estimate pedestrian position from inertial data sensed by handheld devices. In PDR process, step length is estimated using parametric models taking into account some physiological parameters of the user, displacement features and acceleration statistical properties. These models are suitable for the common human gait, and alterations of gait pattern induced by irregular motions lead to increased positioning error at each step. Consequently, frequent adjustment of step length models coefficients is required. This calibration needs large experimental database that characterizes inter/intrasubject variation of human gait parameters. The collection of such a database is costly in terms of time and effort since it should include as many gait-impacting factors as possible, which highly increase the number of measurement trials. In this thesis, we aim to introduce a human gait simulator based on a multibody system in order to provide a simpler way to generate human locomotion database.

We started by reviewing the literature on the various human walking models. This review guided us in the choice of a simulation methodology, leading to a digital human motion prediction framework. We completed our analysis by reporting observations on normal human walking from biomechanical and motion analysis literature. Taking these observations into account, we justified our modeling choices in terms of segments definition and different defined joints DOF of the skeletal model. Inverse dynamics and optimization method were combined by adopting differential inclusion formulation which have smaller number of optimization variables and explicit formulations in terms of variables. In order to allow a realistic prediction of the three-dimensional trajectory of the body segments during walking, several constraints were imposed in the optimization process including limits on joint positions, rates and torques, stability and geometric constraints. Straightforward walking motion is optimized over the step, which is considered as the gait cycle, in such a way as to minimize

the energy dissipated in the actuators per unit of distance. For unloaded swinging mode, step characteristics and joint motions are simultaneously predicted only from the average walking speed.

To evaluate our simulator, simulation outputs were compared with kinematic profiles and accelerometric features obtained from walking experiments. Results showed that the model reproduces similar fundamental patterns of walking and the same variation trend of acceleration related items in function of gait velocity observed in experiments. The main contribution of our model in comparison with previous human walking models is the accuracy of step length estimation. Besides, our model contributes to better estimating hand acceleration feature with respect to planar human gait modeling. However, there is a large difference in hand's acceleration magnitudes between experimental and simulation data. Another noticeable disparity is that experimental acceleration patterns related to feet and COM have shown different profiles for each single support phase. This observation suggests that asymmetric movements that are likely to result in a step-level asymmetry of displacement features occurred. Therefore, we investigated the temporal aspect of this asymmetry to find out whether the asymmetry level of gait cycle during steady walking, probably caused by handling a mass in hand, is significant in the context of pedestrian navigation solution.

The impact of the handheld mass on the walking gait was studied with experimental data collected with 10 test participants and a 0.19 kg handheld device in a motion capture laboratory. It was shown that the presence of a mass in hand or a constrained arm configuration alters the gait symmetry at the step level. The outcome of this research showed that the assumption of identical steps is a source of significant error in the computation of the cumulative traveled distance which led us to extend the definition of gait cycle to the stride. This extension involves modifications on optimization variables, as well as constraints and cost functions definition. For loaded swinging and texting scenarios, gait motions over a stride are predicted for average gait velocity, stride characteristics (length, width), and step-level symmetry indexes. The last two descriptors have been added compared to the previous model to specify the characteristics of the steps and to simulate the acceleration of the hand resulting from the induced movement of the loaded arm. Results have shown that the extended simulator allows to observe an asymmetry in acceleration profiles of feet and COM with respect to step-level simulator. Another interesting contribution is that the extended model results in a more energy efficient locomotion movements. The evaluation of simulation outputs with overground walking data collected with one test subject showed similarities between acceleration profiles related to different body parts. Furthermore, the

same variation tendencies of some acceleration items as function of carrying mode and gait velocity are observed for both data. However, the difference in amplitude of the acceleration signals linked to the hand persists.

In conclusion, we have proposed a new tool to generate human locomotion data in order to avoid costly experimental data collection. The current modeling framework partially solves for the direct modeling problem of pedestrian navigation. Predicting the acceleration features of the hand for given displacement features remains challenging given the simplifying assumptions of the involved robotic tools. Further enhancements on the current simulator are required to achieve the prediction of gaits constituting human locomotion with a high degree of confidence. Such a model might then be a valuable tool to viably assist in the development of novel autonomous pedestrian geolocation algorithms.

Overall, this research shows that combining the three research areas, i.e. robotics, biomechanics and pedestrian navigation, is a very interesting way of addressing the challenges related to the increase of individual's autonomy using everyday objects.

A first research perspective will be to introduce the double support phase in the gait cycle definition in order to obtain shapes and amplitudes of acceleration profiles closer to those of real walking. In addition, including the phase where the stance heel rises from the ground and the support foot rotates about the toe is a potential enhancement of gait cycle definition. In fact, Tlalolini et al. [208] revealed that this under-actuated phase is useful to reduce the criteria cost for fast motions.

Regarding the motion optimization performance, variable block optimization mentioned in section 6.3 is an efficient strategy which can be adopted to avoid the “overfitting” phenomenon, which means that some variables change too much but others change only a little from their initial values. However, the smallest possible number of iterations should be considered to limit the computation time. To improve the convergence of the optimization algorithm, gradient-based optimization methods can be used to find optimal solutions by iteratively considering cost/constraint function values and their gradients with respect to optimization variables [14, 209].

To solve for numerical issues arising from the discretization of state variables, we can increase the number of time knots for interpolation of joints histories. However, the main drawback of this solution is that it considerably expands the optimization problem size. An alternative solution is to optimize the control points for approximation functions along with intermediate time intervals durations like in the work of Kim et al. [14]. This means that the interpolation points are no longer uniformly distributed over the swinging phase time interval, instead their

times are the result of optimization process. Such an alternative widens the feasible solution domain since it diminishes the possible conflict of the implicit constraint of smoothness in time with the explicit optimization constraints.

Finally, validation with experimental data of several subjects is also targeted in order to qualify the framework's capability of coping with inter-subject variability of gait pattern.

References

- [1] C. Combettes. *Estimation de la direction de marche à partir de capteurs inertiels et magnétiques portés dans la main*. PhD thesis, Université de Nantes, France, 2016.
- [2] M. Abid, V. Renaudin, Y. Aoustin, E. Le-Carpentier, and T. Robert. Walking gait step length asymmetry induced by handheld device. *IEEE Transactions on Neural Systems and Rehabilitation Engineering*, 25(11):2075–2083, Nov. 2017.
- [3] Q. Zhao, B. Zhang, J. Wang, W. Feng, W. Jia, and M. Sun. Improved method of step length estimation based on inverted pendulum model. *International Journal of Distributed Sensor Networks*, 13(4):1550147717702914, 2017.
- [4] V.T. Inman, H.J. Ralston, and F. Todd. *Human Walking*. Baltimore, MD: Williams and Wilkins Company, 1981.
- [5] S. Mochon and T.A. McMahon. Ballistic walking. *Journal of Biomechanics*, 13(1):49–57, 1980.
- [6] T. McGeer. Passive dynamic walking. *Int. J. Rob. Res.*, 9(2):62–82, 1990.
- [7] A. Kuo. A simple model of bipedal walking predicts the preferred speed–step length relationship. *Journal of biomechanical engineering*, 123:264–269, Jul. 2001.
- [8] S.H. Collins, P.G. Adamczyk, and A.D. Kuo. Dynamic arm swinging in human walking. *Proceedings of the Royal Society B: Biological Sciences*, 276(1673):3679–3688, 2009.
- [9] B. Kaddar, Y. Aoustin, and C. Chevallereau. Arm swing effects on walking bipedal gaits composed of impact, single and double support phases. *Robotics and Autonomous Systems*, 66:104–115, 2015.
- [10] J. Perry and J.M. Burnfield. *Gait Analysis: Normal and Pathological Function*. SLACK, 2010.
- [11] W. Khalil and J. Kleinfinger. A new geometric notation for open and closed-loop robots. *Proceedings. 1986 IEEE International Conference on Robotics and Automation*, 3:1174–1179, Apr 1986.
- [12] E. Dombre and W. Khalil. *Robot Manipulators: Modeling, Performance Analysis and Control*. ISTE. Wiley, 2013.
- [13] M. Vukobratovic and B. Borovac. Zero-moment point - thirty five years of its life. *Int. J. of Humanoid Robotics*, 1:157–173, Mar. 2004.

- [14] H.J. Kim, Q. Wang, S. Rahmatalla, C.C. Swan, J.S. Arora, K. Abdel-Malek, and J.G. Assouline. Dynamic motion planning of 3D human locomotion using gradient-based optimization. *Journal of biomechanical engineering*, 130(3):031002, 2008.
- [15] Q. Wang, Y. Xiang, H.J. Kim, J. Arora, and K. Abdel-Malek. Alternative formulations for optimization-based-digital human motion prediction. *SAE Technical Papers*, Jun. 2005.
- [16] M. Romanovas, V. Goridko, A. Al-Jawad, M. Schwaab, M. Traechtler, L. Klingbeil, and Y. Manoli. A study on indoor pedestrian localization algorithms with foot-mounted sensors. In *2012 International Conference on Indoor Positioning and Indoor Navigation (IPIN)*, pages 1–10, Nov. 2012.
- [17] Y. Li, Y. Zhuang, P. Zhang, H. Lan, X. Niu, and N. El-Sheimy. An improved inertial/wifi/magnetic fusion structure for indoor navigation. *Information Fusion*, 34:101–119, 2017.
- [18] E.K. Neil, C.N. William, R.O. Wayne, P.R. John, T. Andy, S. Paul, V.B. Joseph, C.H. Stephen, and W.H. Engelmann. The national human activity pattern survey (nhaps): a resource for assessing exposure to environmental pollutants. *Journal of Exposure Analysis and Environmental Epidemiology*, 11:231–252, 2001.
- [19] M.F. Mokbel and J.J. Levandoski. Toward context and preference-aware location-based services. In *Proceedings of the Eighth ACM International Workshop on Data Engineering for Wireless and Mobile Access, MobiDE '09*, pages 25–32, New York, NY, USA, 2009. ACM.
- [20] V. Renaudin, M. Susi, and G. Lachapelle. Step length estimation using handheld inertial sensors. *Sensors*, 12(7):8507–8525, Jun. 2012.
- [21] M. Susi. *Gait analysis for pedestrian navigation using MEMS handheld devices*. PhD thesis, University of Calgary, Canada, 2012.
- [22] J. Jahn, U. Batzer, J. Seitz, and J.G. Boronat. Comparison and evaluation of acceleration based step length estimators for handheld devices. *International Conference on Indoor Positioning and Indoor Navigation (IPIN)*, pages 1–6, 2010.
- [23] D. Titterton, J.L. Weston, J. Weston, Institution of Electrical Engineers, American Institute of Aeronautics, and Astronautics. *Strapdown Inertial Navigation Technology*. Electromagnetics and Radar Series. Institution of Engineering and Technology, 2004.
- [24] I. Skog, P. Handel, J.O. Nilsson, and J. Rantakokko. Zero-velocity detection - an algorithm evaluation. *IEEE Transactions on Biomedical Engineering*, 57(11):2657–2666, Nov 2010.
- [25] A.R. Jimenez, F. Seco, C. Prieto, and J. Guevara. A comparison of pedestrian dead-reckoning algorithms using a low-cost MEMS IMU. In *2009 IEEE International Symposium on Intelligent Signal Processing*, pages 37–42, Aug. 2009.
- [26] S.H. Shin, C.G. Park, J.W. Kim, H.S. Hong, and J.M. Lee. Adaptive step length estimation algorithm using low-cost MEMS inertial sensors. In *2007 IEEE Sensors Applications Symposium*, pages 1–5, Feb. 2007.

- [27] V. Renaudin, O. Yalak, and P. Tomé. Indoor navigation of emergency agents. *European Journal of Navigation*, pages 36–45, 2007.
- [28] D. Alvarez, R.C. Gonzalez, A. Lopez, and J.C. Alvarez. Comparison of step length estimators from wearable accelerometer devices. In *2006 International Conference of the IEEE Engineering in Medicine and Biology Society*, pages 5964–5967, Aug. 2006.
- [29] J. Kim, H. Jang, D. Hwang, and C. Park. A step, stride and heading determination for the pedestrian navigation system. *Positioning*, 1(8), 2004.
- [30] W. Zijlstra and A.L. Hof. Displacement of the pelvis during human walking: experimental data and model predictions. *Gait & Posture*, 6(3):249–262, 1997.
- [31] Z.L. Sun, X.C. Mao, and W.F. Tian. Pedestrian dead reckoning based on activity recognition and stride assessment. *J. Shanghai Jiaotong Univ.*, 42:2002–2005, 2008.
- [32] U. Steinhoff and B. Schiele. Dead reckoning from the pocket - an experimental study. In *2010 IEEE International Conference on Pervasive Computing and Communications (PerCom)*, pages 162–170, Mar. 2010.
- [33] D. Gusenbauer, C. Isert, and J. Krösche. Self-contained indoor positioning on off-the-shelf mobile devices. In *2010 International Conference on Indoor Positioning and Indoor Navigation*, pages 1–9, Sep. 2010.
- [34] M. Susi, V. Renaudin, and G. Lachapelle. Motion mode recognition and step detection algorithms for mobile phone users. In *Sensors*, 2013.
- [35] L. Cohen. *Time-frequency Analysis: Theory and Applications*. Prentice-Hall, Inc., Upper Saddle River, NJ, USA, 1995.
- [36] S. Donker, P. Beek, R. Wagenaar, and T. Mulder. Coordination between arm and leg movements during locomotion. *Journal of motor behavior*, 33:86–102, Apr. 2001.
- [37] S. Yang and Q. Li. Ambulatory walking speed estimation under different step lengths and frequencies. In *2010 IEEE/ASME International Conference on Advanced Intelligent Mechatronics*, pages 658–663, Jul. 2010.
- [38] H. Xing, J. Li, B. Hou, Y. Zhang, and M. Guo. Pedestrian stride length estimation from IMU measurements and ANN based algorithm. *Journal of Sensors*, 2017, 10 pages, 2017.
- [39] S. Sprager and M.B. Juric. Inertial sensor-based gait recognition: A review. *Sensors*, 15(9):22089–22127, 2015.
- [40] J. Frank, S. Mannor, J. Pineau, and D. Precup. Time series analysis using geometric template matching. *IEEE Trans. Pattern Anal. Mach. Intell.*, 35(3):740–754, March 2013.
- [41] Y. Ren, Y. Chen, M.C. Chuah, and J. Yang. User verification leveraging gait recognition for smartphone enabled mobile healthcare systems. *IEEE Transactions on Mobile Computing*, 14(9):1961–1974, Sept. 2015.

- [42] F.E. Zajac, R.R. Neptune, and S.A. Kautz. Biomechanics and muscle coordination of human walking: Part ii: Lessons from dynamical simulations and clinical implications. *Gait & Posture*, 17(1):1–17, 2003.
- [43] N.B. Alexander, J.M. Mollo, B. Giordani, J.A. Ashton-Miller, A.B. Schultz, J.A. Grunawalt, and N.L. Foster. Maintenance of balance, gait patterns, and obstacle clearance in alzheimer's disease. *Neurology*, 45(5):908–914, 1995.
- [44] G. Cavagna, H. Thys, and A. Zamboni. The sources of external work in level walking and running. *The Journal of physiology*, 262:639–657, Dec. 1976.
- [45] R. Alexander. Energy-saving mechanisms in walking and running. *The Journal of experimental biology*, 160:55–69, Nov. 1991.
- [46] R.McN. Alexander. A model of bipedal locomotion on compliant legs. *Philosophical transactions of the Royal Society of London. Series B, Biological sciences*, 338:189–198, Nov. 1992.
- [47] C. Lee and C. Farley. Determinants of the center of mass trajectory in human walking and running. *The Journal of experimental biology*, 201:2935–2944, Dec. 1998.
- [48] M. García, A. Chatterjee, A. Ruina, and M. Coleman. The simplest walking model: stability, complexity, and scaling. *Journal of biomechanical engineering*, 120 2:281–8, 1998.
- [49] R.C. Gonzalez, D. Alvarez, A. Lopez, and J. Alvarez. Modified pendulum model for mean step length estimation. In *Proceedings of the 29th annual international conference of the IEEE Engineering in Medicine and Biology Society (EMBS 2007)*, Lyon, France, volume 2007, pages 1371–1374, Aug. 2007.
- [50] V. Renaudin. *Hybridation MEMS/UWB pour la navigation pédestre intra-muros*. PhD thesis, École Polytechnique Fédérale de Lausanne (EPFL), Lausanne, Switzerland, 2009.
- [51] S. Miyazaki. Long-term unrestrained measurement of stride length and walking velocity utilizing a piezoelectric gyroscope. *IEEE Transactions on Biomedical Engineering*, 44(8):753–759, Aug. 1997.
- [52] C.K. Chow and D.H. Jacobson. Studies of human locomotion via optimal programming. *Mathematical Biosciences*, 10(3):239–306, 1971.
- [53] J.B.d.M. Saunders, T.V. Inman, and H.D. Eberhart. Major determinants in normal and pathological gait. *J Bone Joint Surg*, 35-A(12):543–557, Aug. 1953.
- [54] S.H. Collins and A. Ruina. A bipedal walking robot with efficient and human-like gait. In *Proceedings of the 2005 IEEE International Conference on Robotics and Automation*, pages 1983–1988, Apr. 2005.
- [55] D.W. Grieve and R.J. Gear. The relationships between length of stride, step frequency, time of swing and speed of walking for children and adults. *Ergonomics*, 9:379–399, Oct. 1966.

- [56] P. DeVita. The selection of a standard convention for analyzing gait data based on the analysis of relevant biomechanical factors. *Journal of biomechanics*, 27:501–508, Mai 1994.
- [57] D.A. Winter. Biomechanical motor patterns in normal walking. *Journal of motor behavior*, 15:302–330, Jan. 1984.
- [58] D.A. Winter, A.E. Patla, J. Frank, and S.E. Walt. Biomechanical walking pattern changes in the fit and elderly. *Physical therapy*, 70:340–347, Jul. 1990.
- [59] J.V. Basmajian and C.J. De Luca. *Muscles Alive: Their Functions Revealed by Electromyography*. Williams & Wilkins, 1985.
- [60] R.D. Crowninshield and R.A. Brand. A physiologically based criterion of muscle force prediction in locomotion. *Journal of Biomechanics*, 14(11):793–801, 1981.
- [61] K.G. Holt, J. Hamill, and R.O. Andres. The force-driven harmonic oscillator as a model for human locomotion. *Human Movement Science*, 9(1):55–68, 1990.
- [62] D. Mena, J.M. Mansour, and S.R. Simon. Analysis and synthesis of human swing leg motion during gait and its clinical applications. *Journal of Biomechanics*, 14(12):823–832, 1981.
- [63] A. Kuo. Stabilization of lateral motion in passive dynamic walking. *The International Journal of Robotics Research*, 18, Sep. 1999.
- [64] A. Kuo. Energetics of actively powered locomotion using the simplest walking model. *Journal of biomechanical engineering*, 124:113–120, Mar. 2002.
- [65] R. van der Linde. Passive bipedal walking with phasic muscle contraction. *Biological cybernetics*, 81:227–237, Oct. 1999.
- [66] C. Bauby and A. Kuo. Active control of lateral balance in human walking. *Journal of biomechanics*, 33:1433–1440, Dec. 2000.
- [67] M. Pandy and N. Berme. A numerical method for simulating the dynamics of human walking. *Journal of Biomechanics*, 21(12):1043–1051, 1988.
- [68] M. Pandy and N. Berme. Quantitative assessment of gait determinants during single stance via a three-dimensional model—part 2. pathological gait. *Journal of Biomechanics*, 22(6):725–733, 1989.
- [69] S. Siegler, R. Seliktar, and W. Hyman. Simulation of human gait with the aid of a simple mechanical model. *Journal of Biomechanics*, 15(6):415 – 425, 1982.
- [70] M. Pandy. Simple and complex models for studying muscle function in walking. *Philosophical Transactions of the Royal Society of London B: Biological Sciences*, 358(1437):1501–1509, 2003.
- [71] Effects of restricted knee flexion and walking speed on the vertical ground reaction force during gait.

- [72] T. Fukunaga, K. Kubo, Y. Kawakami, S. Fukashiro, H. Kanehisa, and C.N. Maganaris. In vivo behaviour of human muscle tendon during walking. *Proceedings of the Royal Society of London B: Biological Sciences*, 268(1464):229–233, 2001.
- [73] G.T. Rab. Application of three-dimensional gait data to skeletal modeling. *Gait & Posture*, 2(1):55, 1994.
- [74] A.E. Minetti and R. Alexander. A theory of metabolic costs for bipedal gaits. *Journal of Theoretical Biology*, 186(4):467–476, 1997.
- [75] A. Minetti, C. Capelli, P. Zamparo, P.E. Di Prampero, and F. Saibene. Effects of stride frequency on mechanical power and energy expenditure of walking. *Medicine and science in sports and exercise*, 27:1194–1202, Sep. 1995.
- [76] V. Zatsiorsky. *Kinetics of Human Motion*. 01 2002.
- [77] A.D. Kuo. The six determinants of gait and the inverted pendulum analogy: A dynamic walking perspective. *Human movement science*, 26:617–656, Sep. 2007.
- [78] J. Rose and J.G. Gamble. *Human Walking*. LWW medical book collection. Lippincott Williams & Wilkins, 2006.
- [79] H.B. Skinner. *Current Diagnosis & Treatment in Orthopedics*. AccessLANGE clinical reference series. Lange Medical Books, 2003.
- [80] J. Furusho and M. Masubichi. Control of a dynamical biped locomotion system for steady walking. *Journal of Dynamic Systems Measurement and Control*, 108:111–118, Jun. 1986.
- [81] J.J. Faraway, X. Zhang, and D. Chaffin. Rectifying postures reconstructed from joint angles to meet constraints. *Journal of biomechanics*, 32(7):7333–7736, Aug. 1999.
- [82] C. Azevedo, P. Poinet, and B. Espiau. Moving horizon control for biped robots without reference trajectory. In *Proceedings of the 2002 IEEE, International Conference on Robotics & Automation*, 2002.
- [83] J. Kuffner, J. James, S. Kagami, K. Nishiwaki, M. Inaba, and H. Inoue. Dynamically-stable motion planning for humanoid robots. *Autonomous Robots*, 12(1):105–118, Jan. 2002.
- [84] C. Chevallereau and Y. Aoustin. Optimal reference trajectories for walking and running of a biped robot. *Robotica*, 19(5):557–569, August 2001.
- [85] T. Saidouni and G. Bessonnet. Generating globally optimised sagittal gait cycles of a biped robot. *Robotica*, 21(2):199–210, 2003.
- [86] C. Chevallereau, A. Formal'sky, and B. Perrin. Low energy cost reference trajectories for a biped robot. In *Proceedings of IEEE International Conference on Robotics and Automation*, volume 2, pages 1398–1404, May 1998.
- [87] L. Roussel, C. Canudas-De-Wit, and A. Goswami. Generation of energy optimal complete gait cycles for biped robots. In *Proceedings of IEEE International Conference on Robotics and Automation*, volume 3, pages 2036–2041, May 1998.

- [88] F. Anderson and M.G. Pandy. Dynamic optimization of human walking. *Journal of biomechanical engineering*, 123:381–390, Nov. 2001.
- [89] M.G. Pandy, F. Anderson, and D.G. Hull. A parameter optimization approach for the optimal control of large-scale musculoskeletal systems. *Journal of biomechanical engineering*, 114:450–460, Dec. 1992.
- [90] M.G. Pandy. Computer modeling and simulation of human movement. *Annual review of biomedical engineering*, 3:245–273, Feb. 2001.
- [91] R.N. Marshall, G.A. Wood, and L.S. Jennings. Performance objectives in human movement: A review and application to the stance phase of normal walking. *Human Movement Science*, 8(6):571–594, 1989.
- [92] C. Y. E. Wang, J. E. Bobrow, and D. J. Reinkensmeyer. Swinging from the hip: use of dynamic motion optimization in the design of robotic gait rehabilitation. In *Proceedings of IEEE International Conference on Robotics and Automation*, volume 2, pages 1433–1438, 2001.
- [93] G. Bessonnet, P. Sardain, and S. Chessé. Optimal motion synthesis – dynamic modelling and numerical solving aspects. *Multibody System Dynamics*, 8:257–278, Oct. 2002.
- [94] L. Ren, R.K. Jones, and D. Howard. Predictive modelling of human walking over a complete gait cycle. *Journal of Biomechanics*, 40(7):1567–1574, 2007.
- [95] B. Koopman, H.J. Grootenboer, and H.J. de Jongh. An inverse dynamics model for the analysis, reconstruction and prediction of bipedal walking. *Journal of biomechanics*, 28:1369–1376, Dec. 1995.
- [96] J. Lo, G. Huang, and D. Metaxas. Human motion prediction based on recursive dynamics and optimal control techniques. *Multibody System Dynamics*, 8:433–458, 2002.
- [97] G.T. Yamaguchi and F.E. Zajac. Restoring unassisted natural gait to paraplegics via functional neuromuscular stimulation: a computer simulation study. *IEEE Transactions on Biomedical Engineering*, 37:886–902, 1990.
- [98] M. Silva and J. Ambrósio. Sensitivity of the results produced by the inverse dynamic analysis of a human stride to perturbed input data. *Gait & Posture*, 19(1):35–49, 2004.
- [99] J. Hanavan. A mathematical model of the human body. *AMRL Technical Report*, 18:158, Oct. 1964.
- [100] H. Hatze. A mathematical model for the computational determination of parameter values of anthropomorphic segments. *Journal of Biomechanics*, 13(10):833–843, 1980.
- [101] M.R. Yeadon. The simulation of aerial movement—ii. a mathematical inertia model of the human body. *Journal of Biomechanics*, 23(1):67–74, 1990.

- [102] F. Leboeuf. *Contribution a l'analyse dynamique et à la synthèse dynamique du mouvement humain*. PhD thesis, Jan. 2004.
- [103] W.T. Dempster. Space requirements of the seated operator: geometrical, kinematic, and mechanical aspects of the body, with special reference to the limbs. *Wright Air Development Center Technical Report*, 55–159, Jan. 1956.
- [104] J.T. McConville, T.D. Churchill, I. Kaleps, C.E. Clauser, and J. Cuzzi. Anthropometric relationships of body and body segment moments of inertia. Technical report, 1980.
- [105] J.W. Young, R.F. Chandler, C.C. Snow, K.M. Robinette, G.F. Zehner, and M.S. Lofberg. Anthropometric and mass distribution characteristics of the adults female. Technical report, 1983.
- [106] V. Zatsiorsky and V.N. Seluyanov. The mass and inertia characteristics of the main segment of human body. *Biomechanics VIII: Proceedings of the eighth international congress of biomechanics*. Human Kinetics Publishers Champaign Il, 4, Dec. 1982.
- [107] D. Pearsall and J.G. Reid. The study of human body segment parameters in biomechanics. *Sports Medicine*, 18:126–140, Aug. 1994.
- [108] R. Dumas, L. Chèze, and J.-P. Verriest. Adjustments to mcconville et al. and young et al. body segment inertial parameters. *Journal of Biomechanics*, 40(3):543–553, 2007.
- [109] K. Abdel-Malek, W. Yu, M. Jaber, and J. Duncan. Realistic posture prediction for maximum dexterity. *SAE Technical Papers*, Jun. 2001.
- [110] J. Yang, R.T. Marler, H. Kim, J. Arora, and K. Abdel-Malek. Multi-objective optimization for upper body posture prediction. In *10th AIAA/ISSMO Multidisciplinary Analysis and Optimization Conf. Albany, NY.*, Aug. 2004.
- [111] Z. Mi. *Task-based prediction of upper body motion*. PhD thesis, Department of Mechanical Engineering, University of Iowa, Iowa City, IA 52242., Jul. 2004.
- [112] R.T. Marler. Development of real-time multiobjective optimization-based posture prediction. *Technical Report No. VSR-04.02. Virtual Soldier Research program/CCAD, The University of Iowa, Iowa City, IA 52242.*, 2004.
- [113] A.E. Bryson and Y.C. Ho. *Applied Optimal Control*. New York: Hemishper Publishing, 1975.
- [114] M.G. Pandy, B.A. Garner, and F. Anderson. Optimal control of non-ballistic muscular movements: A constraint-based performance criterion for rising from a chair. *Journal of biomechanical engineering*, 117:15–26, Mar. 1995.
- [115] F. De Groote, A.L. Kinney, A.V. Rao, and B.J. Fregly. Evaluation of direct collocation optimal control problem formulations for solving the muscle redundancy problem. *Annals of Biomedical Engineering*, 44(10):2922–2936, Oct. 2016.
- [116] M.L. Kaplan and J.H. Heegaard. Predictive algorithms for neuromuscular control of human locomotion. *Journal of Biomechanics*, 34(8):1077–1083, 2001.

- [117] M.L. Kaplan and J.H. Heegaard. Second-order optimal control algorithm for complex systems. *International Journal for Numerical Methods in Engineering*, 53(9):2043–2060, 2002.
- [118] J.T. Betts. A survey of numerical methods for trajectory optimization. *J. Guidance, Cont. Dyn.*, 21(2):193–207, 1998.
- [119] D.G. Hull. *Optimal Control Theory for Applications*. Mechanical Engineering Series. Springer New York, 2003.
- [120] C.H. Tseng and J.S. Arora. Optimum design of systems for dynamics and controls using sequential quadratic programming. *AIAA J.*, 27:1793–1800, 1989.
- [121] H. Seywald. Trajectory optimization based on differential inclusion. *J. Guidance, Cont. Dyn.*, 17(3):480–487, 1994.
- [122] J.S. Arora. Optimization of structures subjected to dynamic loads. In *Leondes, C.T. (ed.) Structural Dynamic Systems Computational Techniques and Optimization: Optimization Techniques*, pages 1–72. The Netherlands: Gordon and Breach Science Publishers, 1999.
- [123] C.C. Hsieh and J.S. Arora. Design sensitivity analysis and optimization of dynamic response. *Computer Methods in Applied Mechanics and Engineering*, 43(2):195–219, 1984.
- [124] V. Schulz. Simultaneous solution approaches for large optimization problems. *Journal of Computational and Applied Mathematics*, 164(1):629–641, 2004.
- [125] A.M. Cervantes, A. Wächter, R.H. Tütüncü, and L.T. Biegler. A reduced space interior point strategy for optimization of differential algebraic systems. *Computers & Chemical Engineering*, 24(1):39–51, 2000.
- [126] H. Pontzer, J.H. Holloway, D. Raichlen, and D. Lieberman. Control and function of arm swing in human walking and running. *The Journal of experimental biology*, 212:523–534, Mar. 2009.
- [127] M. Kubo, R.C. Wagenaar, E. Saltzman, and K.G. Holt. Biomechanical mechanism for transitions in phase and frequency of arm and leg swing during walking. *Biological Cybernetics*, 91(2):91–98, Aug. 2004.
- [128] K.M. Jackson, J. Joseph, and S.J. Wyard. The upper limbs during human walking. ii. function. *Electromyography and clinical neurophysiology*, 23:435–446, Sep. 1983.
- [129] S.N. Whittlesey, R.E.A. van Emmerik, and J. Hamill. The swing phase of human walking is not a passive movement. *Motor Control*, 4(3):273–292, 2000.
- [130] H. Elftman. The functions of the arms in walking. *Hum Biol*, 11:529–536, 1939.
- [131] K.M. Jackson, J. Joseph, and S.J. Wyard. A mathematical model of arm swing during human locomotion. *Journal of Biomechanics*, 11(6):277 – 289, 1978.
- [132] R.N. Hinrichs. *Whole Body Movement: Coordination of Arms and Legs in Walking and Running*, pages 694–705. Springer New York, New York, NY, 1990.

- [133] M.L. Fernandez-Ballesteros, F. Buchthal, and P. Rosenfalck. The pattern of muscular activity during the arm swing of natural walking. *Acta Physiologica Scandinavica*, 63(3):296–310, 1965.
- [134] B.R. Umberger. Effects of suppressing arm swing on kinematics, kinetics, and energetics of human walking. *Journal of Biomechanics*, 41(11):2575–2580, 2008.
- [135] H. Herr and M. Popovic. Angular momentum in human walking. *Journal of Experimental Biology*, 211(4):467–481, 2008.
- [136] H. Witte, H. Preuschoft, and S. Recknagel. Human body proportions explained on the basis of biomechanical principles. *Z. Morph. Anthropol.*, 78(3):407–423, 1991.
- [137] Y. Li, W. Wang, R.H. Crompton, and M.M. Gunther. Free vertical moments and transverse forces in human walking and their role in relation to arm-swing. *Journal of Experimental Biology*, 204(1):47–58, 2001.
- [138] J.D. Ortega, L.A. Fehlman, and C.T. Farley. Effects of aging and arm swing on the metabolic cost of stability in human walking. *Journal of biomechanics*, 41(16), 2008.
- [139] Y. Aoustin and A.M. Formalskii. 3d walking biped: optimal swing of the arms. *Multibody System Dynamics*, 32(1):55–66, Jun. 2014.
- [140] B. Zhang, S. Jiang, D. Wei, M. Marschollek, and W. Zhang. State of the art in gait analysis using wearable sensors for healthcare applications. In *2012 IEEE/ACIS 11th International Conference on Computer and Information Science*, pages 213–218, May 2012.
- [141] N.F. Ribeiro and C.P. Santos. Inertial measurement units: A brief state of the art on gait analysis. In *2017 IEEE 5th Portuguese Meeting on Bioengineering (ENBENG)*, pages 1–4, Feb. 2017.
- [142] T. Liu, Y. Inoue, and K. Shibata. Development of a wearable sensor system for quantitative gait analysis. *Measurement*, 42(7):978–988, 2009.
- [143] S. Tadano, R. Takeda, and H. Miyagawa. Three dimensional gait analysis using wearable acceleration and gyro sensors based on quaternion calculations. *Sensors*, 13(7):9321–9343, 2013.
- [144] Simone Theresa Boerema, Lex Stefan van Velsen, Leendert Schaake, Thijs Tönis, and Hermanus J. Hermens. Optimal sensor placement for measuring physical activity with a 3D accelerometer. *Sensors*, 14(2):3188–3206, 2014.
- [145] F. Sposaro and G. Tyson. ifall: An android application for fall monitoring and response. In *2009 Annual International Conference of the IEEE Engineering in Medicine and Biology Society*, pages 6119–6122, Sept 2009.
- [146] S. Yang and Q. Li. Inertial sensor-based methods in walking speed estimation: A systematic review. *Sensors*, 12(5):6102–6116, 2012.
- [147] Q. Li and J.T. Zhang. Post-trial anatomical frame alignment procedure for comparison of 3d joint angle measurement from magnetic/inertial measurement units and camera-based systems. *Physiol. Meas.*, 35(11):2255–2268, 2014.

- [148] A.M. Sabatini, C. Martelloni, S. Scapellato, and F. Cavallo. Assessment of walking features from foot inertial sensing. *IEEE Transactions on Biomedical Engineering*, 52(3):486–494, March 2005.
- [149] P.D. Groves. *Principles of GNSS, Inertial, and Multisensor Integrated Navigation Systems, Second Edition*. Artech House, Mar. 2013.
- [150] Tao Liu, Yoshio Inoue, and Kyoko Shibata. A wearable force plate system designed using small triaxial force sensors and inertial sensors. *Adv. in Biomedical Sensing, LNEE 55*, pages 61–73, 2010.
- [151] Hylton Menz, Stephen Lord, and Richard C Fitzpatrick. Acceleration patterns of the head and pelvis when walking on level and irregular surfaces. *Gait & Posture*, 18:35–46, Sept 2003.
- [152] H. Ghasemzadeh, R. Jafari, and B. Prabhakaran. A body sensor network with electromyogram and inertial sensors: Multimodal interpretation of muscular activities. *IEEE Transactions on Information Technology in Biomedicine*, 14(2):198–206, March 2010.
- [153] Miguel Ortiz, Mathieu De Sousa, and Valérie Renaudin. A new PDR navigation device for challenging urban environments. *Journal of Sensors*, 2017:1–11, 2017.
- [154] J. Le Scornec, M. Ortiz, and V. Renaudin. Foot-mounted pedestrian navigation reference with tightly coupled gnss carrier phases, inertial and magnetic data. In *2017 International Conference on Indoor Positioning and Indoor Navigation (IPIN)*, pages 1–8, Sept 2017.
- [155] V. Renaudin and C. Combettes. Magnetic, acceleration fields and gyroscope quaternion (MAGYQ)-based attitude estimation with smartphone sensors for indoor pedestrian navigation. *Sensors*, 14(12):22864–22890, 2014.
- [156] H. Skutkova, M. Vitek, K. Sedlar, and I. Provaznik. Progressive alignment of genomic signals by multiple dynamic time warping. *Journal of Theoretical Biology*, 385:20–30, 2015.
- [157] S. Kumar, V. Renaudin, Y. Aoustin, E. Le-Carpentier, and C. Combettes. Model-based and experimental analysis of the symmetry in human walking in different device carrying modes. In *2016 6th IEEE International Conference on Biomedical Robotics and Biomechatronics (BioRob)*, pages 1172–1179, Jun. 2016.
- [158] R. Baker. Temporal spatial data, the gait cycle and gait graphs.
- [159] W.B. Greene, J.D. Heckman, and American Academy of Orthopaedic Surgeons. *The Clinical Measurement of Joint Motion*. American Academy of Orthopaedic Surgeons, 1994.
- [160] K. Cerny, J. Perry, and J.M. Walker. Effect of an unrestricted knee-ankle-foot orthosis on the stance phase of gait in healthy persons. *Orthopedics*, 13(10):1121–1127, October 1990.

- [161] M.J. Mueller, S.D. Minor, J.A. Schaaf, M. Strube, and S. Sahrman. Relationship of relationship of plantar-flexor peak torque and dorsiflexion range of motion to kinetic variables during walking. *Physical therapy*, 75:684–693, Sep. 1995.
- [162] S. Nadeau, D. Gravel, A.B. Arsenaault, and D. Bourbonnais. Plantarflexor weakness as a limiting factor of gait speed in stroke subjects and the compensating role of hip flexors. *Clinical biomechanics (Bristol, Avon)*, 14:125–135, Feb. 1999.
- [163] K. Horsman. *The Twente lower extremity model. Consistent dynamic simulation of the human locomotor apparatus*. PhD thesis, University of Twente, Netherlands, December 2007.
- [164] S.L. Delp, J.P. Loan, M.G. Hoy, F.E. Zajac, E.L. Topp, and J.M. Rosen. An interactive graphics-based model of the lower extremity to study orthopaedic surgical procedures. *IEEE Transactions on Biomedical Engineering*, 37(8):757–767, Aug 1990.
- [165] E.Y. Chao, R.K. Laughman, E. Schneider, and R.N. Stauffer. Normative data of knee joint motion and ground reaction force in adult level walking. *Journal of biomechanics*, 16:219–233, Feb. 1983.
- [166] H.D. Eberhart, V.T. Inman, and B. Bresler. *The Principal Elements in Human Locomotion, Chapter 15, Human Limbs and their Substitutes*. Ed. Klopsteg PE, Wilson PD, eds. New York, NY: Hafner Publishing Company, 1968.
- [167] A.N. Gyory, E.Y. Chao, and R.N. Stauffer. Functional evaluation of normal and pathological knees during gait. *Arch Phys Med Rehabil*, 57(12):571–577, 1976.
- [168] M.P. Murray, A.B. Drought, and R.C. Kory. Walking patterns of normal men. *J Bone Joint Surg*, 46A:335–360, 1964.
- [169] D.B. Kettelkamp, R.J. Johnson, G.L. Smidt, E.Y. Chao, and M. Walker. An electrogoniometric study of knee motion in normal gait. *J Bone Joint Surg*, 52A:775–790, 1970.
- [170] M.P. Murray, L.A. Mollinger, G.M. Gardner, and S.B. Sepic. Kinematic and emg patterns during slow, free, and fast walking. *Journal of orthopaedic research : official publication of the Orthopaedic Research Society*, 2:272–280, Jan. 1984.
- [171] M.P. Kadaba, H.K. Ramakrishnan, M.E. Wootten, J. Gainey, G. Gorton, and G.V.B. Cochran. Repeatability of kinematic, kinetic, and electromyographic data in normal adult gait. *Journal of orthopaedic research : official publication of the Orthopaedic Research Society*, 7:849–60, Nov. 1989.
- [172] M.H. Woollacott, A. Shumway-Cook, and L.M. Nashner. Aging and posture control: Changes in sensory organization and muscular coordination. *The International Journal of Aging and Human Development*, 23(2):97–114, 1986.
- [173] M.A. Dettmann, M.T. Linder, and S.B. Sepic. Relationships among walking performance, postural stability, and functional assessments of the hemiplegic patient. *American journal of physical medicine*, 66:77–90, Mai 1987.

- [174] D.R. Gore, M.P. Murray, S.B. Sepic, and G.M. Gardner. Walking patterns of men with unilateral surgical hip fusion. *The Journal of bone and joint surgery. American volume*, 57:759–765, Oct. 1975.
- [175] R. Johnston and G.L. Smidt. Measurement of hip-joint motion during walking. evaluation of an electrogoniometric method. *The Journal of bone and joint surgery. American volume*, 51A(6):1082–1094, 1969.
- [176] A. Levens, V.T. Inman, and J. Blosser. Transverse rotation of the segments of the lower extremity in locomotion. *The Journal of bone and joint surgery. American volume*, 30A:859–872, 1948.
- [177] E. Bideen, R. Olshen, S. Simon, D. Sutherland, J. Gage, and M. Kadaba. Comparison of gait data from multiple labs. *Proceedings of the 33rd Annual Orthopedic Research Society Meeting, San Francisco, CA*, Jan. 1987.
- [178] R.L. Waters, J. Morris, and J. Perry. Translational motion of the head and trunk during normal walking. *Journal of Biomechanics*, 6(2):167 – 172, 1973.
- [179] A. Thorstensson, J. Nilsson, H. Carlson, and M.R. Zomlefer. Trunk movements in human locomotion. *Acta physiologica Scandinavica*, 121:9–22, Jun. 1984.
- [180] H.J. RALSTON. Effects of immobilization of various body segments on the energy cost of human locomotion. *Ergonomics*, 12:53–60, 1965.
- [181] M.W. Chapman and K.M. Kurokawa. Some observations on the trasverse rotations of the human trunk during locomotion. *Bull. prosthet. Res.*, 10:38–59, 1969.
- [182] S. Ha, Y. Han, and H. Hahn. Adaptive gait pattern generation of biped robot based on human's gait pattern analysis. *International Journal of Aerospace and Mechanical Engineering*, 1(2):80–85, 2007.
- [183] D.T. Romero. *Génération de mouvements optimaux de marche pour des robots bipèdes 3D*. PhD thesis, IRCCyN, Ecole centrale de Nantes, Nantes, France.
- [184] J. Denavit and R.S. Hartenberg. A kinematic notation for lower-pair mechanisms based on matrices. *Trans. of the ASME. Journal of Applied Mechanics*, 22:215–221, 1955.
- [185] J.-I. Yamaguchi, A. Takanishi, and I. Kato. Development of a biped walking robot compensating for three-axis moment by trunk motion. In *Proceedings of 1993 IEEE/RSJ International Conference on Intelligent Robots and Systems (IROS '93)*, volume 1, pages 561–566, Jul. 1993.
- [186] J.B. Keller. Impact with friction. *ASME. J. Appl. Mech.*, 53(1):1–4, 1986.
- [187] R.M. Brach. Rigid body collisions. *ASME. J. Appl. Mech.*, 56(1):133–138, 1989.
- [188] M. Bausset. *Mécanique des systèmes de solides: dynamique de Newton, dynamique de Lagrange, mécanismes, chaînes robotiques, potentiels géodésiques, potentiels gravifiques*. Enseignement de la physique. Masson, 1990.

- [189] P. Orhant. *Contribution à la manipulation fine. Étude de la phase d'impact*. PhD thesis, Institut national polytechnique de Grenoble, Laboratoire d'automatique de Grenoble, 1994.
- [190] S. Miossec. *A contribution to the study of biped walk*. PhD thesis, Ecole Centrale de Nantes (ECN) ; Université de Nantes, November 2004.
- [191] M.W. Walker and D.E. Orin. Efficient dynamic computer simulation of robotic mechanisms. *ASME. J. Dyn. Sys. Meas. Control*, 104(3):205–211, 1982.
- [192] T. Coleman, M. Ann Branch, and A. Grace. Optimization toolbox for use with matlab, user's guide, version 3. Jan. 1999.
- [193] M.J.D. Powell. *Variable Metric Methods for Constrained Optimization, Lecture Notes in Mathematics*. Springer, Berlin, 1977.
- [194] R.McN. Alexander. Optimum walking techniques for quadrupeds and bipeds. *Journal of Zoology*, 192(1):97–117, 1980.
- [195] S. Kumar. *Contribution to modeling of human walking gait cycle over stride based on robotics for pedestrian navigation solution*. PhD thesis, École Centrale de Nantes, France, Aug. 2015.
- [196] M.L. Harris-Love, L.W. Forrester, R.F. Macko, K.H.C. Silver, and G.V. Smith. Hemiparetic gait parameters in overground versus treadmill walking. *Neurorehabilitation and Neural Repair*, 15(2):105–112, 2001.
- [197] S. Hesse, M. Konrad, and D. Uhlenbrock. Treadmill walking with partial body weight support versus floor walking in hemiparetic subjects. *Archives of Physical Medicine and Rehabilitation*, 80(4):421–427, 1999.
- [198] D. Gouwanda. Comparison of gait symmetry indicators in overground walking and treadmill walking using wireless gyroscopes. *Journal of Mechanics in Medicine and Biology*, 14, Feb. 2014.
- [199] P.J. Potvin and R.W. Schutz. Statistical power for the two-factor repeated measures anova. *Behavior Research Methods, Instruments, & Computers*, 32(2):347–356, Jun. 2000.
- [200] N. Lythgo, C. Wilson, and M. Galea. Basic gait and symmetry measures for primary school-aged children and young adults whilst walking barefoot and with shoes. *Gait & posture*, 30:502–506, Aug. 2009.
- [201] H. Sadeghi, P. Allard, F. Prince, and H. Labelle. Symmetry and limb dominance in able-bodied gait: a review. *Gait & Posture*, 12(1):34–45, 2000.
- [202] J.A. Zeni, J.G. Richards, and J.S. Higginson. Two simple methods for determining gait events during treadmill and overground walking using kinematic data. *Gait & Posture*, 27(4):710–714, 2008.
- [203] P. de Leva. Adjustments to zatsiorsky-seluyanov's segment inertia parameters. *Journal of Biomechanics*, 29(9):1223–1230, 1996.

-
- [204] J. Zhao, Y. Wei, S. Xia, and Z. Wang. Estimating human body segment parameters using motion capture data. In *2010 4th International Universal Communication Symposium*, pages 243–249, Oct. 2010.
- [205] K. An and Q. Chen. Dynamic optimization of a biped model: Energetic walking gaits with different mechanical and gait parameters. *Advances in Mechanical Engineering*, 7(5):1–13, Mai 2015.
- [206] M.Y. Zarrugh, F.N. Todd, and H.J. Ralston. Optimization of energy expenditure during level walking. *European Journal of Applied Physiology and Occupational Physiology*, 33(4):293–306, Dec. 1974.
- [207] B. Kaddar. *Effet du balancement des bras sur la consommation énergétique durant la marche d'un robot bipède*. PhD thesis, Nantes University, France, 2013.
- [208] D. Tlalolini, C. Chevallereau, and Y. Aoustin. Comparison of different gaits with rotation of the feet for a planar biped. *Robotics and Autonomous Systems*, 57(4):371–383, 2009.
- [209] D. Tlalolini, Y. Aoustin, and C. Chevallereau. Design of a walking cyclic gait with single support phases and impacts for the locomotor system of a thirteen-link 3d biped using the parametric optimization. *Multibody System Dynamics*, 23(1):33, Sep. 2009.

Appendix A

R. Dumas et al. / Journal of Biomechanics 40 (2007) 543–553

Definition of the segment lengths and of the origins of the segment coordinate systems (SCSs)—values of the segment length L (used for scaling) and of the scaling factors for the segment mass m , the position of centre of mass, the moments of inertia and the products of inertia (i denotes negative product of inertia)—see Section 2.5 in the text for an example of the use of this Table

Segment	Length definition	Origin of SCS	Gender	Length L (in mm)	Scaling factor for mass m (%)	Scaling factors for position of centre of mass			Scaling factors for tensor of inertia					
						X (%)	Y (%)	Z (%)	r_{xx} (%)	r_{yy} (%)	r_{zz} (%)	r_{xy} (%)	r_{xz} (%)	r_{yz} (%)
<i>Head & Neck</i>	<i>CJC to HV</i>	<i>CJC</i>	F	221	6.7	-7.0	59.7	0	32	27	34	6(i)	1	1(i)
			M	244	6.7	-6.2	55.5	0.1	31	25	33	9(i)	2(i)	3
<i>Torso</i>	<i>CJC to LJC</i>	<i>CJC</i>	F	429	30.4	-1.6	-43.6	-0.6	29	27	29	22	5	5(i)
			M	477	33.3	-3.6	-42.0	-0.2	27	25	28	18	2	4(i)
<i>Arm</i>	<i>SJC to EJC</i>	<i>SJC</i>	F	243	2.2	-7.3	-45.4	-2.8	33	17	33	3	5(i)	14
			M	271	2.4	1.7	-45.2	-2.6	31	14	32	6	5	2
<i>Forearm</i>	<i>EJC to WJC</i>	<i>EJC</i>	F	247	1.3	2.1	-41.1	1.9	26	14	25	10	4	13(i)
			M	283	1.7	1.0	-41.7	1.4	28	11	27	3	2	8(i)
<i>Hand</i>	<i>WJC to midpoint between MH₂ and MH₅</i>	<i>WJC</i>	F	71	0.5	7.7	-76.8	4.8	63	43	58	29	23	28(i)
<i>Pelvis</i>	<i>LJC to projection of HJC in sagittal plane</i>	<i>LJC</i>	M	80	0.6	8.2	-83.9	7.4	61	38	56	22	15	20(i)
			F	107	14.6	-0.9	-23.2	0.2	91	100	79	34(i)	1(i)	1(i)
<i>Thigh</i>	<i>HJC to KJC</i>	<i>HJC</i>	M	94	14.2	2.8	-28.0	-0.6	101	106	95	25(i)	12(i)	8(i)
			F	379	14.6	-7.7	-37.7	0.9	31	19	32	7	2(i)	7(i)
<i>Leg</i>	<i>KJC to AJC</i>	<i>KJC</i>	F	432	12.3	-4.1	-42.9	3.3	29	15	30	7	2(i)	7(i)
			M	388	4.5	-4.9	-40.4	3.1	28	10	28	2	1	6
<i>Foot</i>	<i>AJC to midpoint between MH₁ and MH_V</i>	<i>AJC</i>	F	433	4.8	-4.8	-41.0	0.7	28	10	28	4(i)	2(i)	5
			M	165	1.0	27.0	-21.8	3.9	17	36	35	10(i)	6	4(i)
<i>Alternative length and origin</i>			M	183	1.2	38.2	-15.1	2.6	17	37	36	13	8(i)	0
<i>Torso</i>	<i>C₇ to SUP</i>	<i>SUP</i>	F	125	30.4	-41.1	-117.3	-1.9	98	93	98	76	16	19(i)
			M	139	33.3	-45.6	-112.1	-0.8	93	85	96	62	7	13(i)
<i>Hand</i>	<i>WJC to FT₃</i>	<i>WJC</i>	F	167	0.5	3.3	-32.7	2.1	27	18	25	12	10	12(i)
			M	189	0.6	3.5	-35.7	3.2	26	16	24	9	7	8(i)
<i>Pelvis</i>	<i>Midpoint between RASIS to LASIS</i>	<i>Middle of RASIS and LASIS</i>	F	238	14.6	-37.1	-5.0	0.1	41	45	36	15(i)	0	0
<i>Foot</i>	<i>CAL to TT_{II}</i>	<i>CAL</i>	M	224	14.2	-33.6	-14.9	-0.3	42	44	40	10(i)	5(i)	3(i)
			F	233	1.0	44.3	4.4	-2.5	12	25	25	7(i)	5	3(i)
			M	265	1.2	43.6	-2.5	-0.7	11	25	25	9	6(i)	0

Appendix C

Arm motion

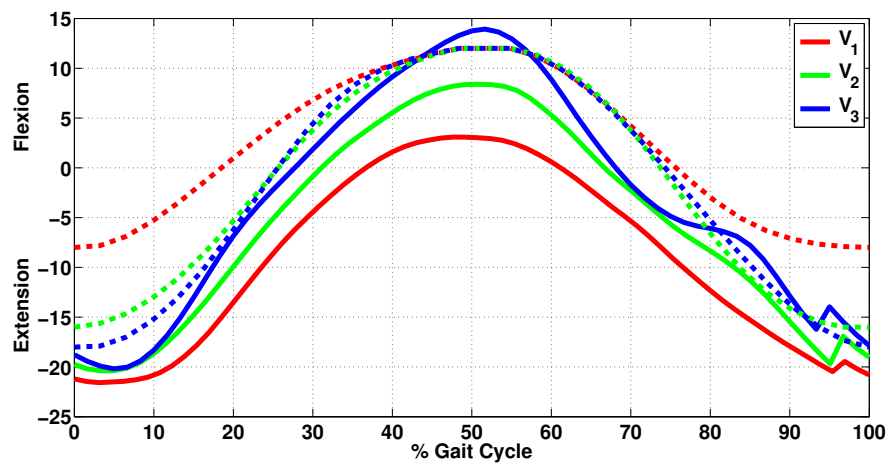


Fig. C.1 Shoulder flexion/extension motion during a stride (first step is ipsilateral). Solid line for experimental data, dashed line for simulation data.

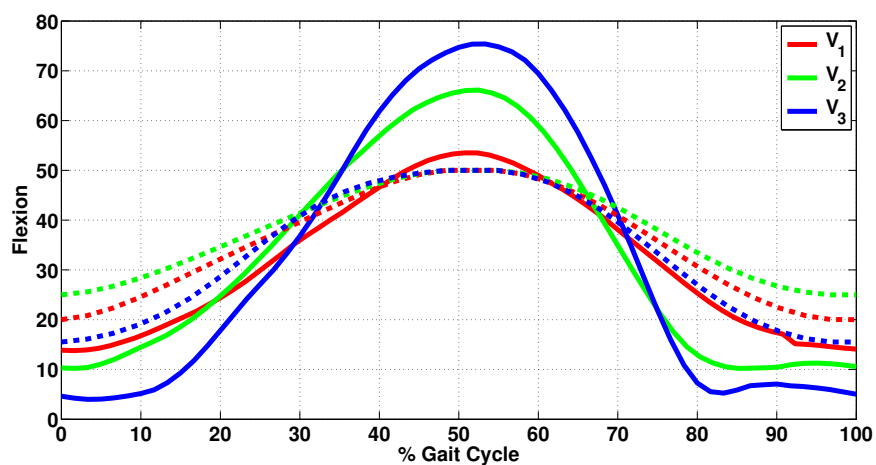


Fig. C.2 Elbow flexion motion during a stride (first step is ipsilateral). Solid line for experimental data, dashed line for simulation data.

Appendix D

COM displacement

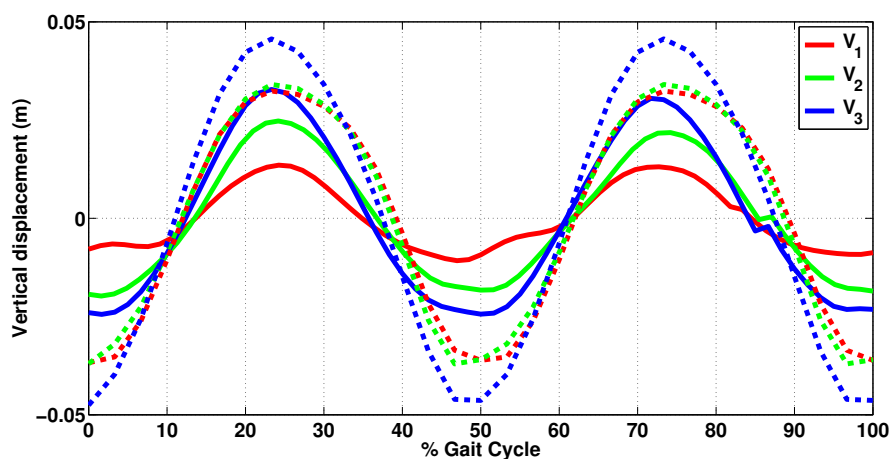


Fig. D.1 Vertical displacement of COM during a stride. Solid line for experimental data, dashed line for simulation data.

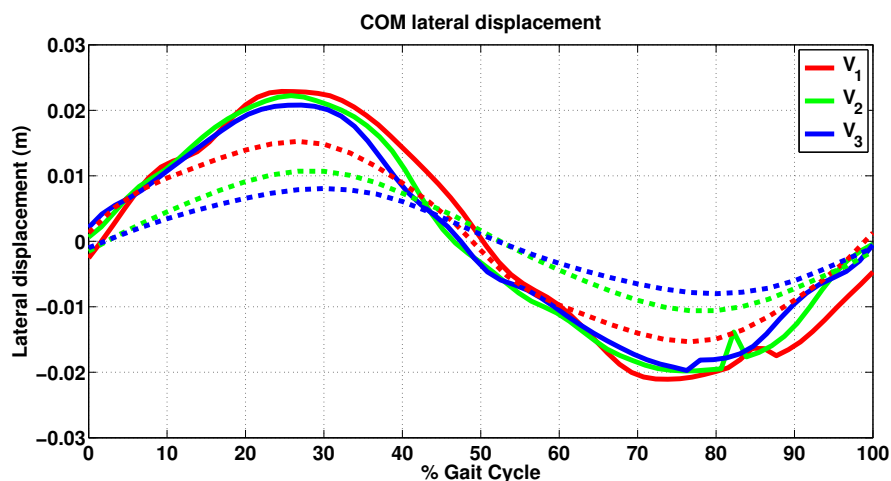


Fig. D.2 COM mediolateral displacement during a stride. Solid line for experimental data, dashed line for simulation data.

Appendix E

2D biped model

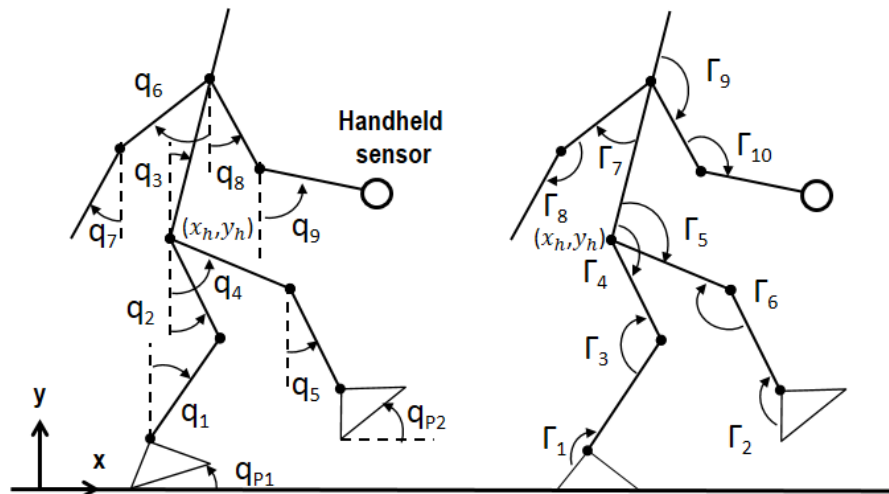


Fig. E.1 2D Biped with two-link arms, one equipped with a handheld device, with its different DOFs and corresponding actuators [157].

Appendix F

Acceleration of handheld device

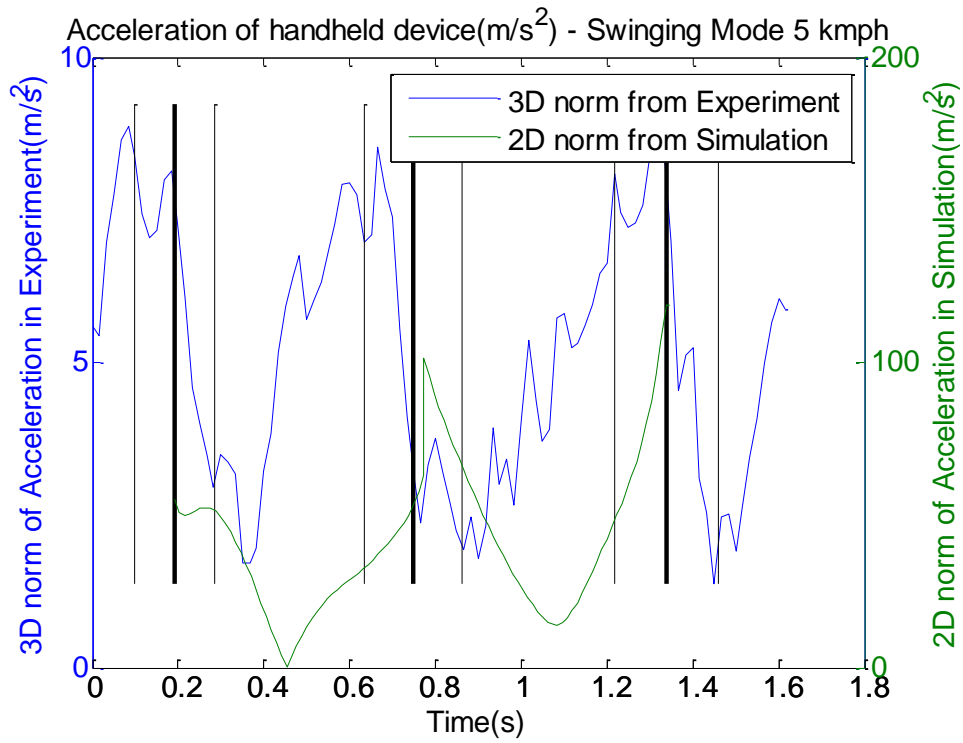


Fig. F.1 Comparison between the handheld device characteristics from simulation and experiments for swinging mode at 5 km/h [157].

Appendix G

Sthenic criterion

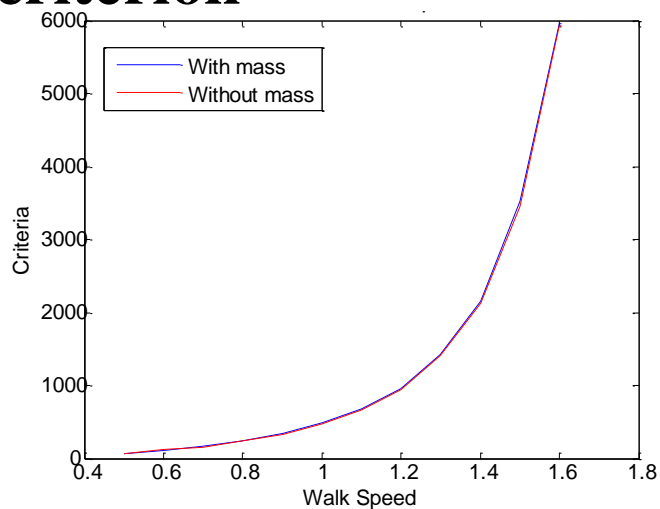


Fig. G.1 Criteria vs Walking Speed with and without IMU sensor in hand [195].

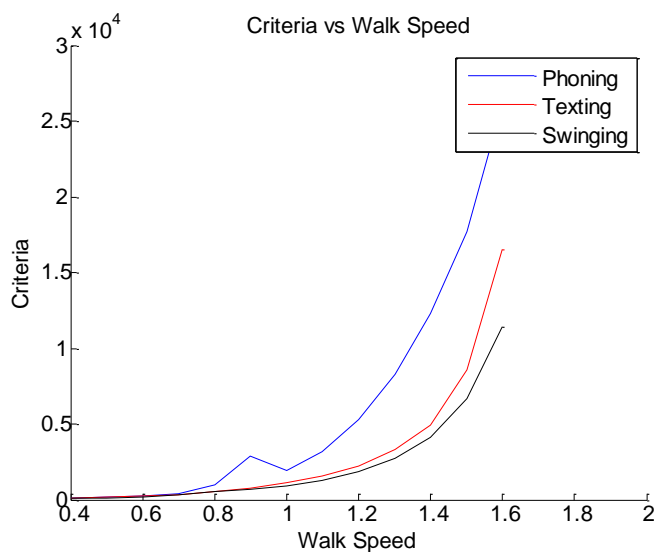


Fig. G.2 Criteria variation with walking speed for swinging, texting and phoning modes [195].

Titre : titre (en français)... Estimation et caractérisation du cycle de marche humain à l'aide de dispositifs portables

Mots clés : Dispositifs portables, Système multi-corps, Optimisation paramétrique, Symétrie de pas, Motifs de marche humaine, Analyse de variance.

Résumé : De nouveaux dispositifs portables sont introduits pour l'observation de la mobilité des personnes dans les espaces intérieurs et extérieurs. Ce matériel comprend des capteurs MEMS à bas coût : accéléromètre, gyromètre, magnétomètre, qui fournissent en permanence des données disponibles contrairement aux solutions existantes basées sur les signaux radio. Afin d'atténuer la propagation des erreurs des capteurs dans l'estimation de la position, une stratégie de navigation à l'estime des piétons est couramment adoptée. Le traitement nécessite des modèles paramétriques de longueur de pas s'appuyant sur certains paramètres physiologiques, des caractéristiques de déplacement et des propriétés statistiques d'accélération. Les coefficients de ces modèles doivent être ajustés fréquemment pour limiter les erreurs cumulatives induites par la variation des allures de marche. Une vaste base de données expérimentale fournissant des informations sur la variabilité de la locomotion humaine est nécessaire pour cette calibration. Cependant, le développement d'une telle base de données est coûteux en termes de temps et d'efforts, et plusieurs facteurs affectant la marche devraient être considérés, ce qui augmente considérablement le nombre d'essais. Dans cette thèse, nous proposons une méthode alternative de génération de données qui consiste à simuler le mouvement de la marche humaine dans différentes conditions. Dans ce but, un simulateur multi-corps 3D basé sur une technique d'optimisation paramétrique a été développé et des améliorations ont été apportées tout au long de ce travail pour obtenir une prévision plus réaliste des mouvements de marche. Les trajectoires articulaires au cours d'un pas ont été optimisées en minimisant un

critère d'énergie basé sur les couples actionnés. La validation avec des données inertielles provenant d'expérimentations de marche au sol sur un sujet sain a montré une asymétrie dans les signaux d'accélération expérimentaux d'un pas à l'autre. Cela suggère que les mouvements asymétriques sont susceptibles d'entraîner une asymétrie des caractéristiques de pas. Cela va à l'encontre de l'hypothèse générale de la stratégie PDR : la présence d'un dispositif en main n'affecte pas la symétrie de la marche et tous les pas sont identiques pour une vitesse de marche fixe. Cette hypothèse est étudiée à l'aide d'expériences de capture de mouvement sur plusieurs sujets, conçues pour étudier l'influence d'une masse portée à la main sur les cycles de marche. L'analyse de variance a montré que la présence d'une masse en main modifie la symétrie de marche au niveau du pas, puis le processus d'optimisation proposé est étendu au niveau de la foulée afin de permettre d'observer des profils d'accélération asymétrique. Dans l'ensemble, notre simulateur reproduit des motifs fondamentaux similaires de la marche et la même tendance de variation des caractéristiques liées à l'accélération que l'on retrouve dans les expérimentations. Cependant, il présente des limites lorsqu'il s'agit de prédire les données d'accélération liées à la main, en raison de certaines hypothèses de modélisation et de problèmes numériques. Par conséquent, notre approche de simulation résout partiellement le problème direct de modélisation dans la navigation piétonne, et des améliorations par rapport aux hypothèses du modèle sont prévues pour une prédiction plus fiable des signaux d'accélération sur un cycle de marche complet.

Title : titre (en anglais)..... Walking gait features extraction and characterization using wearable devices.....

Keywords : Handheld devices, Multibody system, Parametric optimization, Step-level symmetry, Walking gait patterns, Analysis of variance.

Abstract : New wearables devices are introduced with novel options for observing personal transport and mobility in indoor and outdoor spaces. This hardware includes low cost MEMS sensors: accelerometer, gyroscope, magnetometer, which provide continuously available data contrary to existing solutions that are based on radio signals. In order to mitigate the propagation of sensor errors in the position estimate, a pedestrian dead reckoning strategy is commonly adopted. The processing requires parametric step length models relying on some physiological parameters, displacement features and acceleration statistical properties. The coefficients of these models need frequent adjustment to limit cumulative errors induced by alteration of gait pattern. A large experimental database providing information about human locomotion variability is required for this calibration. However, the development of such database is costly in terms of time and effort, and several gait-affecting factors should be considered, which highly increases the number of measurement trials. In this thesis, we propose an alternative way of generating locomotion data that consists in simulating human gait motion under different conditions. In this scope, a 3D multibody system simulator based on parametric optimization technique was developed, and improvements were made throughout this work to get a more realistic walking motion prediction. Joint trajectories during one step were optimized by minimizing an energy criterion

based on actuated torques. Validation with inertial data from overground walking experiments on one healthy subject showed an asymmetry in experimental acceleration signals from one step to the next. This suggests that asymmetric movement are likely to result in a step-level asymmetry of displacement features. This defeats the general assumption in PDR strategy: the presence of a device in hand does not impact the gait symmetry and all steps are identical for a fixed walking speed. This hypothesis is investigated with motion capture experiments with several subjects, designed to study the influence of a mass carried in hand on the walking gait cycles. Analysis of variance tests have shown that the presence of a mass in hand changes the gait symmetry at the step level, and then the proposed optimization process is extended to the stride level in order to allow observing asymmetric acceleration patterns. Overall, our simulator reproduces similar fundamental patterns of walking, and the same variation trend of acceleration related items found in experiments. However, it shows limitations when predicting acceleration data related to the hand, due to some modeling assumptions and numerical issues. Therefore, our simulation approach partially solves for the direct modeling problem in pedestrian navigation, and improvements on model assumptions are foreseen to predict acceleration signals over a complete gait cycle more reliably.